Acknowledgements

It is not simple to express in a few words the recognition, gratitude and esteem that I feel about my supervisor, Dr. Augusto Smerzi: for the constant attention and the time he devoted me, for being helping and comprehensive during the difficult moments, for his patience and kindness. He has taught me many things, not only in physics. I thank him deeply.

I would like to thank Prof. S. R. Shenoy: I appreciate very much our discussions during which he communicated me his passion for science and research.

I have been fortunate to spend four months at the LENS laboratory at Firenze: it was a stimulating and interesting period which I remember with great pleasure. I would like to thank here Dr.s S. Burger, F. S. Cataliotti, C. Fort, P. Maddaloni, F. Minardi and Prof. M. Inguscio.

I would also like to thank Prof. A. R. Bishop for inviting me to spend two months at the Los Alamos National Laboratory. I enjoyed a fruitful collaboration, the results of which are described in the third chapter of this thesis. During my stay at LANL I found a pleasant working environment which I liked very much. I also want to thank, for our discussions, Dr.s K. Ø. Rasmussen and G. Kalosakas (I remember a "lucky day" with him!).

I warmly thank Dr.s A. Fubini and F. Ferlaino for our discussions and pleasant conversations.

Finally, I would like to give a special and warm thanks to Prof. P. Sodano, for our interesting discussions and for all the time he has devoted me.

I spent a nice period at SISSA: I would like to thank all the people I met and helped me, in particular Dr.s A. De Martino, L. Giada and P. Tangney.

Contents

INTRODUCTION

Since the first experimental observation of the Bose-Einstein condensation of a gas of alkali atoms, six years ago, there has been an increasing interest on this new, highly interdisciplinary, branch of physics.

It was realized, from the very beginning that, despite of the diluteness of such systems, the *nonlinearity* was crucial on the understanding of both the equilibrium and dynamical properties.

In this Thesis we point out that there is a further key aspect that must be taken into account when the condensates are trapped in deep optical lattices: *discreteness*.

The interplay between discreteness and nonlinearity raises a new class of deeply non-trivial phenomena which disappear in the continuum limit of the Gross-Pitaevskii equation (GPE). Recognizing and exploiting such interplay is the main topic of this Thesis.

We think that the dynamics of a Bose-Einstein condensate (BEC) in optical lattices is going to become of central interest in the next future. Optical potentials provide BEC's waveguides, which prevent the spatial spreading of the BEC wave packets and preserve their coherence over long distances. This has allowed to build high sensitive interferometers, including gyroscopes and gravitometers. From the theoretical point of view, the big challenge is to reconsider the meaning of phenomena which have been well understood in homogeneous systems: superfluidity, for instance, is in the top list. A further example is given by quantum phase transitions.

The connection and the interplay with the language and insights of the nonlinear physics community is a second challenge. We believe that the results obtained in the BEC context can provide a new prospective view into old problems. The understanding of the modulational instability in terms of phase randomization and a (classical) dynamical phase transition are among this line, as well as the possibility to generalize the Landau criteria for superfluidity to discrete systems. On the other hand, it is clear that nonlinear physicists can have much to say about BEC. With this Thesis we hope we have provided, together with original results, some links between these different languages and views.

In the first part of the Thesis we discuss the dynamical regimes of a BEC in an optical lattice. There are several important reasons to study this system, which is under intense experimental and theoretical investigation. First of all, the experimental realizations [1–8] have reached a high level of precision, with easily tunable parameters and accurately tailored trapping profiles. The periodic potential is generally realized with two counterpropagating laser beams. The intensity of the laser is proportional to the interwell energy barrier and can be varied in a wide spectrum of values, ranging from a situation in which the optical potential can be considered as a small perturbation to the case in which the BEC chemical potential is much smaller than the interwell energy barriers.

The key feature that makes the dynamical properties of such systems particularly interesting is that the periodic potential naturally introduce *discreteness* in a nonlinear system. The theoretical investigations have pointed out that the excitation spectrum of a BEC in an optical lattice exhibits band structure in analogy with the electron energy Bloch bands in a periodic potential [9–12]. When the the power of the laser (i.e. the strength of the optical potential) is strong enough, the lowest band dynamics maps on a discrete nonlinear Schrödinger equation (DNLSE) [13] (see Chapter 1). The dynamics in the array can be therefore studied in the framework of the nonlinear lattice theory [13–15]. The DNLSE is an equation widely investigated *per se* in the nonlinear physics [16–18] and it is important in the study of different physical systems, ranging from polaron theory to optical fiber arrays. The possibility to have an experimental system to test the DNLSE (and more general discrete nonlinear equations) in the framework of the nonlinear lattice theory is creating a wide interest for the properties of arrays of BECs in different physics communities. BEC in a periodic potential can allow for the observations of intrinsic localized modes (i.e. matter excitations localized on few lattice sites), as well as the study of solitons and breathers, possibly also with condensates having a repulsive interatomic interactions. The criterion to have such discrete solitons and breathers (DSB) will be given in section 1.4.

The experimental realization of an array of BECs in an optical lattice also provides a concrete experimental framework to study the phase dynamics and the atomic tunneling between neighbour wells of the optical potential.

The phase coherence of different condensates in the array plays a crucial role in the dynamics, and can be easily studied experimentally observing the interference patterns created by the condensates after turning off the magnetic trap.

Another important issue, motivated from the experiments [1, 6–8], is the study of the effects of external forces on the discrete dynamics of the lattice. In the presence of the gravitational field (i.e. with an linear external energy in the DNLSE), coherent Bloch oscillations occur [1]. Similarly, Bloch oscillations are also possible in horizontal optical lattices realized by two counterpropagating laser beams with a frequency detuning varying linearly in time (more details on this experimental setup in [19, 20]).

The effect of the nonlinearity is the coherent destruction of the interwell Bloch oscillations: this manifests in a distortion of the on-site phases of the condensates in the different traps [1, 13]. A discussion of this case will be considered in section 1.5.

The dynamics in a harmonic magnetic trap was studied in [7]. The first direct observation of a Josephson atomic current in a one-dimensional array of BECs has been reported in [8]; the coherence of multiple adjacent wells was continuously probed by atomic interference. This experiment and its theoretical analysis will be discussed in detail in Chapter 2.

Yet, two possible lines of future research are: 1) the study of generalized discrete equations which governs the system when the inclusion of on site collective degrees of freedom are important; 2) the inclusion of a disorder potential, created e.g. with additional lasers, in order to investigate the interplay of discreteness nonlinearity and disorder. In Chapter 3 we will discuss the latter problem on a different perspective respect to the current literature [21].

The discreteness is also relevant for the occurrence of new dynamical instabilities, well known in the theory of nonlinear media (continuous as well as discrete). In section 2.4 we will discuss both from a theoretical and experimental point of view the occurrence of a discrete Modulational Instability (MI).

The recent realization of the two-dimensional optical lattices [3] opens the possibility to study discreteness effects in higher dimensions. Last, but not least, the high laser power available nowadays could allow for the investigation of low tunneling rates between adjacent wells of the periodic potential: in these regimes the quantum fluctuations play an important role, and, with a strength of the optical potential V_0 large enough, it is expected a quantum transition from the superfluid to the Mott insulator phase diagram region. The observation of squeezed number states was reported in [6]. An estimate of the coupling between wells as a function of V_0 will be presented in section 2.3: from this estimate it is also possible to evaluate the power of the laser needed to observe the quantum phase transition. We think that this is a very promising field of research. The competition of thermal and quantum effects is also, in this regard, another important problem [22, 23].

In the analysis of Part I, we do not consider the effect of the internal degrees of freedom of the condensates in the different wells. In Part II we discuss how include these effects for *two* wells. The main goal is to understand if the internal modes can affect the Josephson currents, and how. We will actually show that the Josephson relation between the current and the phase difference is still valid, but with time-dependent coefficients which depends explicitly on the dynamics of the internal degrees of freedom.

In Chapter 4 we consider two different hyperfine levels coupled by a laser, that induces a Josephson-like coupling between the states. The two components feel different effective harmonic traps (with different harmonic trap-curvatures and/or different positions of trap minima). Using two gaussian-profile variational wavefunctions we determine dynamical equations coupling the fractional number difference, the effective phase difference, and the rocking and breathing motions of the BEC profiles. These equations, also describe one-component ground state BEC tunneling between actual double wells, considered previously in a fixed-position and rigid-profile-case, but now with BEC center-of-mass motion and collective modes included. The equations map onto the dynamics of a momentum-shortened pendulum, as found in previous works, but now with an additional pendulum-length stretching. The five fixed points classifying five pendulum modes of oscillation about average values of 0 or π found previously are preserved, but the modes are enriched and modified. They are studied in section 4.3. In particular, the macroscopic quantum self-trapping regime still occurs: the population imbalance between the two traps is maintained by the interatomic interaction. The different regimes of the quantum phase dynamics show up in characteristic oscillations of the center-of-mass and density profiles, providing an experimental tool to detect and study the Josephson oscillations. The results of this chapter can be generalized to the case of more than two atomic species, or equivalently, to the case of multiple wells.

In Chapter 5 we discuss how to create a weak link between the two hyperfine levels: this is reached by applying a far-detuned laser. The parameter of the weak link is showed to be proportional to Ω/δ, where Ω is the Rabi frequency (i.e. the strength of the laser) and δ is the detuning. We will also discuss the experimental results obtained with this weak link [24]: the macroscopic quantum oscillations between the condensates are presented and compared with the Josephson equations of the system. With the particular geometry, the center of the two potentials are far $15\mu m$, while their width is $\approx 4\mu m$. The time-dependent Josephson current vanishes in a time of order $200\mu s$: this is the window time in which the Josephson oscillations are detectable (and they have been detected). We compare these results with the Rabi oscillations of the thermal cloud (i.e. above the critical temperature): the experimental findings clearly show that they damp more quickly than the condensate oscillations. Furthermore, we discuss analogies and differences between the Rabi and the Josephson regimes.

Part I

BOSE-EINSTEIN CONDENSATES IN OPTICAL LATTICES

Chapter 1

Discrete nonlinear dynamics

1.1 Introduction

In this chapter we discuss the dynamical regimes of a BEC in periodic potentials, a problem which has recently attracted a lot of interest [9–15, 25–31]. The plan of the chapter is the following: in section 1.2 we derive the DNLSE from the Gross-Pitaevskii equation (GPE) and we discuss the validity of a such derivation. The dynamical phase diagram for the horizontal array (i.e. without any external driven field) is obtained and discussed in section 1.4: a collective coordinate approach (described in section 1.3) is used and compared with full numerical calculations. We investigate the different dynamical regimes: diffusive (in which the boson wave packet spreads out), self-trapped (with a self-induced pinning), breathing (where the center of mass of the wave packet moves with an oscillating width), and solitonic (in which the wave packet shape is exactly preserved during the dynamics). The equations of motion for the variational parameters which describe the boson wave packet are derived and systematically studied in App.A. In section 1.5

we discuss the dynamics of arrays of BECs in a tilted (washboard) potential describing a vertical optical trap, showing that the effects of the mean field interaction lead to a breakdown of the Bloch oscillations.

1.2 From GPE to DNLSE

In this section we state the dynamical equations of a BEC in a periodic potential also in presence of an external driven field. We introduce a collective coordinate approach: this method was described in [13], where it was studied the dynamical phase diagrams of the system and the breakdown of Bloch oscillations due to mean field effects in the Anderson-Kasevich experiment [1]. The variational equations can be cast in Hamiltonian form allowing to define the group velocity and the effective mass, as in the standard (semiclassical) Bloch theory of an electron in a periodic potential. The possibility to have a negative effective mass gets reflected in the existence of bright soliton regimes, even if the BEC's interatomic potential is repulsive (we recall that in free space only dark solitons can exist if the scattering length is positive). In the regimes in which the effective mass diverges, the wave packet localizes around a few lattice sites, stopping its motion. The pinning is accompanied by a breaking of the global coherence. Therefore the variational ansatz breaks down, but still predicts the mean field energy critical value for the occurrence of the localization.

The full dynamics (at $T = 0$) of a BEC in an external potential V_{ext} satisfies the Gross-Pitaevskii equation (GPE) [32]:

$$i\hbar\frac{\partial\Psi}{\partial t} = -\frac{\hbar^2}{2m}\nabla^2\Psi + [V_{ext} + g_0 \mid \Psi \mid^2]\Psi \tag{1.1}$$

where $g_0 = \frac{4\pi\hbar^2 a}{m}$, with a s-wave scattering length and m the atomic mass. The condensate wave function is normalized to the total number of particles N_T. We write the external potential as the sum of the laser field and a potential $\mathcal{V}$, whose form depends on the particular experiment:

$$V_{ext}(\vec{r}) = \mathcal{V}(\vec{r}) + V_L(y,z)\cos^2[2\pi x/\lambda] \tag{1.2}$$

where λ is the wavelength of the lasers (the spacing in the lattice is $\lambda/2$) and $V_L(y,z)$ is determined by the transverse intensity profile of the (nearly gaussian) laser beams. E.g., in [1], $\lambda = 850\,nm$ and the $1/e^2$ radius of the transverse profile is $\approx 80\mu m$, an order of magnitude larger than the transverse radius of the condensate. Varying the intensity of the laser beam we can change linearly the trap well depths. We define V_0 as the trap depth at the center of the beam, $V_0 = \beta E_R$ where $E_R = \frac{\hbar^2 k^2}{2m}$ is the recoil energy ($k = 2\pi/\lambda$): for typical experimental values [7,8], β range from 0 to 6.

The form of $\mathcal{V}$ varies in the different experiments. $\mathcal{V} \equiv 0$ refers to the case in which only the optical lattice is present (*horizontal array*); $\mathcal{V} \equiv mgx$ when also the gravity acts (*vertical array*) [1]; $\mathcal{V}$ harmonic potential [6–8] will be called in the following *parabolic array*. We will study in this chapter the behaviour of the first two types of traps, while the latter will be discussed in the following chapter.

When the laser power (i.e. V_0) is large enough, we can use a tight-binding approximation and decompose the condensate order parameter $\Psi(\vec{r},t)$ as a sum of wave functions $\Phi(\vec{r}-\vec{r}_n)$ localized in each well of the periodic potential:

$$\Psi(\vec{r},t) = \sqrt{N_T}\sum_n \psi_n(t)\;\Phi(\vec{r}-\vec{r}_n), \tag{1.3}$$

where $\psi_j = \sqrt{n_j(t)}\,e^{i\phi_j(t)}$ is the j-th amplitude ($n_j = N_j/N_T$, where N_j and

ϕ_j are the number of particles and the phase in the trap j).

We remark that the assumption (1.3) relies on the fact the interwell barrier V_0 is much higher than the chemical potentials. E.g., in [8] for $\beta = 3$ (i.e. $V_0 = 3E_R$) it is $\mu \sim 0.06V_0$. A second important condition is that the energy of the system should be confined within the lowest band. Higher energy bands are not contained in DNLSE, and become important when the energy is of the order of $\hbar\omega_T$, where ω_T is the harmonic frequency of a single well of the lattice. The effective dimensionality of the BEC's trapped in each well can also play a crucial role [33], by modifying the degree of nonlinearity of the DNLSE. Such corrections can be included with site-dependent parameters in DNLSE, but can ultimately complicate its structure. We ignore such corrections by exploring bulk properties of the system, where the details of the (tail) density profile are irrelevant. In this prospect, the DNLSE can be seen as a zero-order (perturbative) approximation of more complicate discrete, nonlinear equations. A comparison between the ground state found in this approximation and the full ground state (which takes into account the transverse degrees of freedom) in the Firenze experiment will be given in the next chapter.

More specifically, the assumption (1.3) is a particular case of the more general adiabatic approximation

$$\Psi(\vec{r},t) = \sum_n c_n(t)\ \Phi_n(\vec{r}; N_n(t)), \tag{1.4}$$

where $< \Phi_n \Phi_m > \simeq \delta_{nm}$ and $c_n = \sqrt{N_n} e^{i\phi_n}$. The adiabatic approximation consists on neglecting the time derivative of $\Phi_n(\vec{r}; N_n(t))$. It is found (in dimensionless units) an equation of the form

$$i\dot{c}_n = \epsilon_n c_n + K_{n+1} c_{n+1} + K_{n-1} c_{n-1} + U_n \mid c_n \mid^\alpha c_n \tag{1.5}$$

where ϵ_n, K_n and U_n depends on $N_n(t)$ and on the parameters of the optical potential, and α is an effective nonlinearity depending on the dependence of the local (on site) chemical potential by the number of atoms in the same well.

The (1.5) is highly non-trivial as interesting, and deserves further investigations (see also next chapter).

Here and in the following we want to investigate effects which arise from nonlinearity and discreteness, but do not depends on the details of the optical confinement. We therefore consider a "zero-order" approximation of (1.4) with the ansatz (1.3): ϵ_n, K and U are chosen as averaged values, independent from $N_n(t)$.

Replacing the ansatz (1.3) in (1.1) we find that the GPE reduces to a DNLSE:

$$i\hbar\frac{\partial\psi_n}{\partial t} = -K(\psi_{n-1}+\psi_{n+1}) + (\epsilon_n + U \mid \psi_n \mid^2)\psi_n, \tag{1.6}$$

where the tunneling rate is

$$K \simeq -\int d\vec{r}\,\big[\frac{\hbar^2}{2m}\vec{\nabla}\Phi_n\cdot\vec{\nabla}\Phi_{n+1} + \Phi_n V_{ext}\Phi_{n+1}\big], \tag{1.7}$$

the on-site energies are

$$\epsilon_n = \int d\vec{r}\,\big[\frac{\hbar^2}{2m}(\vec{\nabla}\Phi_n)^2 + V_{ext}\Phi_n^2\big] \tag{1.8}$$

and the nonlinear coefficient (which we will suppose equal in each site) is

$$U = g_0 N_T \int d\vec{r}\,\Phi_n^4. \tag{1.9}$$

In order to cast the Eq.(1.6) in dimensionless form, we rescale the time as $t \rightarrow \frac{\hbar}{2K}t$. In [8], for $V_0 = 3E_R$ it is $K \approx 0.07E_R$ and $U \approx 12E_R$: the unit of the scaled time is $0.32\,ms$ (similar numerical value are found e.g in [1]). Defining $E_n = \epsilon_n/2K$ and $\Lambda = U/2K$, Eq.(2.6) becomes

$$i\frac{\partial \psi_n}{\partial t} = -\frac{1}{2}(\psi_{n-1} + \psi_{n+1}) + (E_n + \Lambda \mid \psi_n \mid^2)\psi_n. \tag{1.10}$$

In Eq.(1.10), the integer $n = -\infty, \ldots, -1, 0, 1, \ldots, \infty$.

Eq.(1.10) is the equation of motion $\dot{\psi}_n = \frac{\partial \mathcal{H}}{\partial(i\psi_n^*)}$, where $\mathcal{H}$ is the Hamiltonian function

$$\mathcal{H} = -\frac{1}{2}\sum_{n=-\infty}^{\infty}(\psi_n\psi_{n+1}^* + \psi_n^*\psi_{n+1}) + \sum_{n=-\infty}^{\infty}(E_n \mid \psi_n \mid^2 + \frac{\Lambda}{2} \mid \psi_n \mid^4) \tag{1.11}$$

with $i\psi_n^*, \psi_n$ canonically conjugate variables. Both the Hamiltonian $\mathcal{H}$ and the norm

$$\sum_{n=-\infty}^{\infty} \mid \psi_n \mid^2 = 1 \tag{1.12}$$

are conserved.

1.3 Variational dynamics

To study the dynamical regimes of a BEC in an array, we consider the dynamical evolution of a gaussian profile wave packet and we introduce a variational wave function

$$\psi_V^n(t) = \sqrt{k} \cdot \exp\Big\{ -\frac{(n-\xi)^2}{\alpha} + ip(n-\xi) + i\frac{\delta}{2}(n-\xi)^2 \Big\} \tag{1.13}$$

where $\xi(t)$ and $\alpha(t)$ are, respectively, the center and the square of the width $\gamma(t)$ $(\alpha = \gamma^2)$ of the density $\rho_n = \mid \psi_n \mid^2$; $p(t)$ and $\delta(t)$ are their associated momenta and $k(\xi, \alpha)$ a normalization factor.

The wave packet dynamical evolution can be obtained by using the Euler-Lagrange equations for the Lagrangian $\mathcal{L} = \sum_{n=-\infty}^{\infty} i\dot{\psi}_n\psi_n^* - \mathcal{H}$. The equations of motion for the variational parameters which describes the boson wave packet are derived in App.A and they are

$$\begin{cases} \dot{p} = -\frac{\partial V}{\partial \xi} \\ \dot{\xi} = \sin p \, \cdot \, e^{-\eta} \end{cases} \tag{1.14}$$

and

$$\begin{cases} \dot{\delta} = \cos p \Big(\frac{4}{\alpha^2} - \delta^2 \Big) e^{-\eta} + \frac{2\Lambda}{\sqrt{\pi\alpha^3}} - 8\frac{\partial V}{\partial \alpha} \\ \dot{\alpha} = 2\alpha\delta \cos p \, \cdot \, e^{-\eta} \end{cases} \tag{1.15}$$

where

$$\eta = \frac{1}{2\alpha} + \frac{\alpha\delta^2}{8} \tag{1.16}$$

and the effective potential V is given by

$$V = k \int_{-\infty}^{\infty} dn \, E_n e^{-\frac{2(n-\xi)^2}{\alpha}}. \tag{1.17}$$

The pairs ξ, p and $\frac{\alpha}{8}, \delta$ are canonically conjugate dynamical variables with respect to the effective Hamiltonian

$$H = \frac{\Lambda}{2\sqrt{\pi\alpha}} - \cos p \, \cdot \, e^{-\eta} + V(\xi, \alpha). \tag{1.18}$$

We note that for the continuous GPE (i.e. without the optical potential) we should have

$$H = \frac{\Lambda}{2\sqrt{\pi\alpha}} + \frac{1}{2}p^2 + \frac{1}{2\alpha} + \frac{\alpha\delta^2}{8} + V(\xi, \gamma). \tag{1.19}$$

In the discrete case we have a band ($\cos p$) and not a simple kinetic term as in the continuous case (p^2): this is a typical lattice effect. Furthermore in order to find the continuum case from the discrete one we have to expand the exponential term in (1.18) and to neglect the higher order terms to obtain (1.19).

The standard definition of group velocity gives

$$v_g \equiv \frac{\partial H}{\partial p} = \dot{\xi} = \frac{\tan p}{m^*} \tag{1.20}$$

with the inverse effective mass given by

$$\frac{1}{m^*} \equiv \frac{\partial^2 H}{\partial p^2} = \cos p \, e^{-\eta}. \tag{1.21}$$

The quasi-momentum dependence of the effective mass allows a rich variety of dynamical regimes. Bright solitonic solutions with a positive nonlinear parameter $\Lambda > 0$, for instance, are allowed by a negative effective mass. A regime with a diverging effective mass $m^* \to \infty$ leads to a self-trapping of the wave packet.

1.4 Horizontal array

In the horizontal lattice, only the optical potential is present ($\mathcal{V} = 0$). Therefore the on-site energies E_n, as well as $V(\xi, \gamma)$, are constant. The momentum is, of course, conserved and it is equal to the initial value:

$$p(t) = p(0) \equiv p_0. \tag{1.22}$$

We will consider the case $\Lambda > 0$, in order to make contact with the experiments in which ${}^{87}Rb$ atoms with positive scattering length a are used. However we note that the equations of motion (1.14) and (1.15) are invariant with respect to the replacement $\Lambda \to -\Lambda$, $p_0 \to p_0 + \pi$ and $t \to -t$. The case of a BEC with $a < 0$ in an optical lattice would be also very interesting, but at present date has not yet experimentally realized (for a discussion of this case, see [14]).

A detailed study of the variational equations of motion is in App.A (and in [34]). Here we quote only the main results and we discuss rather the physical implications and the comparison with a full numerical analysis. This comparison is surprisingly successful in describing even details of the quite complex dynamical and collisional behaviour. Stability phase diagrams for such states are obtained by inspection of the profile dynamics equations.

The parameter Λ is the ratio between the nonlinear coefficient, induced by the interatomic interactions, and the coupling between condensates in neighbour wells: it is the only (geometry dependent) parameter which governs the dynamical regimes of the system. When Λ is small, the wave packet spreads out; in the opposite limit, the nonlinearity leads to a localization of the wave packet. When $\cos p_0 < 0$, an intermediate regime arises: in this case, the effective mass (1.21) is negative and, for a suitable values of Λ, it can be reached a balance between nonlinearity and diffusion. In terms of the variational parameters, this means that in the diffusive regime, $\alpha \to \infty$ and (if $p_0 \neq 0$) $\xi \to \infty$, with an effective mass always finite. In the self-trapped regime, to the contrary, α remains finite and the center of mass ξ cannot go to ∞; furthermore, $1/m^* \to 0$, meaning that $\eta \to \infty$ and $\delta \to \infty$. Therefore in this regime there is an energy transfer to the internal modes of oscillations, since δ is the momentum associated to the wave packet width: in the full numerical solution of Eq.(1.10), this corresponds to a breakdown of the wave packet. We note that a nonlinear self-trapping occurs also in a two-site model [35–37].

Now we discuss separately the two different cases $\cos p_0 > 0$ and $\cos p_0 < 0$, which correspond respectively to positive and negative effective mass.

1.4.1 Positive effective mass

From the previous discussion follows that, when $\cos p_0 > 0$, the solitonic regime is forbidden and we have only the diffusive and the self-trapped regimes. In order to show the transition between them, let us consider first the case $p_0 = 0$, in which the center of mass of the wave packet does not move ($\xi = 0$). Using as initial values $\delta_0 = 0$ and α_0, the initial value of the Hamiltonian (1.18) is $H_0 = \Lambda/2\sqrt{\pi\alpha_0} - e^{-1/2\alpha_0}$. Since the Hamiltonian is a conserved quantity, it is $H_0 = \Lambda/2\sqrt{\pi\alpha} - e^{-1/2\alpha-\alpha\delta^2/8}$. Therefore $\frac{\Lambda}{2\sqrt{\pi\alpha}} - H_0 > 0$. Using the previous relation, we can see that when $H_0 > 0$, α have to remain finite and the we have a self-trapped regime in which the wave packet remain localized and the nonlinearity forbids the diffusion. Vice versa, when $H_0 < 0$, $\alpha \to \infty$ for $t \to \infty$: the wave function spreads out and we are in the diffusive regime. The transition occurs at $H_0 = 0$, with

$$\Lambda_c = 2\sqrt{\pi\alpha_0}e^{-1/2\alpha_0}. \qquad (1.23)$$

We note that for large t in the self-trapped regime ($\Lambda > \Lambda_c$) $\delta \to \infty$ and in the diffusive regime $\delta \to 0$ ($\alpha\delta^2 \approx -8\log \mid H_0 \mid$). Physically, this means that in the self-trapping there is an energy transfer to the internal modes of the wave packet, as previously discussed. In Figs.1-2 we plot the density $\mid \psi_n \mid^2$ for different times with Λ in the diffusive region (Fig.1) and in the self-trapped one (Fig.2): the solid lines are the numerical solutions of Eq.(1.10), the dashed lines are the solutions of the variational equations (1.14) and (1.15). In Fig.3 we plot the dispersion $\gamma(t)$ of the wave packet for three different values of Λ (we recall that $\alpha = \gamma^2$): when Λ is in the diffusive region, the width increases with time, and when it is in the self-trapped region reaches a constant value. The numerical discrepancy in the latter case between the numerical result and the variational one is due to the fact the numerical solution of Eq.(1.10) loses, in the self-trapping region, its gaussian shape (as we can see from Fig.2). Furthermore, the growing rate of the width increases (decreases) with Λ for $\Lambda < \Lambda_c$ ($\Lambda > \Lambda_c$): in Fig.4 we report the variational and numerical values of the width of the density vs. Λ/Λ_c after a time $\tau = 10$ (scaled units). The discrepancy at large Λ/Λ_c is due to a slight deviation of the numerical density profile from a gaussian shape.

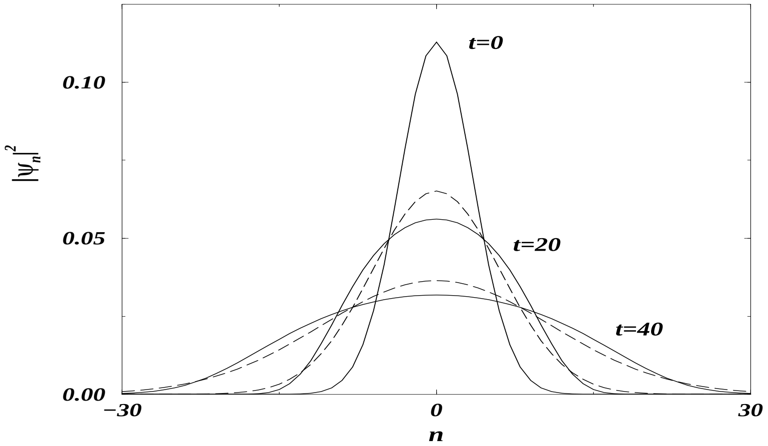

Figure 1.1: Plot of the wave function density $\rho_n =| \psi_n |^2$ at times $t = 0, 20, 40$ with $\Lambda = 1$ in the diffusive region. Numerical values: $p_0 = 0$, $\delta_0 = 0$, $\alpha_0 = 50$. The critical value of Λ is in this case $\Lambda_c = 24.82$. Solid lines: solutions of Eq.(1.10) with 73 sites; dashed lines: solutions of variational Eqs.(1.14) and (1.15).

It is important to remark that the occurrence of the transition between the diffusive and the self-trapped regimes does not depends on the chosen initial conditions. In Fig.5 we choose a steplike initial condition: $\psi_n(t = 0) = const$ for $n = -L, \cdots, L$ and $\psi_n = 0$ elsewhere. For small values of Λ, the population in the interval $\sum_{n=-L}^{L} | \psi_n |^2$ decreases with time (Fig.5a)

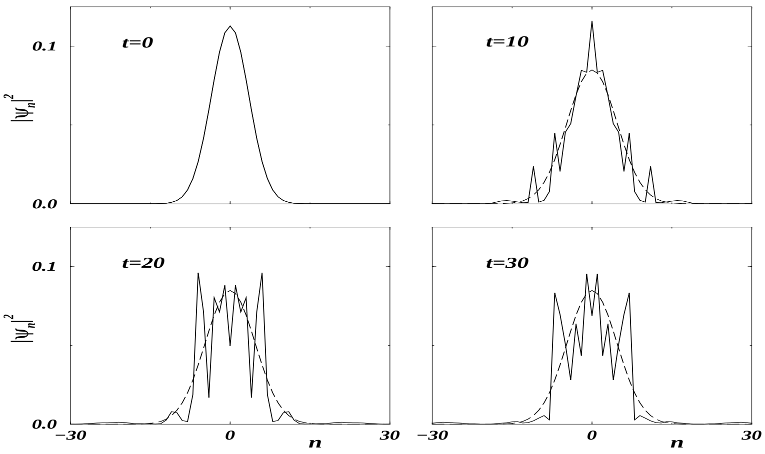

Figure 1.2: Plot of the wave function density at times $t = 0, 10, 20, 30$ with $\Lambda = 100$ in the self-trapping region. The numerical values of the remaining parameters are as in Fig.1.

and the wave function $\psi_n(t)$ gradually spreads out with time (Fig.5c). When Λ is large, to the contrary, the step region remains populated (Fig.5b) and the wave packet well localized (Fig.5d). We observe that the value given by Eq.(1.23), despite it is calculated with gaussian wavefunctions, is in quite good agreement with the numerical critical value. This means, inter alias, that our dynamical phase diagram depends weakly on the details of the density profiles of the localized excitations.

Before to pass to the case of $p_0 \neq 0$, we briefly discuss the size effects. With a finite number of sites, the self-trapping condition is not anymore $\alpha < \infty$, but $\alpha < \alpha_{size}$, where α_{size} is the square of the finite length of the lattice. Proceeding as before, it is possible to show that the effective value at which the transition occurs is related to the critical value (1.23) by the relation

$$\Lambda_c^{eff} = \frac{\Lambda_c}{1 - \sqrt{\alpha_0/\alpha_{size}}}. \tag{1.24}$$

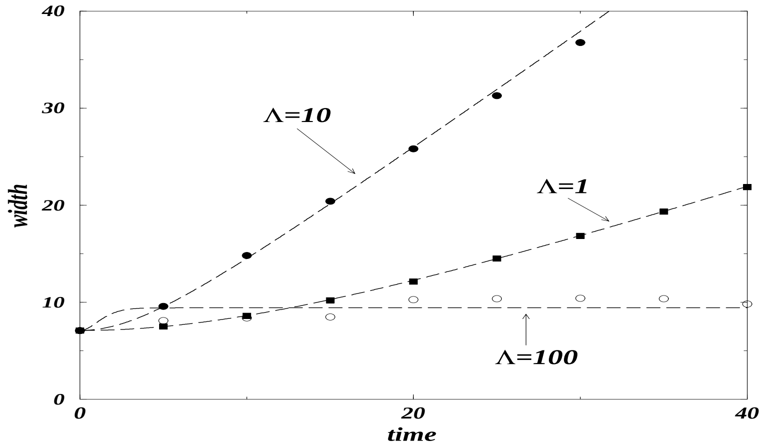

Figure 1.3: Plot of the wave packet width vs. time for $\Lambda = 1, 10, 100$ with the same numerical parameters of Fig.1. Points (respectively filled squares, filled circles and open circles): numerical solution of DNLSE; dashed lines: variational analysis.

Of course, when an infinitely large lattice is used, $\Lambda_c \approx \Lambda_c^{eff}$; moreover, when $\alpha_0 \approx \alpha_{size}$, does not make sense to talk about self-trapping.

Let us consider the case of $p_0 \neq 0$, in which the center of the wave packet moves on the lattice: as already discussed, there are two distinct regimes. When $H_0 > 0$, $\alpha(t) < \alpha_{max}$: this is the self-trapped regime in which the boson wave packet remains localized around few sites. The self-localization is a genuine nonlinear effect, characterized by a diverging effective mass. In particular, the self-trapped wave packet cannot translate along the array: this is a major difference with respect to soliton-like solutions. The limit values for $t \to \infty$ are $\alpha \to \frac{\Lambda^2}{4\pi H_0^2}$, $\delta \to \infty$ and $\dot{\xi} \to 0$.

A diffusive regime occurs when $-\cos p_0 < H_0 \leq 0$. In this case $\alpha(t \to \infty) \to \infty$ and $\dot{\xi} \approx -H_0/\tan p_0 = const$. The transition between the two

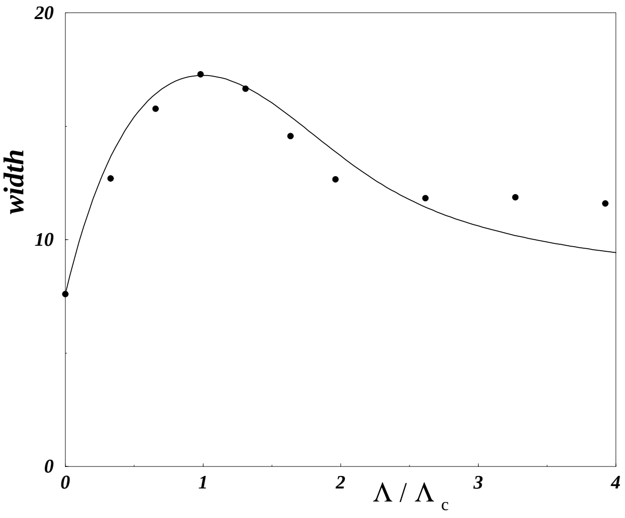

Figure 1.4: Variational (solid line) and numerical (circles) width of the density vs. Λ/Λ_c after the time $\tau = 10$, scaled units (initial values: $p_0 = 0$, $\delta_0 = 0$ and $\gamma_0 = 7$).

regimes occurs at

$$\Lambda_c = 2\sqrt{\pi\alpha_0}\,\cos p_0\, e^{-1/2\alpha_0}. \tag{1.25}$$

With $\Lambda > \Lambda_c$, the ratio between the initial value of the width γ_0 and the limit width $\gamma_{max}(t \to \infty)$ is given by

$$\frac{\gamma_0}{\gamma_{max}} = \frac{\Lambda - \Lambda_c}{\Lambda}. \tag{1.26}$$

In Fig.6 we plot γ_0/γ_{max} vs. Λ/Λ_c. We checked the stability of self-trapping, also considering different initial forms of the wave packet. In Figs.7(a)-7(b) we plot, respectively, the width and the average position for $\Lambda < \Lambda_c$, i.e. for a diffusive case. We see that the center of mass and the width goes to infinite. These two figures have to be compared with Figs.7(c)-7(d), in which the same numerical parameters are used, but opposite $\cos p_0$: we see that the motion of the center of mass is almost the same, but the the increasing rate

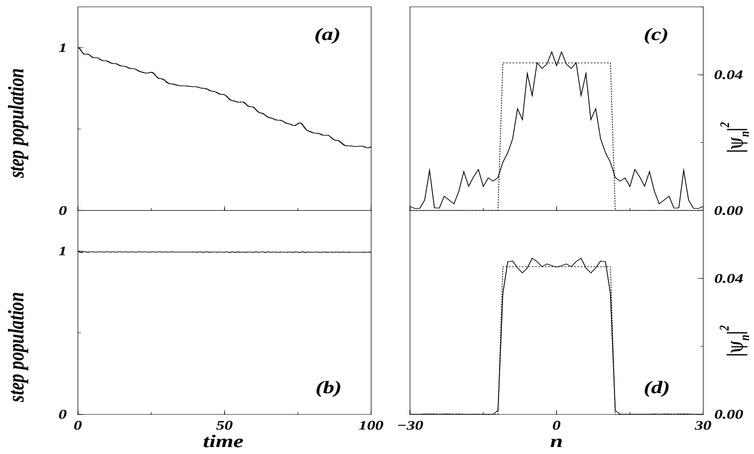

Figure 1.5: (a) Population in the interval $\sum_{n=-L}^{L} \mid \psi_n \mid^2$ vs. time for $\Lambda = 1$. (b) Population vs. time for $\Lambda = 100$. (c) Density profile at $t = 40$ for $\Lambda = 1$ (dotted line: initial condition). (d) Density profile at $t = 40$ for $\Lambda = 1$ (dotted line: initial condition). The numerical simulations are done with 73 sites and $L = 11$. From the numerical solutions, the critical value for the transition is $\Lambda_c \approx 90$, in qualitative agreement with Eqs.(1.23) and (1.24), which give $\Lambda_c \approx 100$.

of the width is much smaller. The reason is that, with the used parameters, Λ is in the breather region, i.e. in a regime in which the width remains finite. A detailed explanation will be presented in the next subsection. The average position is defined as $< n >= \sum_n n \mid \psi_n \mid^2$ and the width by $2\sqrt{< n^2 >}$ with $< n^2 >= \sum_n n^2 \mid \psi_n \mid^2 - < n >^2$.

In Fig.8 we consider a self-trapped state ($\Lambda > \Lambda_c$): the variational prediction is that $\dot{\xi} \to 0$ and that $\xi \to const.$ During the approach to final time, the width increases (and it goes asymptotically to a constant value) and the momentum conjugate to the width goes to infinite. The full numerical solution cannot go to this state, because the transfer of energy to internal state

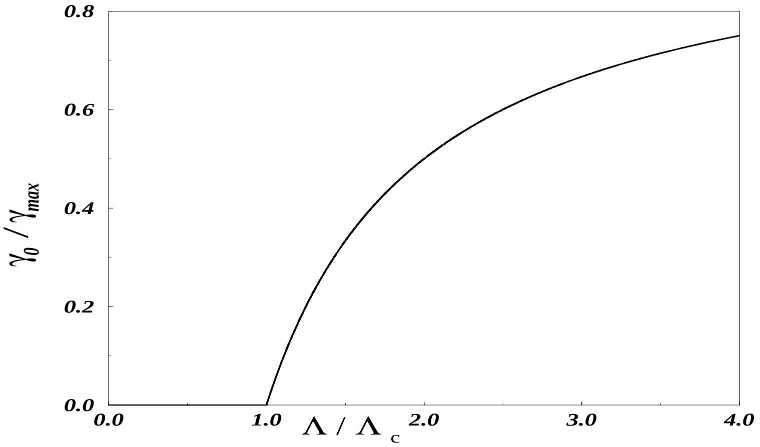

Figure 1.6: Universal curve of γ_0/γ_{max} vs. Λ/Λ_c as in Eq.(1.26).

breaks down the wave packet: when the average position approaches to value predicted from the variational analysis (thick line), the wave packet deform until it breaks: we can think at the asymptotic value as a wall on which the wave packet bounces. In the inset we compare the numerical and the variational average position, where this kind of $self$-bouncing determines a deviation between the two lines. We observe anyway, despite the variational analysis cannot exactly follow the full dynamics in the self-trapping, it can anyway predict the occurrence of the transition and give a very good value for the critical point.

The results of this subsection are summarized in Fig.9, in which the diffusive and the self-trapped regions are reported.

1.4.2 Negative effective mass

In this subsection we discuss the case $\cos p_0 < 0$. We will show that soliton-like structures are present (even if the BEC's interatomic potential

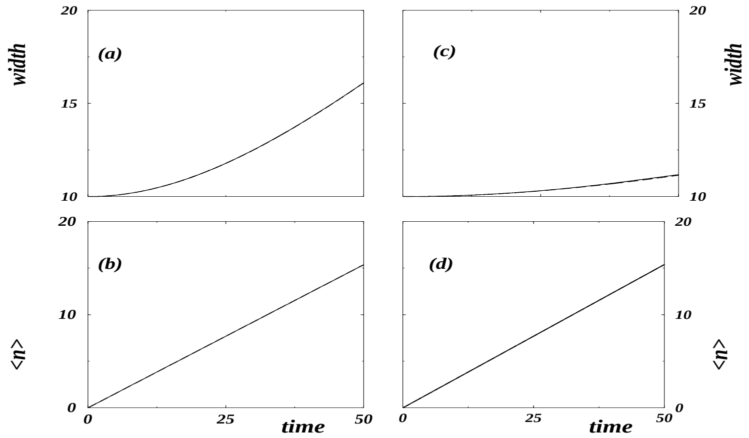

Figure 1.7: Width (a) and average position (b) vs. time for $p_0 = \pi/10$, $\alpha_0 = 100$ and $\Lambda = 0.24$ in the diffusive region (from Eq.(1.25) $\Lambda_c = 33.55$). In (c) and (d) we plot the width and the average position for the same parameters, but opposite $\cos p_0$ ($p_0 = 9\pi/10$). In this case $\Lambda_c = 0.17$ and $\Lambda_{sol} = 0.33$. The variational predictions (dashed lines) are in excellent agreement with the numerical solutions (solid).

is repulsive). By using the results in App.A, we will also discuss the phase diagram which have different regimes: diffusive (in which the boson wave packet spreads out), self-trapped (as in the case $\cos p_0 > 0$), but also breathing (where the center of mass of the wave packet moves with an oscillating width), and solitonic (in which the wave packet shape is exactly preserved during the dynamics).

Intrinsically localized excitations [38, 39], as solitons (shape preserving) and breathers (characterized by internal oscillations), are important channels for energy transport in nonlinear media, such as optical fibres and waveguides [40], polaronic materials [41] and biological molecules [42]. Intense theoretical research is now focusing on the existence of solitons and breathers in a lattice

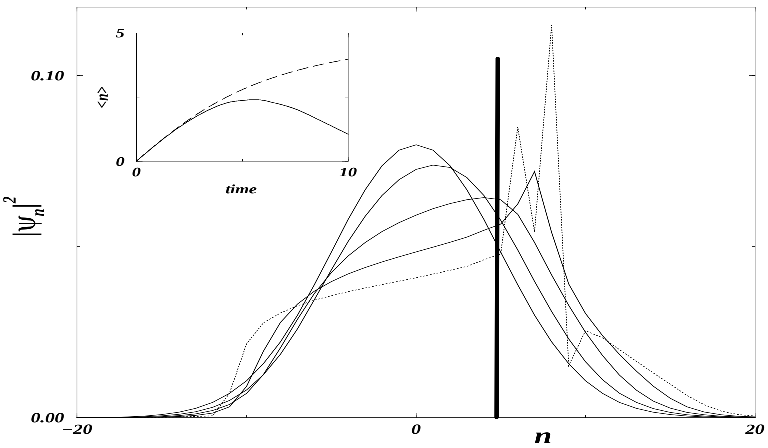

Figure 1.8: Density profiles at times $t = 0, 1.25, 2.5, 3.75$ (solid lines) and at $t = 5$ (dotted) for $p_0 = \pi/4$, $\alpha_0 = 100$ and $\Lambda = 50$ ($\Lambda_c = 24.82$). The thick line represents the asymptotic value predicted from the variational analysis. In the inset the variational (dashed line) and numerical (solid) average position vs. time are plotted.

(often named discrete solitons and discrete breathers (DSB) [40]). Current approaches include the search for exact solutions in some limits [43]; effective (point) particle and variational approaches [44–46]; perturbation around the linearized case and, of course, numerical solutions [16,40]. The occurrence of bright soliton in BEC has been considered in [47]. Dark solitons in BECs has been experimentally studied in [48].

Although intensely studied, DSB have been experimentally observed only quite recently in superconducting ladders of Josephson junctions [49], in antiferromagnet systems [50], in optical waveguides [51] and in low dimensional materials [52].

The discrete solitons/breathers are characterized by a dynamical, self-maintained energy localization, due to both the discreteness and the non-

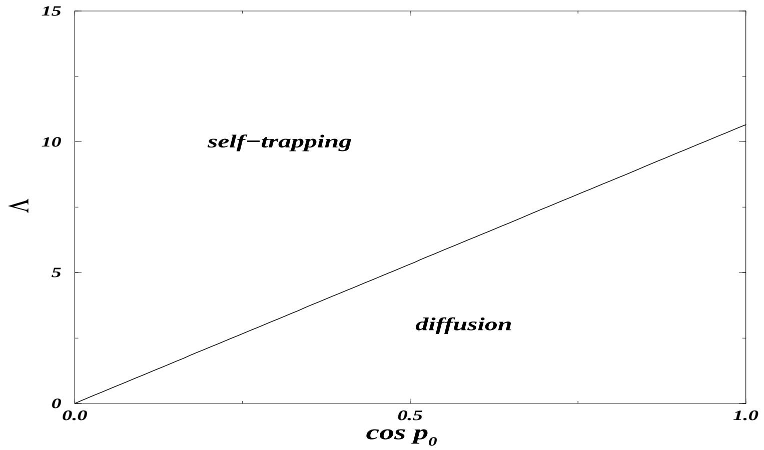

Figure 1.9: Dynamical phase diagram in the horizontal array with $\cos p_0 > 0$: we plot Λ vs. $\cos p_0$, for α_0 fixed ($\alpha_0 = 10$), $\Lambda > 0$ and with initial $\xi_0 = 0$ and $\delta_0 = 0$. Varying α_0 only implies a different slope of solid line, according to Eq.(1.25).

linearity of the underlying equations of motion. The discreteness provides a band structure of the excitation spectrum, while the nonlinearity allows for the tuning of the DSB energy outside the band. The finite energy gap guarantees the (meta-)stability of the DSB's. These, obviously, have a different nature to the "Anderson localizations", created by impurities or imperfections of the lattice [53]; the incorporation of disorder into nonlinear excitations, and the tracing out of its dynamical effects are also important theoretical problems. We will discuss the case of DNLSE with impurities in Chapter 3.

The determination of the phase diagram is done in App.A. In the region $\cos p < 0$ the self-trapping condition is given by $H_0 >\mid \cos p_0 \mid$: the critical value is given by

$$\Lambda_c = 2\sqrt{\pi\alpha_0} \mid \cos p_0 \mid \; (1 - e^{-1/2\alpha_0}). \tag{1.27}$$

For $\Lambda < \Lambda_c$, $\alpha \to \infty$, while for $\Lambda > \Lambda_c$, α remains finite.

A soliton solution can be determined by imposing $\dot{\alpha} = \dot{\delta} = 0$. We find

$$\Lambda_{sol} = 2\sqrt{\frac{\pi}{\alpha_0}} \mid \cos p_0 \mid \, e^{-1/2\alpha_0}. \tag{1.28}$$

For $\Lambda = \Lambda_{sol}$ the center of the wave packet moves with a constant velocity $\dot{\xi}$ and its width remains constant in time. We observe that for $\alpha_0 > 1$, it is $\Lambda_c < \Lambda_{sol}$. In Fig.10 we plot the average position and the width for $\Lambda = \Lambda_{sol}$. Since we are not using periodic boundary conditions (PBC), when he wave packet arrives to the end of the lattice, it hits a wall: since it is soliton, after hitting, it regains its shape. This is illustrated in Fig.11, where we show the profile density at different times.

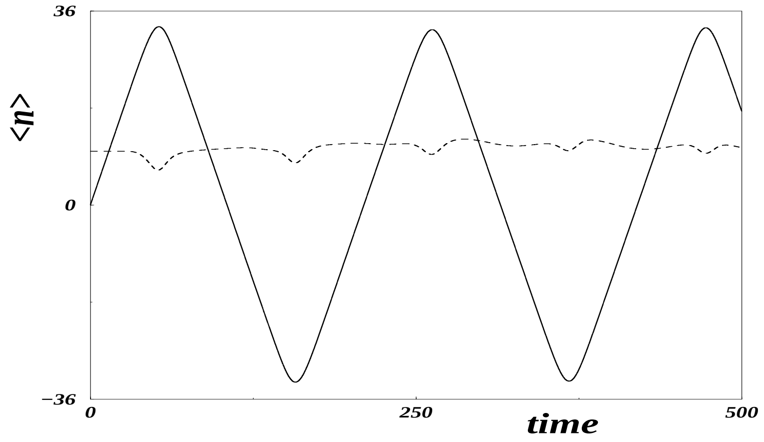

Figure 1.10: Width (dotted line) and average position (solid line) calculated numerically for $\Lambda = \Lambda_{sol}$ and $p_0 = 3\pi/4$ in a finite array of 73 sites.

For $\Lambda_c < \Lambda < \Lambda_{sol}$, $\xi \to \infty$ while $\alpha(t)$ oscillates, corresponding to a breather solution. When $\alpha_0 > 1$, the breather region extends until a value $\Lambda_{breath} > \Lambda_{sol}$: the equation from which it is possible determine Λ_{breath} is reported in App.A. In Fig.12 we plot the density profile at different times when Λ is chosen in the breather region. In Fig.13 the same values are used,

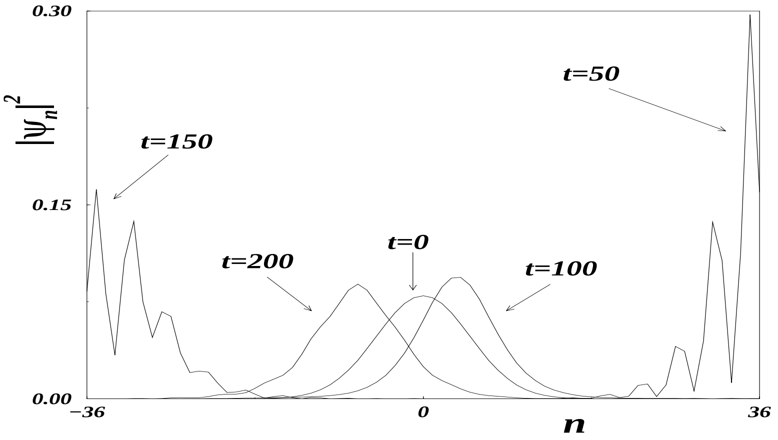

Figure 1.11: Numerical density profile for $t = 0, 50, 100, 150, 200$ for the soliton described in Fig.10.

but with opposite $\cos p_0$: a diffusive solution is obtained.

The dynamical phase diagram which summarizes the results for the case $\cos p_0 < 0$ is given in Fig.14, where the different regimes are plotted. We have to mention that when $\Lambda_c < \Lambda < \Lambda_{breath}$, the variational width oscillates between α_0 and a value smaller than α_0: from numerical analysis, we realized that these breather solutions are rather unstable and therefore the numerical transition from breather to self-trapping is quite softened. Yet, Λ_{breath} is in qualitative agreement with the numerical findings.

Before concluding, we discuss the relation between the present results and the Modulational Instability. As we will show in the following chapter, if we consider a small perturbation on a plane wave $\psi_n \propto e^{ip_0 n}$, stability analysis shows that when $\cos p_0 < 0$ the eigenfrequencies of the linear modes become imaginary driving an exponential growth of small perturbations. When $\cos p_0 > 0$, the plane wave is stable. In the present case, we are considering not a wave plane, but a localized wave function; anyway we expect that we

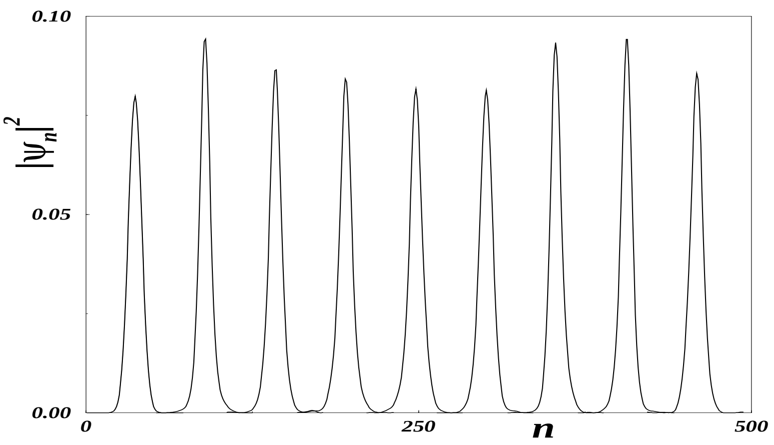

Figure 1.12: Numerical density profiles calculated at different times ($t = 0, 50, 100, \ldots, 400$). The value of Λ is inside the breather region of the dynamical phase diagram ($p_0 = 3\pi/4$, $\gamma_0 = 10$, $\Lambda = 0.24$).

can find the result previously stated by considering the case $\alpha >> 1$. In this case, when $\cos p_0 > 0$, $\Lambda_c \to \infty$ and the self-trapped region disappears: this correspond to the result which there is not modulational instability for $\cos p_0 > 0$. To the contrary, when $\cos p_0 < 0$, then $\Lambda_c \to 0$ and always the system exhibits instability to small perturbation. In Fig.14, this means that we have only self-trapping, as expected.

1.5 Vertical array

In this section we discuss the vertical array, in which the external potential is given by the sum of the laser field and the gravitational potential: $\mathcal{V} = mgx$. This setup has been realized first in the Anderson-Kasevich experiment at Yale [1]. The one-dimensional vertical optical array was created by two counterpropagating laser beams (with wavelength $\lambda = 850nm$). A

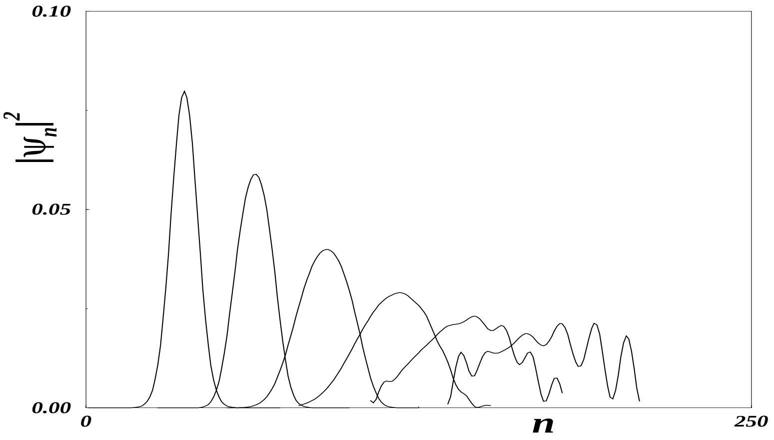

Figure 1.13: The same parameters as in Fig.12, but for $p_0 = \pi/4$.

weakly interacting Bose-Einstein condensate was trapped in ~ 30 wells, situated at the antinodes of the standing optical wave. Each well contained approximately 1000 condensate atoms, with the peak densities matching a gaussian profile. Since the array is oriented vertically, the atoms undergo coherent Bloch oscillations, driven by the interwell gravitational potential. At the edge of the Brillouin zone, a fraction of atoms can Zener tunnel in the higher energy band which, in this specific case, is in the continuum.

The importance of this experiment relies in the fact that a *coherent* leakage of atoms from the trap was observed: the output trap can be viewed as an atom laser whose coherent length ($> 500\,\mu m$) greatly exceeds of the dimensions of the BEC (i.e. the resonator). The time-domain pulses are directly analogous to the output of a mode-locked laser source, in which interference occurs between many properly phased continuous-wave output beams. The nearly constant time interval between successive pulses directly implies that the relative phase associated with each pulse envelope is well defined. The realization of an atom laser is nowadays a very active field of research (see

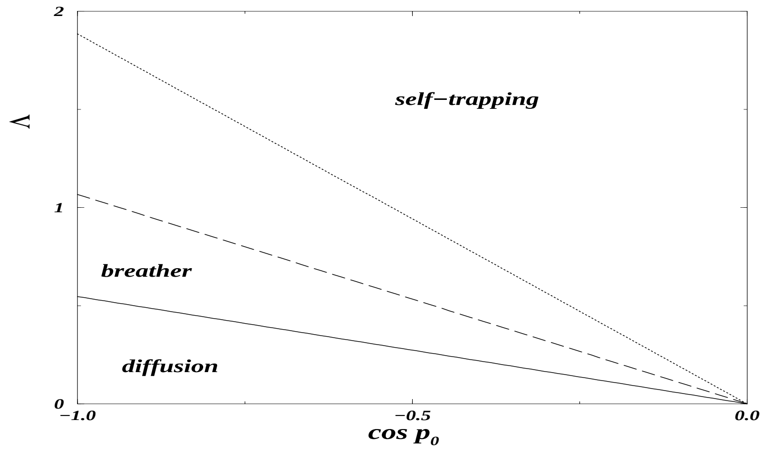

Figure 1.14: Dynamical phase diagram in the horizontal with $\cos p_0 < 0$: the dashed line is Λ_{sol} and it corresponds to solitons, the solid line is Λ_c and the dotted is Λ_{breath}. In the region $\Lambda_c < \Lambda < \Lambda_{breath}$, the variational analysis predicts breather solutions. As in Fig.9, α_0 is fixed ($\alpha_0 = 10$), $\Lambda > 0$ and with initial $\xi_0 = 0$ and $\delta_0 = 0$.

references indicated in [54]).

Furthermore, the coherent output $from$ the laser is an indirect evidence of the occurrence of Josephson oscillations in the trap. In the ac Josephson effect, application of a dc voltage across the junction leads to an alternating current. Here the chemical potential $\Delta\mu = mg\lambda/2$ between adjacent traps (whose distance is precisely $\lambda/2$) is determined by the gravitational potential and acts as an external dc voltage: in this way a coherent alternating current with frequency $\omega_J = \Delta\mu/\hbar$ is obtained. In the following chapter we will discuss an experiment in which a direct observation of Josephson oscillations is reported.

The main features of the Anderson-Kasevich experiment can be discussed in terms of the collective coordinate approach discussed in the previous section. In order to get the on-site energies (1.8), we use gaussian wavefunctions localized in the different traps

$$\Phi_n(\vec{r}) = Ce^{-(x-x_n)^2/2\sigma_x^2}e^{-y^2/2\sigma_y^2}e^{-z^2/2\sigma_z^2} \tag{1.29}$$

with C normalization factor, $x_n = n\lambda/2$ center of the n-th well along the optical trap and $\sigma_{x,y,z}$ widths to determine variationally. We remark that doing this approximation we are neglecting implicitly the variation of the widths along the transverse degrees of freedom. By substituting the gravitational potentials $\mathcal{V} = mgx$, we find simply

$$\epsilon_n = mg\frac{\lambda}{2}n \tag{1.30}$$

without dependence on the widths $\sigma_{x,y,z}$ of the localized wavefunctions Φ_n.

In this way, we find $E_n = \epsilon_n/2K = \omega n$, where

$$\omega = \frac{mg\lambda}{4K} : \tag{1.31}$$

by substituting in Eq.(1.17) we get

$$V(\alpha, \xi) = \omega\xi \tag{1.32}$$

as expected. The variational equations of motion read

$$\begin{cases} \dot{p} = -\omega \\ \dot{\xi} = \sin p \, \cdot \, e^{-\eta} \end{cases} \tag{1.33}$$

and

$$\begin{cases} \dot{\delta} = \cos p\Big(\frac{4}{\alpha^2} - \delta^2\Big)e^{-\eta} + \frac{2\Lambda}{\sqrt{\pi}\alpha^3} \\ \dot{\alpha} = 2\alpha\delta\cos p \, \cdot \, e^{-\eta} \end{cases} \tag{1.34}$$

from which

$$p(t) = -\omega t + p_0 \tag{1.35}$$

It is well known that single atoms in a tilted washboard potential oscillate among sites at the Bloch frequency. This regime is described by Eqs.(1.33) and (1.34) with $\Lambda = 0$, corresponding to a negligible mean field condensate interaction. This is, precisely, the regime investigated in [1] in which a coherent output was observed: indeed a simple variational estimate based on Eq.(B.1) gives $\Lambda \simeq 0.5$ and $\omega \simeq 2$. Furthermore, $K \simeq 1.5 \cdot 10^{-24}\, erg$ and the scaled time is in units of $\hbar/2K = 0.35\, ms$. In the limit $\Lambda \to 0$, the Eqs.(1.33) and (1.34) can be solved exactly. First, we observe that from $dH/dt = 0$ we can get

$$\cos p \cdot \frac{d}{dt} e^{-\eta} = -\frac{\Lambda \dot{\alpha}}{4\sqrt{\pi \alpha^3}}$$

from which we can see that with $\Lambda = 0$, $e^{-\eta}$ is a conserved quantity. Let us put $\xi_0 = 0$ and $\delta_0 = 0$: therefore $e^{-\eta} = e^{-\eta(t=0)} = e^{-1/2\alpha_0}$. Since the (conserved) energy is $H_0 = -\cos p_0 \cdot e^{-1/2\alpha_0}$, we find

$$\xi(t) = A[\cos(\omega t - p_0) - \cos p_0] \tag{1.36}$$

where

$$A = -\frac{H_0}{\omega \cos p_0} = \frac{e^{-1/2\alpha_0}}{\omega}. \tag{1.37}$$

We see from these equations that the amplitude A of the Bloch oscillations does not depends on the initial velocity and it is inversely proportional to the strength of the linear external field; furthermore, the greater is initially the width of the wave packet, the greater is the amplitude of the Bloch oscillations.

To obtain the solution for the width, we observe that the function

$$\mathcal{X} \equiv \alpha \delta$$

satisfies the equation $\dot{\mathcal{X}} = -8A\omega \log(A\omega)\cos(\omega t - p_0)$. Since $\mathcal{X}(t=0) = 0$, integrating we obtain

$$\mathcal{X}(t) = -8A\log(A\omega)[\sin(\omega t - p_0) + \sin p_0] :$$

by using the fact that $\dot{\alpha} = 2\mathcal{X}e^{-\eta}\cos p$, we get finally

$$\alpha(t) = 4A^2 \log A\omega\{\cos[2(\omega t - p_0)] - \cos 2p_0 - 4\sin p_0 \sin(\omega t - p_0) - 4\sin^2 p_0\} + \alpha_0 \tag{1.38}$$

and

$$\delta(t) = -\frac{8A\log A\omega\,[\sin(\omega t - p_0) + \sin p_0]}{\alpha(t)}. \tag{1.39}$$

From Eq.(1.38) we see that when $p_0 = 0$, then the width oscillates at a frequency twice than the center of mass. In Fig.15 we show that the Bloch oscillations described by the variational ansatz (dashed line) are in excellent agreement with the full numerical solution of the DNLSE (solid line).

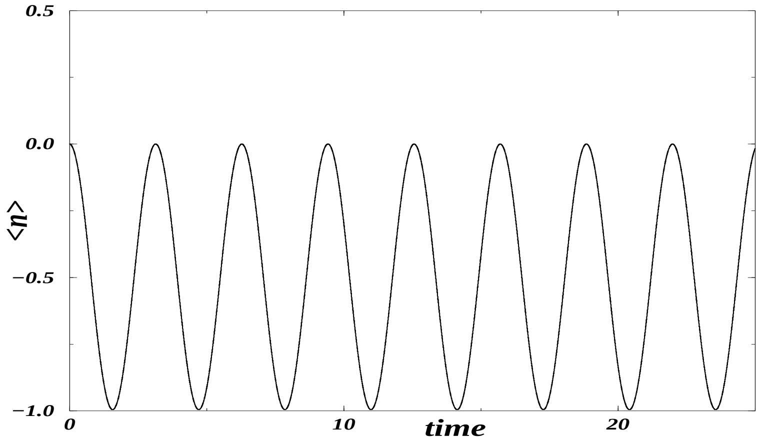

Figure 1.15: Numerical (solid line) and variational (dashed) average position of the density in the vertical array ($\omega = 2$, $\Lambda = 0$ and initial $p_0 = 0$, $\delta_0 = 0$, $\alpha_0 = 100$).

Let us now consider the effect of the nonlinearity on the Bloch oscillations. This has been studied experimentally in [1] by increasing the density in each well, and observing a degradation in the interference pattern. With $\Lambda \neq 0$ we have:

$$\ddot{\xi} + \frac{\Lambda\delta}{2\sqrt{\pi}\gamma}\dot{\xi} + \omega^2\xi = \omega H_0 - \frac{\Lambda\omega}{2\sqrt{\pi}\gamma}. \tag{1.40}$$

The Eq.(1.40) displays an effective damping term proportional to the velocity $\dot{\xi}$. We stress that the dynamics is fully Hamiltonian, and real dissipative processes are absent. For $t \to \infty$, α tends to a constant value α_{fin} and $\delta \sim \frac{2\Lambda}{\sqrt{\pi\alpha_{fin}^3}}t$, so the term $\Lambda\delta$ has the correct positive sign (for large t). The apparent damping is the consequence of a diverging effective mass of the wave packet $m^* \sim e^{\frac{\Lambda^2}{2\pi\alpha_{fin}^2}t^2}$, which stops the Bloch oscillations. The oscillation roughly decreases as

$$\xi(t) \sim -A(1 - e^{-\frac{\Lambda^2 t^2}{2\pi\alpha_{fin}^2}} \cos\omega t). \tag{1.41}$$

From Eq.(1.41), we can see that the time τ_{dec} in which the Bloch oscillation stops is of order

$$\tau_{dec} \sim \frac{\sqrt{2\pi}\alpha}{\Lambda} \tag{1.42}$$

We observe that with typical experimental numbers of [1] this time is of order $\sim 1s$ and does not forbid the observation of the coherent leakage of atoms from the trap. In Fig.16 (solid line) we show the variational Bloch dynamics with a nonlinear parameter $\Lambda = 10$ and initial values $\xi_0 = 0$, $p_0 = 0$ and $\delta_0 = 0$. The solid line shows the full numerical solution of the DNLSE, in good agreement with the analytical result (dashed line). The discrepancy at $t > 10$ is due to the breaking of the gaussian wave packet in the numerical simulation.

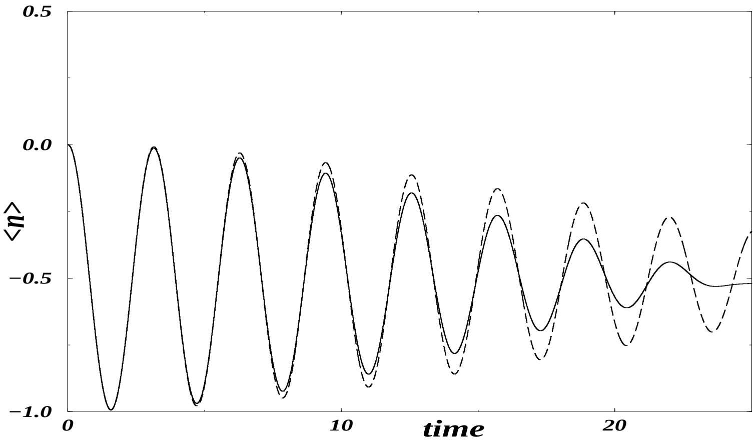

Figure 1.16: Coherent destruction of Bloch oscillations: numerical (solid line) and variational (dashed) average position of the density in the vertical array ($\omega = 2$, $\Lambda = 10$ and initial $p_0 = 0$, $\delta_0 = 0$, $\alpha_0 = 100$).

The effect of the coherence of the Bloch oscillations can be clearly seen by looking at the phases of the condensates in the different traps: when $\Lambda = 0$, the Fourier transform of ψ_n is well peaked around $p(t)$ which is running. This means that $\phi_n \propto pn$ (we recall that $\psi_n(t) = \sqrt{n_n(t)}\, e^{i\phi_n(t)}$). This reflects in the coherence of the output. When $\Lambda \neq 0$, at times of order τ_{dec}, the wave packet is broken down and the phases deviate from the relation $\phi_n \propto pn$, i.e. the Fourier transform is broken. This effect manifests, in the numerical analysis of Eq.(1.10), as a distortion of the on-site phases, as showed in Fig.17.

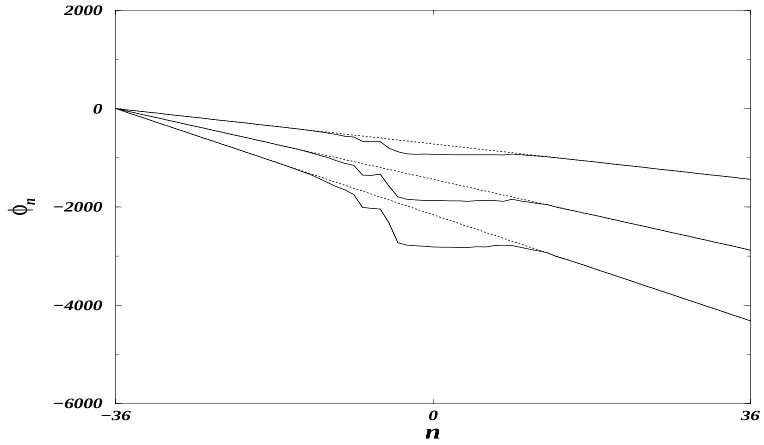

Figure 1.17: On-site phases ϕ_n at different times (from the top of the figure $t = 10, 20, 30$). Dotted lines are for $\Lambda = 0$ and solid lines for $\Lambda = 300$. Furthermore: $N = 73$ sites, $\omega = 2$ and initial $p_0 = 0$, $\delta_0 = 0$, $\alpha_0 = 100$.

Chapter 2

Josephson junction arrays

2.1 Introduction

In this chapter we discuss the experiment realized at the LENS in Firenze [8], where for the first time has been reported the direct observation of a Josephson current in an array of weakly coupled Bose-Einstein condensates. The array, as discussed in the previous chapter, is created by a laser standing-wave, with the condensates trapped in the valleys of the periodic potential, and weakly coupled by the interwell barriers. By varying the laser power, the energy barrier and therefore the microscopic tunneling rate (i.e. the Josephson coupling energy) can be experimentally tuned and different physical regimes can be investigated.

By suddenly moving the magnetic trap, the condensates are displaced from the equilibrium position in the harmonic + optical potential. For small displacement it is observed a coherent current in the trap: the phases of the condensates are locked and the BECs tunnel all together from a well to the neighbour one. The coherence of multiple tunneling between adjacent wells is continuously probed by observing the interference patterns of the condensates when the magnetic and potential traps are turned off. As discussed in the previous chapter, the system is described by a discrete nonlinear Schrödinger equation (DNLSE), with an harmonic external driven potential: we will show that the predictions of the full Gross-Pitaevskii equation which describes the system are reproduced quite well from the DNLSE. Considering the DNLSE and introducing as collective coordinates the center of mass ξ of the condensates and the phase difference $\Delta\phi$ between condensates in adjacent wells, it is possible to show that ξ and $\Delta\phi$ satisfies the equation of a pendulum: these equations have the form of the standard Josephson relation for the current and the phase difference.

From the Josephson equations it is possible to show that the square of the small-amplitude oscillation frequency is proportional to the microscopic tunneling rate of each condensate through the barriers, and provides a direct measurement of the Josephson critical current as a function of the intermediate barrier heights. We find the expected result that the oscillation frequency *with* the lattice is smaller than the frequency *without* the lattice: by increasing the laser power (i.e. the height of the barriers), the frequency decreases and the time of the oscillations increases: the barriers slow down the oscillations.

The frequency calculated from the Gross-Pitaevskii equation is in agreement with the experimental findings, and both are in reasonable agreement with a variational estimate of the microscopic tunneling rate. An important consequence of this is that we have a well defined way to calculate the Josephson coupling energy. We will show that when the laser power is high enough (i.e. the Josephson energy is low enough), quantum effects should be important. Moreover, there is a threshold for a quantum transition between the superfluid region, which has been investigated in the experiments at LENS discussed in this chapter, and the region of the Mott insulator. We give an estimate of the needed power of the laser: we think that this can be a very stimulating field of future researches.

The array of BECs also have a very interesting and seemingly counterintuitive property: with a large displacement of the harmonic trap, the condensates stop on a side of the harmonic potential. This behavior is a clear manifestation of a dynamical instability. Indeed, the study of the variational equations found in the previous chapter shows that when $\Delta\phi$ reaches $\pi/2$ during the oscillations, the system should be unstable. This is the occurrence in our particular system of a very general feature of the nonlinear media (discrete as well as continuous): the so-called Modulational Instability (MI). Using solid-state terminology and making a connection with the previous chapter, the instability occurs when the effective mass becomes singular. The reason of the occurrence of the MI can be clearly understood by doing a stability analysis of the DNLSE: when $\cos\Delta\phi < 0$, the eigenfrequencies of the linear modes becomes imaginary and there is an exponential growth of small perturbations of the carrier wave.

By using the DNLSE, we can estimate the critical value for the displacement: this depends on the energy of the interwell barrier. In this way we can tune the experimental parameters in order to have or not the modulational instability. Another important consequence of the MI is that it puts precise conditions on the stability and on the maximum possible velocity of the wave propagation in such kind of lattice.

The plan of the chapter is the following: in section 2.2 we discuss the Josephson oscillations for small displacements of the magnetic trap and we derive the pendulum equations. The experimental data are also reported. In section 2.3 a discussion of the behavior of the Josephson energy vs. the laser power is reported and an estimate of the critical value for the quantum transition is given. In section 2.4 the MI in an arrays of weakly coupled BECs is discussed and preliminary experimental results are shown.

2.2 Josephson currents in arrays of weakly coupled condensates

The existence of a Josephson current through a potential barrier between two superconductors or between two superfluids is a direct manifestation of macroscopic quantum phase coherence [55, 56]. The first experimental evidence of a current-phase relation was observed in superconducting systems soon after the Josephson effect was proposed in 1962 [57], whilst verification in superfluid Helium has been presented only recently owing to the difficulty of creating weak links in a neutral quantum liquid [58, 59].

The experimental realization of Bose-Einstein condensates (BEC) of weakly interacting alkali atoms has provided a route to study neutral superfluids in a controlled and tunable environment and to implement novel geometries for the connection of several Josephson junctions so far unattainable in charged systems.

A Josephson junction (JJ) is a simple device made of two coupled macroscopic quantum fluids [56]. If the coupling is weak enough, an atomic mass current I flows across the two systems, driven by their relative phase $\Delta\phi$ as:

$$I = I_c \sin \Delta\phi \tag{2.1}$$

where I_c is the "Josephson critical current", namely the maximal current allowed to flow through the junction. The relative phase dynamics, on the other hand, is sensitive to the external and internal forces driving the system:

$$\hbar \frac{d}{dt} \Delta\phi = \Delta V \tag{2.2}$$

with ΔV being the chemical potential difference between the two quantum fluids. The arrays of JJs are made of several simple junctions connected in various geometrical configurations. In the last decade such systems have attracted much interest, due to their potential for studying quantum phase transitions in systems where the external parameters can be readily tuned [60]. Recently, the creation of simple quantum-logic units and more complex quantum computer schemes have been discussed [61]. A great level of accuracy has been reached in the realization of two- and three-dimensional superconducting JJ arrays [60]. One dimensional (1D) geometries are much more difficult to realize, due to the unavoidable presence of on site frustration charges which destroy the collective phase coherence. 1D JJ arrays with neutral superfluids (such as Bose-Einstein condensates), on the other hand, can be accurately tailored, and open the possibility to observe directly several remarkable phenomena not accessible to other systems [35]. First experiments with BECs held in a vertical optical lattice have shown the spatial and temporal coherence of condensate waves emitted at different heights of the gravitational field [1]. More recently, the degree of phase coherence among different sites of the array [6] has been explored in the BEC ground state configuration.

We discuss in this section the realization of a one-dimensional array of JJs by loading a BEC into an optical lattice potential generated by a standing-wave laser field. The current-phase dynamics, driven by an external harmonic oscillator potential provided by an external magnetic field, maps on a pendulum-like equation and we have performed a measurement of the critical Josephson current as a function of the interwell potentials created by the light field.

In the experiment, BECs of ^{87}Rb atoms are produced in the ($F = 1$, $m_F = -1$) state confined by a cylindrically symmetric harmonic magnetic trap and a blue detuned laser standing-wave, superimposed on the axis of the magnetic trap [11]. The cylindrical magnetic trap is divided into an array of disk shaped traps by the light standing-wave. By varying the intensity of the superimposed laser beam (detuned 150 GHz to the blue of the D1 transition at $\lambda = 795\,\mathrm{nm}$) up to $14\,\mathrm{mW/mm^2}$ we can vary the interwell barrier energy V_0 from 0 to $5E_R$ where $E_R = h^2/2m\lambda^2$ is the recoil energy of an atom (of mass m) absorbing one of the lattice photons. The BEC is prepared by loading $\sim 5 \times 10^8$ atoms in the magnetic trap and cooling the sample via RF-forced evaporation until a significant fraction of condensed atoms is produced. We then switch on the laser standing-wave and continue the evaporation ramp until no thermal component is experimentally visible. This ensures that the system reaches the ground state of the combined trap. The BEC splits in the wells of the optical array: the distance between the wells is $\lambda/2$ and ~ 200 wells are typically occupied, with ~ 1000 atoms in each well. The interwell barrier energy V_0, and therefore the tunneling rate, is controlled by varying the intensity of the laser, chosen to be much higher than the condensate chemical potential μ. Note that μ ranges between $\mu \approx 0.10\, V_0$ for $V_0 = 2\, E_R$ to $\mu \approx 0.04\, V_0$ for $V_0 = 5\, E_R$. Each couple of condensates in neighbouring wells therefore realizes a bosonic JJ, with a critical current I_c depending on the laser intensity.

The condensate order parameter satisfies the Gross-Pitaevskii equation

$$i\hbar \frac{\partial \Psi}{\partial t} = -\frac{\hbar^2}{2m} \nabla^2 \Psi + [V_{ext} + g_0 \mid \Psi \mid^2] \Psi \tag{2.3}$$

where

$$V_{ext}(\vec{r}) = V_0 \cos^2(kx) + \frac{1}{2} m [\omega_x^2 x^2 + \omega_r^2 (y^2 + z^2)] \tag{2.4}$$

where $k = 2\pi/\lambda$ (we recall that $\lambda = 795nm$). The axial and radial frequencies of the magnetic trap are respectively $\omega_x = 2\pi \times 9Hz$ and $\omega_r = 2\pi \times 92Hz$. The potential (2.4) along the x direction is plotted in Fig.1A.

We can describe the dynamics as discussed in Chapter 1: we recall briefly the most important results of that chapter. We decompose the condensate order parameter as a sum of wavefunctions localized in each well of the periodic potential (tight-binding approximation):

$$\Psi(\vec{r}, t) = \sqrt{N_T} \sum_j \psi_j(t) \Phi_j(\vec{r}) \tag{2.5}$$

where N_T is the total number of atoms and $\psi_j = \sqrt{n_j(t)}\, e^{i\phi_j(t)}$ is the j-th amplitude, with the fractional population $n_j = N_j/N_T$ and the number of particles N_j and the phase ϕ_j in the trap j.

The validity of assumption (2.5) has been discussed in the previous chapter. It relies on the fact that the height of the interwell barriers is much higher than the chemical potential. We will prove by a variational calculation that

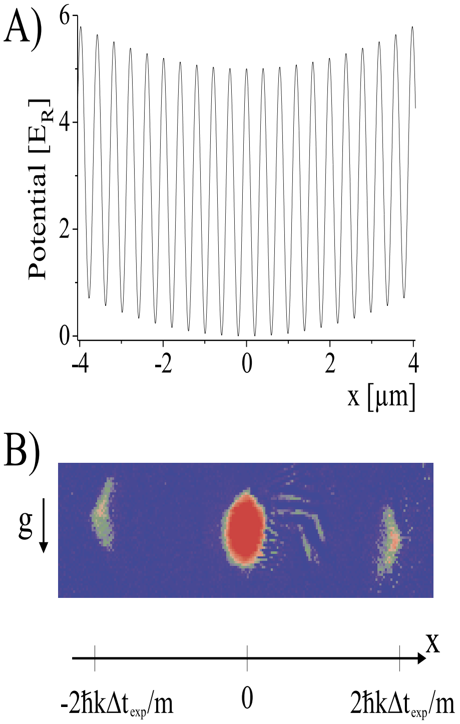

Figure 2.1: A) Combined potential of the optical lattice and the magnetic trap in the axial direction. The curvature of the magnetic potential is multiplied by a factor of 100 for clarity. B) Absorption image of the BEC released from the combined trap. The expansion time was $26.5ms$ and the optical potential height was $5E_R$.

this assumption is verified in most of the range of our experimental parameters. The validity of the tight-binding approximation is also based on the fact that the tunneling of atoms in the higher energy band is energetically forbidden: since the gap is $\sim 5E_R$, the potential energy $\frac{1}{2}m\omega_x^2\left(\frac{\lambda}{2}\right)^2 j^2$ for that would require $j \sim 500$, i.e. displacements three times larger than the condensate dimensions. In the following we will compare the ground state which we found with the ground state obtained taking into account the variation of the widths in the transverse directions. As previously discussed, in the present case the ansatz (2.5) can well describe the bulk properties of the system.

The wavefunction $\Phi_j(\vec{r})$ of the condensate in the j-th site of the array overlaps in the barrier region with the wavefunctions $\Phi_{j\pm 1}$ of the condensates in the neighbour sites. Therefore, the system realizes an array of weakly coupled condensates, whose equation of motion satisfies a discrete nonlinear Schrödinger equation:

$$i\hbar\frac{\partial\psi_n}{\partial t} = -K(\psi_{n-1}+\psi_{n+1}) + (\epsilon_n + U \mid \psi_n \mid^2)\psi_n, \tag{2.6}$$

where, recalling Eqs.(1.7)-(1.9), the tunneling rate is $K \simeq -\int d\vec{r}\,\big[\frac{\hbar^2}{2m}\vec{\nabla}\Phi_n \cdot \vec{\nabla}\Phi_{n+1} + \Phi_n V_{ext}\Phi_{n+1}\big]$, the on-site energies are $\epsilon_n = \int d\vec{r}\,\big[\frac{\hbar^2}{2m}(\vec{\nabla}\Phi_n)^2 + V_{ext}\Phi_n^2\big]$ and the nonlinear coefficient is $U = g_0 N_T \int d\vec{r}\,\Phi_n^4$. Both the Hamiltonian $\mathcal{H} = \sum_j[-K(\psi_j\psi_{j+1}^* + \psi_j^*\psi_{j+1}) + \epsilon_j \mid \psi_j \mid^2 + \frac{\Lambda}{2} \mid \psi_j \mid^4]$ and the norm $\sum_j n_j = 1$.

To evaluate the coefficients of the DNLSE (2.6), we use the variational ansatz given in section 1.4:

$$\Phi_n(\vec{r}) = Ce^{-(x-x_n)^2/2\sigma_x^2}e^{-y^2/2\sigma_y^2}e^{-z^2/2\sigma_z^2} \tag{2.7}$$

with C normalization factor, $x_n = n\lambda/2$ center of the n-th well along the optical trap and $\sigma_{x,y,z}$ widths to determine variationally. The details of the calculation of K, ϵ_n, U are in App.B. It is found

$$\epsilon_n = \Omega n^2 \tag{2.8}$$

where

$$\Omega = \frac{1}{2}m\omega_x^2\big(\frac{\lambda}{2}\big)^2 = 1.54\times 10^{-5}E_R. \tag{2.9}$$

The simple variational estimate discussed in App.B gives for $V_0 = 3E_R$ the values $K \sim 0.07E_R$, $\Lambda \sim 12\,E_R$ and a chemical potential $\mu \sim 0.06\,V_0$ much lower than the interwell potential V_0. We observe that the wavefunctions Φ_j, as well as the tunneling rate K, depend on the height of the energy barrier V_0.

Although we can approximate the condensates in each lattice site as having their own wavefunctions, tunneling between adjacent wells lock the phases of the different condensates. As a result when the condensates are released from the combined trap they will show an interference pattern. This pattern consists of a central peak plus a symmetric comb of equally spaced peaks separated by $\pm 2\hbar k_l t_{exp}/m$ where k_l is the wave vector of the trapping laser and t_{exp} is the expansion time. In practice one can think of the far field intensity distribution of a linear array of dipole antennas all emitting with the same phase. A complementary point of view is to regard the density distribution after expansion as the Fourier transform of the trapped one, i.e. the momentum distribution. It is easy to show that the sum of De Broglie waves corresponding to momentum states integer multiples of $\pm 2\hbar k_l$ is the sum of localized wavefunctions of Eq.(2.5). The expanded cloud density distribution (Fig.1B and Fig.2) consists of three distinct atomic clouds spaced by $\sim 306\,\mu\mathrm{m} \simeq 2\hbar k_l t_{exp}/m$ with the two external clouds corresponding to the first order interference peaks, each containing roughly 10% of the total number of atoms. When there is not coherence, we have not longer the three peaks. The interference pattern therefore provides us with information about the relative phase of the different condensates [3, 6], indeed by repeating the experiment with thermal clouds, even with a temperature considerably lower than the interwell potential, we did not observe the interference pattern.

We remark that this situation is different from the Bragg diffraction of a

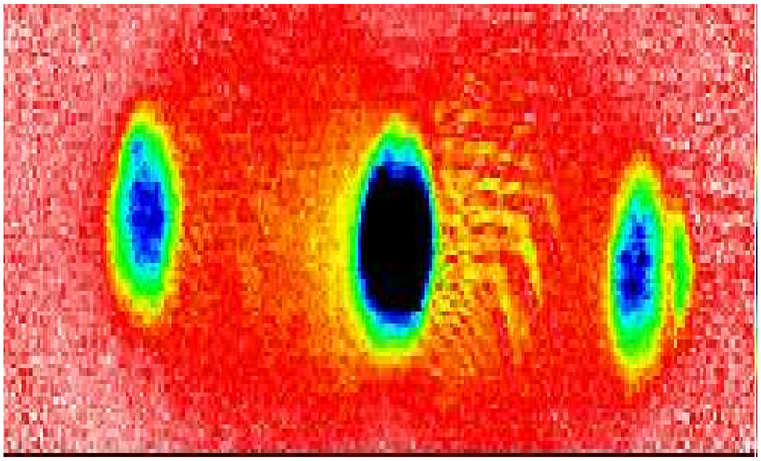

Figure 2.2: Another absorption image featuring the three peaks.

condensate released from a harmonic magnetic trap [62], where the condensate is diffracted by a laser standing-wave. In our case it is the ground state of the combined magnetic harmonic trap plus optical periodic potential that by expansion produces an interference pattern. For the time scales of our experiment the relative intensities of the three interference peaks do not depend on the time the atoms spend in the optical potential indicating that the steady state system has been reached. In absence of external perturbations the condensate remains in the state described by Eq. (2.5) with a lifetime of $\sim 0.3\,\mathrm{s}$ at the maximum light power, limited by scattering of light from the laser standing-wave.

In the ground state configuration the Bose-Einstein condensates are distributed among the sites at the bottom of the parabolic trap. If we suddenly displace the magnetic trap along the lattice axis by a small distance $\sim 30\,\mu\mathrm{m}$ (the dimension of the array is $\sim 100\,\mu\mathrm{m}$) the cloud will be out of equilibrium and will start to move. As the potential energy that we give to the cloud is still smaller than the interwell barrier each condensate can move along the magnetic field only by tunneling through the barriers. A collective motion can only be established at the price of a well definite phase coherence among the condensates. In other words, the relative phases among all adjacent sites should remain locked together in order to preserve the ordering of the collective motion. The locking of the relative phases will again show up in the expanded cloud interferogram.

For not too large displacements, we observe a coherent collective oscillation of the condensates, i.e. we see the three peaks of the interferogram of the expanded condensates oscillating in phase thus showing that the quantum mechanical phase is maintained over the entire condensate (Fig.3A). In the top part of the figure we show the positions of the three peaks as a function of time, and compared with the motion of the condensate in the same displaced magnetic trap but in absence of the optical standing-wave (we refer to this as "harmonic" oscillation). The motion performed by the center of mass of the condensate is an undamped oscillation at a substantially lower frequency than in the "harmonic" case. We will comment on this frequency shift later, now we would like to further stress the coherent nature of the oscillation. To do so we repeat the same experiment with a thermal cloud. In this case, although individual atoms are allowed to tunnel through the barriers, no macroscopic phase is present in the cloud and no motion of the center of mass should be observed. The center of mass position of the thermal clouds is also reported in Fig.3B together with the "harmonic" oscillation of the same cloud in absence of the optical potential. As can be clearly seen the thermal cloud does not move from its original position in presence of the optical lattice.

We now turn back to the discussion of the frequency reduction observed in the oscillation of the pure condensate in presence of the optical lattice. The current flowing through the junction between two quantum fluids has a maximum value, the critical Josephson current I_c, which is directly proportional to the tunneling rate K. The existence of such a condition essentially limits the maximum velocity at which the condensate can flow through the interwell barriers and therefore reduces the frequency of the oscillations. As a consequence we expect a dependence of the oscillation frequency from the tunneling rate.

Before to derive the Josephson equations which describe the system in the regime of small displacements of the magnetic trap, we want discuss the ground state of the DNLSE (2.6). As the number of atoms is large the "kinetic" energy term of DNLSE is small respect to the potential and nonlinear terms, and the population density profile of the ground state is simply given by an inverted discrete parabolic profile:

$$\mid \psi_n \mid^2_{G.S.} = \frac{\mu - \Omega n^2}{U} \tag{2.10}$$

with $n < n_{inv}$ and the inversion point given by

$$n_{inv} \simeq \sqrt{\frac{\mu}{\Omega}}. \tag{2.11}$$

The chemical potential μ is fixed by the condition $\sum_n \mid \psi_n \mid^2 = 1$: by substituting the sums with integrals we get the result

$$\mu = \left(\frac{3}{4} U \Omega^{1/2}\right)^{2/3} \tag{2.12}$$

It is important to remark that the fact that K and U does not depends on the lattice site n is a consequence of the fact we are using in the transverse directions average widths $\sigma_{y,z}$ which does not depend on n. A more detailed calculation was done in the the work by *Pedri et al.* [33], where it was calculated the number of particles in the ground state by taking into account the variation of the widths in the transverse direction (in our formalism, this means that U and K are site-dependent): their result is

$$\mid \psi_k \mid^2_{G.S.} = \frac{15}{16k_M}\left(1 - \frac{k^2}{k_M^2}\right)^2 \tag{2.13}$$

where

$$k_M^2 = \frac{2\hbar\tilde{\omega}}{m\omega_x^2(\lambda/2)^2}\left(\frac{15}{8\sqrt{\pi}}N_T\frac{a}{a_{ho}}\frac{\lambda}{2\sigma}\right)^{2/5}$$

with $\tilde{\omega} = (\omega_x\omega_r)^{1/3}$, $a_{ho} = \sqrt{\hbar/m\tilde{\omega}}$, a the s-wave scattering length and σ characterizing the width of the condensates on each well (for $V_0 = 4E_R$ it is $\sigma/(\lambda/2) = 0.27$). A comparison of Eqs.(2.10) and (2.13) for the experimental values before given is plotted in Fig.4.

Let us now discuss the dynamical equations of the system: we rewrite the DNLSE (2.6) in terms of the canonically conjugate population/phase variables, therefore enlightening its equivalence with the Josephson equations for a one dimensional junction array. With $\psi_j = \sqrt{n_j}e^{i\phi_j}$ we find

$$\begin{cases} \hbar\dot{n}_j = 2K\sqrt{n_j n_{j-1}}\sin(\phi_j - \phi_{j-1}) - 2K\sqrt{n_j n_{j+1}}\sin(\phi_{j+1} - \phi_j) \\ \hbar\dot{\phi}_j = -\Lambda n_j - \Omega j^2 + K\sqrt{n_{j-1}/n_j}\cos(\phi_j - \phi_{j-1}) + K\sqrt{n_{j+1}/n_j}\cos(\phi_{j+1} - \phi_j) \end{cases} \tag{2.14}$$

It is useful to introduce collective coordinates: the center of mass $\xi(t)$ and the dispersion $\sigma(t)$ are defined, respectively, as

$$\xi(t) = \sum_j j n_j \tag{2.15}$$

and

$$\sigma^2(t) = \sum_j j^2 n_j - \xi^2. \tag{2.16}$$

From Eq.(2.14) we have

$$\hbar\dot{\xi} = 2K \sum_j \sqrt{n_j n_{j+1}} \sin\left(\phi_{j+1} - \phi_j\right). \tag{2.17}$$

We can use for n_j the approximation (2.10) with the population density profile simply given by an inverted discrete parabolic profile, centered around ξ:

$$n_j(t) = \frac{\mu - \Omega[j - \xi(t)]^2}{\Lambda}$$

from which we can see that $\frac{d}{dt}\sigma^2 = 0$.

During the dynamical evolution, the relative phases across the junctions $\phi_{j+1} - \phi_j \equiv \Delta\phi(t)$ remain locked together to the same (oscillating) value. This has been verified studying the Fourier transform $\tilde{\psi}_k = \sum_j \psi_j e^{ikj}$, which remains well peaked around an oscillating value: for a study of the Fourier transforms in the dynamics see section 2.4. From the experimental point of view, the phase locking means that the expanded condensate continues to show the three peaks of the interferogram of Fig.1. The phase-current relation is given by

$$\begin{cases} \hbar\frac{d}{dt}\xi(t) = 2K\ \sin\Delta\phi(t) \\ \hbar\frac{d}{dt}\Delta\phi(t) = -\ m\omega_x^2\left(\frac{\lambda}{2}\right)^2\ \xi(t) \end{cases} \tag{2.18}$$

which, in analogy with the case of a superconducting Josephson junction (in the resistively shunted junction model [55,56]) and with the case of ^3He [59], is a pendulum equation with the relative phase $\Delta\phi$ corresponding to the angle to a vertical axis and the center of mass ξ being the corresponding angular momentum. We remark that, in the regimes we are considering, the current-phase dynamics does not depend explicitly on the interatomic interaction. This allows us to study regimes with a number of condensate atoms spanning over different order of magnitude. However, it is clear that the nonlinear interaction is crucial on determining the superfluid nature of the coupled condensates, by locking the overall phase coherence against perturbations.

In Fig.5 we show a comparison between the GPE and the DNLSE for the oscillations corresponding to two different initial displacements: there is a reasonable agreement. We also note that from the pendulum Eqs.(2.18) it is possible to say that the frequency of the oscillations should depend on the initial displacement $\xi(0)$. This is what happens: in Fig.6 we plot the frequency of the oscillations as a function of the initial displacement: the GPE results are compared with the DNLSE. We see that there is not an exact agreement and the frequency of the GPE is greater than the DNLSE, which is equal to frequency of the pendulum equations (2.18). For the critical initial displacement given in section 2.4 by Eq.(2.32), the oscillations are not anymore present: at that point the difference between GPE and DNLSE is of order 10 per cent. With experimental measurement with an error of less than 10 per cent and controlling the initial displacement with an error less than $5\mu m$, it should be possible to detect the shift of the frequency now discussed.

By defining the current as

$$I \equiv N_T \frac{d}{dt} \xi$$

and the critical Josephson current

$$I_c \equiv \frac{2 K N_T}{\hbar} \tag{2.19}$$

we readily see that Eqs.(2.18) are equivalent to the Josephson Eqs.(2.1)-(2.2). We note that the array of junctions behave as a single Josephson junction.

Furthermore, we can see that the small amplitude oscillation frequency ω_l of the current I gives a direct measurement of the critical Josephson current I_c and, therefore, of the atomic tunneling rate K of each condensate through the barriers. The critical current is related to the frequency ω of the atomic oscillations in the lattice and to the frequency ω_x of the condensate oscillations in absence of the periodic field by the relation

$$I_c = \frac{4\hbar N_T}{m\lambda^2} \left(\frac{\omega}{\omega_x}\right)^2 . \tag{2.20}$$

Fig.7 shows the experimental value of the frequencies of the small oscillations in the trap compared with the results of the Gross-Pitaevskii equation. The value of the frequency calculated using Eqs.(2.19), (2.20) and the variational estimate of K of App.B is also plotted.

2.3 Quantum phase transitions

In this section we briefly discuss the possibility to observe quantum phase transitions in arrays of weakly coupled BECs. The full quantum Hamiltonian for the bosonic gas in the optical potentials is

$$i\hbar\frac{\partial}{\partial t}\hat{\Psi}(\vec{r},t) = \left[T + V_{ext} + \int d\vec{r'}\hat{\Psi}^\dagger(\vec{r'},t)v(\vec{r}-\vec{r'})\hat{\Psi}(\vec{r'},t)\right]\hat{\Psi}(\vec{r},t) \tag{2.21}$$

where $T = -\hbar^2\vec{\nabla}^2/2m$ and $v(\vec{r}-\vec{r'})$ is the two-body potential. Here for simplicity, we does not consider the harmonic trap: $V_{ext}(\vec{r}) = V_0\cos^2(kx)$. By doing the standard s-wave scattering approximation ($v(\vec{r}-\vec{r'}) = g_0\delta(\vec{r}-\vec{r'})$) we obtain the well- known equation

$$i\hbar\frac{\partial}{\partial t}\hat{\Psi} = \left[T + V_{ext} + g_0\hat{\Psi}^\dagger\hat{\Psi}\right]\hat{\Psi} \tag{2.22}$$

from which the Gross-Pitaevskii is usually derived [32].

When the power laser is high enough, we can do a tight-binding approximation, exactly as in the Chapter 1:

$$\hat{\Psi}(\vec{r},t) = \sqrt{N_T}\sum_j \hat{\psi}_j(t)\Phi_j(\vec{r}) \tag{2.23}$$

In (2.23), $\Phi_j(\vec{r})$ is a wavefunction localized in the well n and normalized to 1. The Bose-Hubbard model (or quantum-DNLS) is then obtained:

$$\hat{H} = \sum_j [-K(\hat{\psi}_j\hat{\psi}^\dagger_{j+1} + \hat{\psi}^\dagger_j\hat{\psi}_{j+1}) + \frac{U}{2}(\hat{\psi}^\dagger_j\hat{\psi}_j)^2] \tag{2.24}$$

where the coefficients K and U are the same of the previous section. As it is well known, quantum phase transitions for one-dimensional systems are possible only at $T = 0$ [63]. The Bose-Hubbard model has been intensively investigated (for a discussion in one dimension see e.g [64] and reference therein), also in connection with the properties of arrays of Josephson junction arrays, which are usually described by the Quantum Phase Model, which is strongly related to Bose-Hubbard model. For a discussion of the Quantum Phase Model in one dimension see [23, 65–67].

To connect with the standard notation, we observe that the number of bosons in the site j is $\hat{N}_j = N_T\hat{\psi}^\dagger_j\hat{\psi}_j$. Using known results, we have that the ratio between the Josephson energy

$$E_j = \frac{K < N >}{N_T} \tag{2.25}$$

and the charging energy

$$E_c = \frac{U}{N_T^2} \tag{2.26}$$

determine the transition between the superfluid region and the Mott insulator (in which the phase is undetermined and the atom number states are squeezed). In Eq.(2.25), $< N >$ is the average value of particles per site.

When $E_j/E_c >> 1$, the effects of quantum fluctuations are negligible: this is precisely the case considered in the experiment described in the previous section, where E_j/E_c is of order 10^5. When E_j/E_c approaches to unity, the quantum fluctuations becomes more and more important: in [6] $E_j/E_c \sim 10 - 100$. The quantum phase transition occurs when

$$E_j \sim E_c.$$

Since E_j is proportional to K and K decreases when V_0 increases, we have to increase the laser power.

Here we give an estimate of the power of the laser needed to observe the quantum fluctuations and, possibly, the quantum phase transition. We calculate $K(V_0)$ by using the Eq.(2.20) and calculating the frequency of the small oscillations with the GPE (which is expected to work until the quantum fluctuations becomes important). From our results, plotted in Figs.8-9, we can see that the dependence of the microscopic quantum tunneling (and therefore of the Josephson energy) on the height of the barriers, V_0, is of the form

$$\frac{K}{E_R} = C_0 \, e^{-\Gamma V_0/E_R} : \tag{2.27}$$

this dependence is in agreement with the results in [68]. We numerically find $C_0 \approx 0.15$ and $\Gamma \approx 0.2$ (proceeding as in [68] we found a different value for Γ, which does not fit the experimental data).

Now we can estimate the value V_0^{cr} at which the transition occurs: this value of course depends on the number of particles in the lattice, as previously discussed. With $N_T \sim 10000$ and ≈ 100 sites, we get

$$V_0^{cr} \approx 45 - 50. \tag{2.28}$$

Reducing the number of particles, we get a critical value of the laser power more realistic value from the experimental point of view (but, of course, is also more difficult to deal with a so small number of particles): with $N_T \sim 1000$ and ≈ 50 sites we have

$$V_0^{cr} \approx 30 \, - \, 35. \tag{2.29}$$

2.4 Modulational instability: a classical superfluid-insulator transition

The Modulational Instability (MI) is a general feature of discrete as well as continuum nonlinear wave equations. Its demonstrations span a diverse set of disciplines ranging from fluid dynamics [69] (where it is usually referred to as the Benjamin-Feir instability) and nonlinear optics [70] to plasma physics [71].

MI refers to the exponential growth of a small perturbation of a carrier wave, as a result of the interplay between dispersion and nonlinearity. One of the early contexts in which its significance was appreciated was the linear stability analysis of deep water waves which are described by the ubiquitous model of the nonlinear Schrödinger equation. It was only much later recognized that the conditions for MI would be significantly modified for discrete settings relevant to the local denaturation of DNA [72] or arrays of optical fibers [46,51]. In the latter case, the relevant model is the DNLSE and its MI conditions were discussed in [73]. In fact, it was recently recognized that in discrete systems, MI is “the first step towards energy localization in nonlinear lattices” [74], since it leads to the creation of localized coherent structures which are subsequently trapped and pinned due to lattice discreteness [75].

In this section we want to discuss how to observe the MI in an array of weakly coupled BECs and to present some preliminary experimental data obtained by the LENS group at Firenze. We will refer to the experimental setup described in section 2.2, with the same values (the only differences is that in the experiments discussed below the total number of particles is 50000). As we have discussed, for a small displacement of the magnetic trap, coherent oscillations in the lattice are observed. The transmission of coherent matter waves in an array of weakly coupled condensates requires phase coherence among the sites [8].

However, there is a critical displacement above which the phase coherence is dramatically lost. The relative phase of the condensates localized in different sites randomizes (by running at different velocities), and the system becomes an insulator. It is worth stressing that such randomization takes place between the phases of BECs localized in different "sites", each BEC remaining internally coherent. The transmission of coherent matter waves in an array of weakly coupled condensates requires phase coherence among the sites.

In order to explain the occurrence of MI in the array, let us consider the DNLSE (2.6) with $\epsilon_n = 0$ (which corresponds to neglect the effect of the harmonic trap). We observe that among the eigenstates of Eq.(2.6) there are plane waves of the form $\psi = \psi_0 \exp(ikn)$, and the chemical potential is given by: $\mu = -\cos k + \Lambda \mid \psi_0 \mid^2$. The stability analysis of such states can be carried out by writing: $\psi_n = \psi_0 e^{ikn}(1 + ue^{iqn} + v^* e^{-iqn})$. The DNLSE excitation spectrum (for $\epsilon_n = 0$) is given by:

$$\omega_{n,\pm} = \sin k \sin q \pm 2\sqrt{\cos^2 k \cdot \sin^4 \frac{q}{2} + \Lambda|\psi_0|^2 \cos k \cdot \sin^2 \frac{q}{2}} \tag{2.30}$$

The MI occurs when the eigenfrequency ω_n becomes imaginary: we see that when $\cos k > 0$, $\cos^2 k \cdot \sin^4 \frac{q}{2} + \Lambda|\psi_0|^2 \cos k \cdot \sin^2 \frac{q}{2} > 0$, and ω_n is always real. Instead, for $\cos k < 0$, we see that $\cos^2 k \cdot \sin^4 \frac{q}{2} + \Lambda|\psi_0|^2 \cos k \cdot \sin^2 \frac{q}{2} < 0$ if

$$\Lambda \mid \psi_0 \mid^2 > -\cos k \cdot \sin^2 \frac{q}{2} \tag{2.31}$$

Therefore, when $\Lambda > 0$, the system would become unstable leading to exponential growth of all phonon $q-$modes when the quasi-momentum k of the carrier wave is such that $k > \pi/2$. This result still hold for non-homogeneous carrier waves, when the wave-packet has a width much larger than the wave length associated with the collective motion. This conclusion can be further exploited by studying the stability of the collective coordinate equations of motion [13].

The effect of the exponential growth of phonon modes of arbitrary momenta, leads to an effective dephasing among different sites, and the wave suddenly stops. The complete delocalization in momentum space leads to strong localization in real space, hence the appearance of localized pulse-like coherent structures of large amplitude. However, it is well-known that discreteness, due to the presence of the so-called Peierls-Nabarro barrier [75], pins such large amplitude solutions [74, 76], not allowing them to propagate. The excess of kinetic energy is partially converted to wakes of small amplitude extended wave radiation [75] and partially stored to the internal mode breathing oscillations [77] of the resulting pulses.

By considering also the external potential $\epsilon_n = \Omega n^2$, the previous conclusions are essentially unchanged. By using the Eqs.(2.18), we see that the MI instability occurs when the initial displacement $\xi(0)$ is such that in the pendulum oscillations $\Delta\phi$ reach $\pi/2$. The critical value for the initial displacement, $\xi_{cr}(0)$, is given by the formula

$$\xi_{cr}^2(0) = \frac{16K}{m\omega_x^2\lambda^2} = \frac{2K}{\Omega} \tag{2.32}$$

where Eq.(2.20) was also used. From this equation we can see that for laser power V_0 increasing, the critical value $\xi_{cr}(0)$ decreases and the region of the MI increases. In Fig.10 we plot the critical displacement vs. the laser power V_0, as given by Eq.(2.32).

The average value momentum $< k >$ is calculated from the Fourier transform $\tilde{\psi}_k$ of the wavefuction ψ_n: it is

$$< k >= \sum_k k \mid \tilde{\psi}_k \mid^2 \tag{2.33}$$

(in this equation $\tilde{\psi}_k$ is normalized to 1: $\sum_k \mid \tilde{\psi}_k \mid^2 = 1$). As discussed in section 2.2, it is in

$$< k >= \Delta\phi. \tag{2.34}$$

In Fig.11 we show that for a small initial displacement $\xi(0) < \xi_{cr}(0), < k(t) >$ oscillates with time as the pendulum Eqs.(2.18) predicts. When $\Delta\phi$ reaches $\pi/2$, the MI is activated and the Fourier transform, as well as the wave function, breaks down.

As a consequence of the instability, the on site phases randomize. This can be shown by defining an "order parameter"

$$\Psi = \sum_n \psi_{n+1}\psi_n^*. \tag{2.35}$$

In Fig.12 we show that $| \Psi |^2$ is 1 for $\xi(0) < \xi_{cr}(0)$. When $\Delta\phi \rightarrow \pi/2$, the order parameters drops suddenly to zero, due to a loss of coherence among interwell phases. In this sense we can say that we are dealing with a classical superfluid-insulator transition. In Fig.13 the center of mass motion is plotted in the MI region: a comparison between GPE and DNLSE is done and a reasonable agreement is found.

The decoherence, localization and pinning are in agreement with the experimental as well as with the model (with both GPE and DNLSE) observations and clearly indicate the importance of MI in inducing energy localization in this effectively discrete nonlinear system. As we discussed, for small displacements the system can oscillate coherently by locking the relative phases to the same value $\Delta\phi(t) = p(t)$, where $p =< k >$ is the quasi-momentum of the wave-packet. However, MI "unlocks" the relative phases, which start to run independently with different velocities. The overall phase coherence is quickly lost, and the system behaves as an insulator. Such a transition occurs for classical field theories and it is qualitatively different from the quantum Mott insulator-superfluid (QMIS) transition in mesoscopic Josephson junction chains, which is driven by the competition between zero-point quantum phase fluctuations and the potential energy. Yet, it is possible to draw an analogy. In the former (MI) case, the insulator regime is associated with a vanishing temporal correlation among the phases of each site, each phase still being meaningful in the GPE sense. The quantum transition, on the other hand, is driven by the large quantum phase fluctuations induced by the squeezing of atom number states in each site, and, therefore, by the non-commuting nature of the number-phase observables. Clearly, such quantum fluctuations cannot be captured within the GPE framework.

In Fig.14 we report preliminary experimental results of the LENS group which shows that the condensate stops for initial large displacement, and this is accompanied by a loss of coherence: the three peaks disappear, as we can see in the inset.

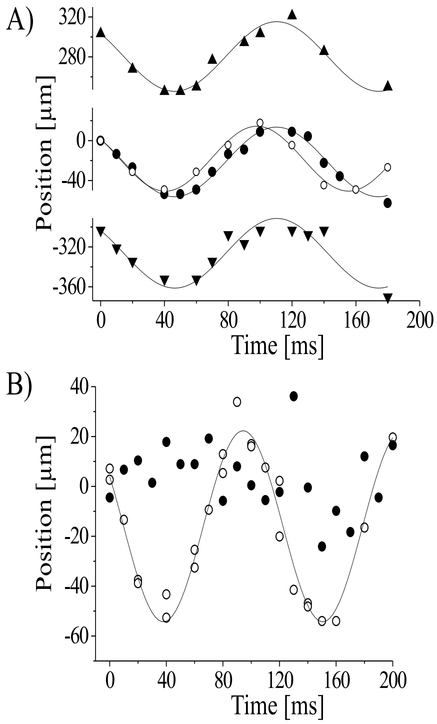

Figure 2.3: A) Center of mass position of the three peaks in the interferogram of the expanded condensate as a function of the time spent in the combined trap after displacement of the magnetic field. Up and down triangles correspond to the first order peaks, filled circles to the central peak. Open circles show the center of mass position of the BEC in absence of the optical lattice. The continuous lines are the fits to the data. B) Center of mass positions of the thermal cloud as a function of time spent in the displaced magnetic trap with the standing wave turned on (filled circles) and off (open circles).

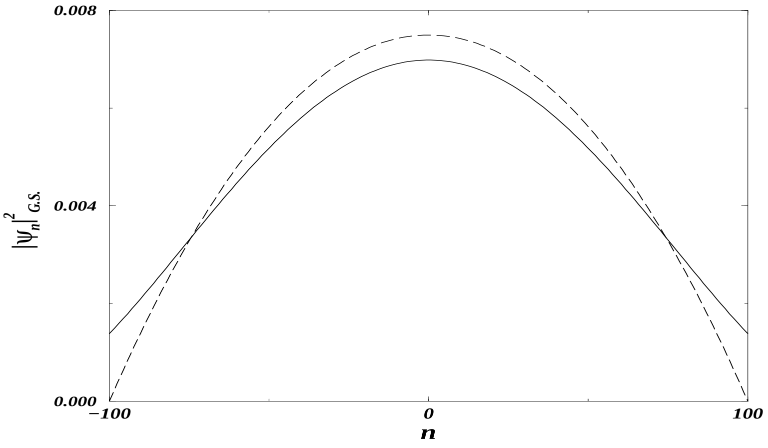

Figure 2.4: Comparison of the Eqs.(2.10), dashed line, and (2.13), solid, for $\alpha = 4$ and $N_T = 200000$.

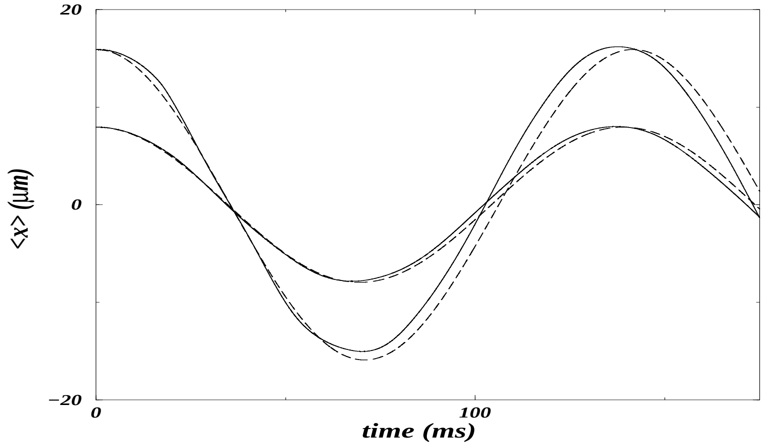

Figure 2.5: Comparison of the Gross-Pitaevskii equation (solid line) and the discrete nonlinear discrete Schrödinger equation (dashed) for two different initial displacements (20 and 40 sites). $V_0 = 4E_R$ and $N_T = 200000$ are used.

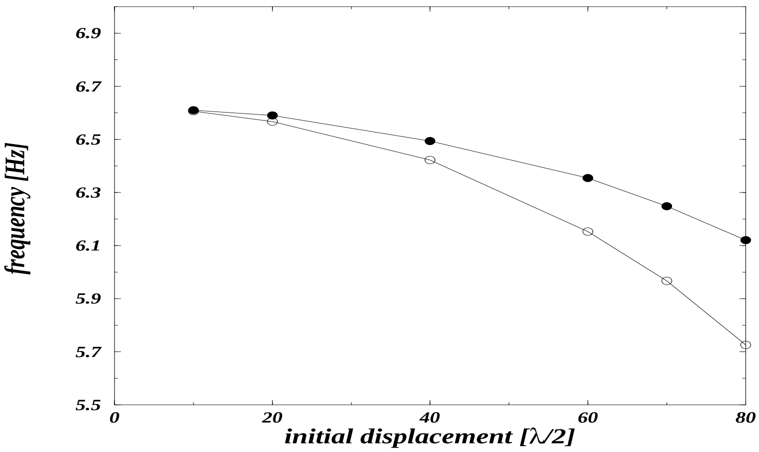

Figure 2.6: Frequency of the oscillations vs. initial displacement (expressed in lattice sites) with the Gross-Pitaevskii equation (black circles) and the discrete nonlinear discrete Schrödinger equation (open circles). $V_0 = 5E_R$ and $N_T = 50000$ are used.

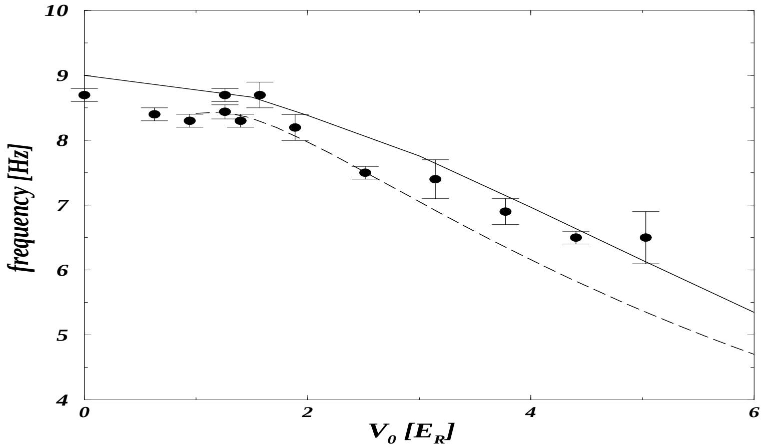

Figure 2.7: Frequency of the atomic oscillations in the trap as a function of the laser barrier height. Black circles: experimental data; solid line: solution of the GPE; dashed line: frequency obtained using Eq.(2.20) with K given by the variational calculation in App.B.

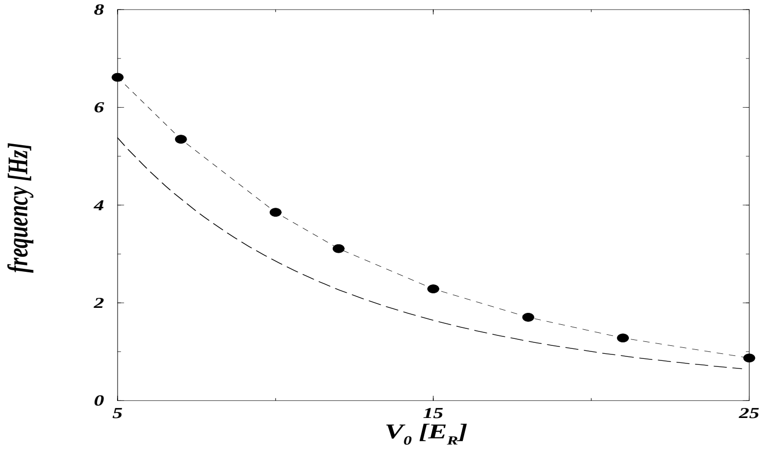

Figure 2.8: Plot of the frequency of the small oscillations as a function of the height of the energy barriers between adjacent wells V_0: black circles correspond to the solution of the GPE (2.3) and the long-dashed line to the variational estimate given in App.B.

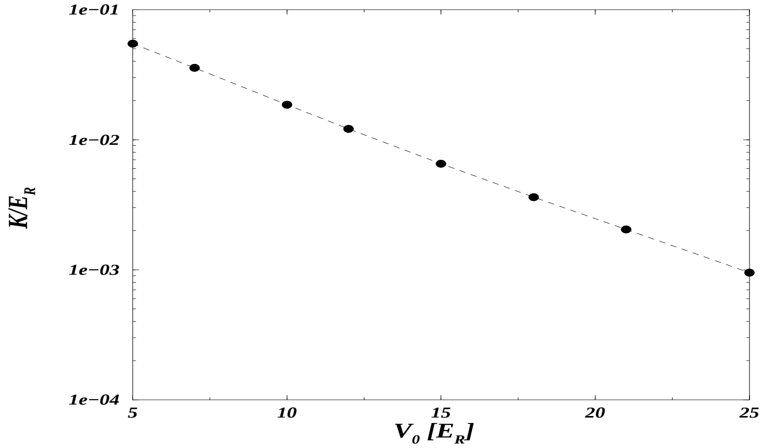

Figure 2.9: Plot in logarithmic scale of the microscopic tunneling rate K (in units of E_R) as a function of the height of the energy barriers between adjacent wells V_0: K is obtained by using the Eq.(2.20) and the frequencies of the small oscillations given by the solution of the GPE.

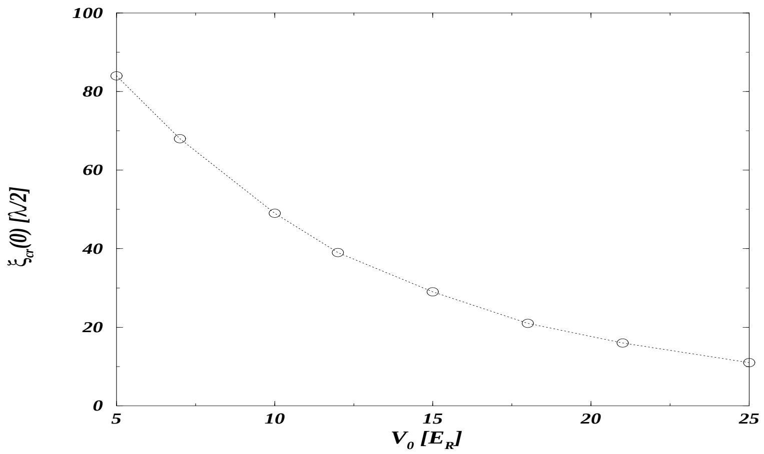

Figure 2.10: Plot of the initial critical displacement $\xi_{cr}(0)$ vs. the laser power V_0, as given by Eq.(2.32).

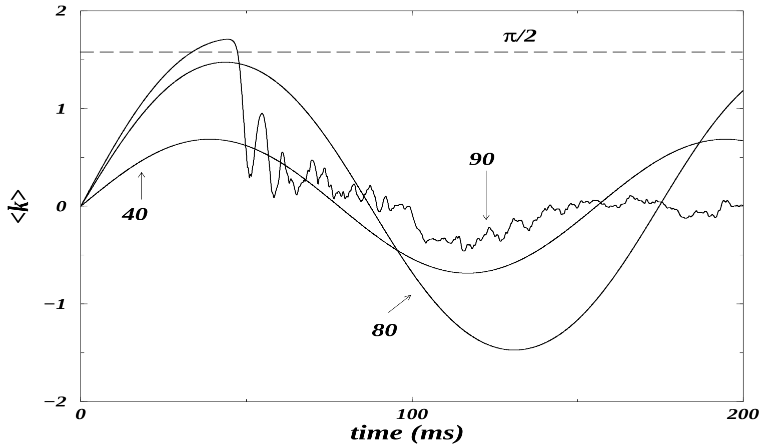

Figure 2.11: Plot of the quasi-momentum $< k >$ vs. time for three different initial displacements: 40, 80 and 90 sites. We are considering the values $V_0 = 5E_R$ and $N_T = 50000$: the Eq.(2.32) gives an initial critical displacement $\xi_{cr}(0) \approx 84$ sites. It is clearly seen that when $< k >$ reaches $\pi/2$ (i.e. with an initial displacement greater than $\xi_{cr}(0)$), the MI is activated.

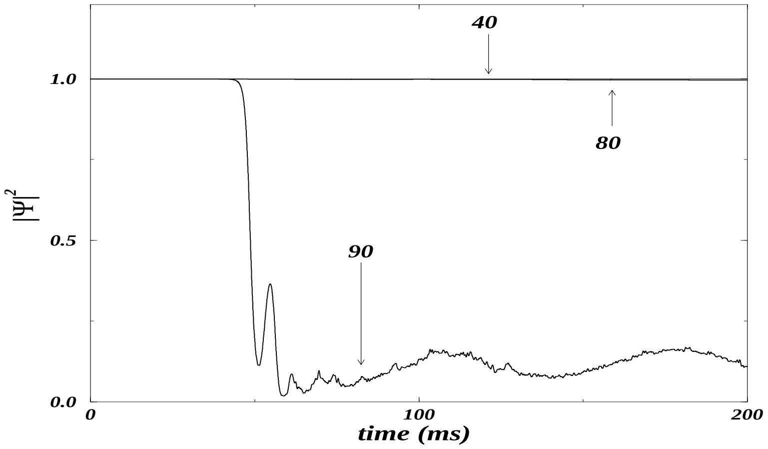

Figure 2.12: Plot of the modulus square of the order parameter Ψ defined by Eq.(2.35) for three different initial displacements (40, 80 and 90 sites) and with the same parameters of Fig.11. In the instant in which the quasi-momentum $< k >$ reaches $\pi/2$ (i.e. with an initial displacement greater than $\xi_{cr}(0)$), the order parameter drops to 0: see Fig.11.

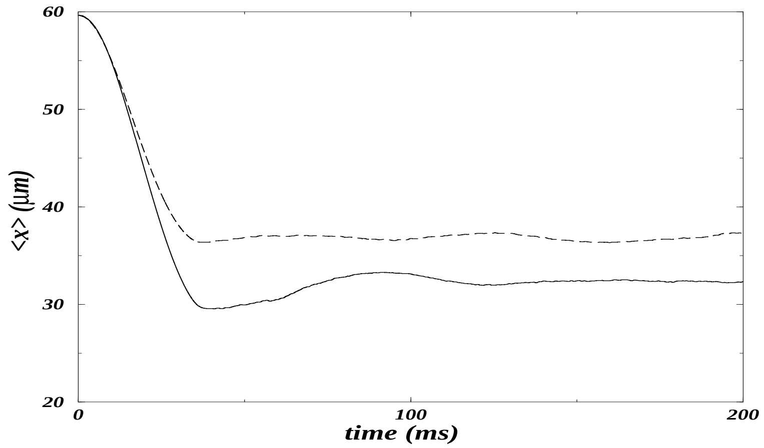

Figure 2.13: Center of mass vs. time for an initial displacement of 150 sites, greater than the critical displacement. We are considering the values $V_0 = 5E_R$ and $N_T = 50000$. Solid line: GPE; dashed line: DNLSE.

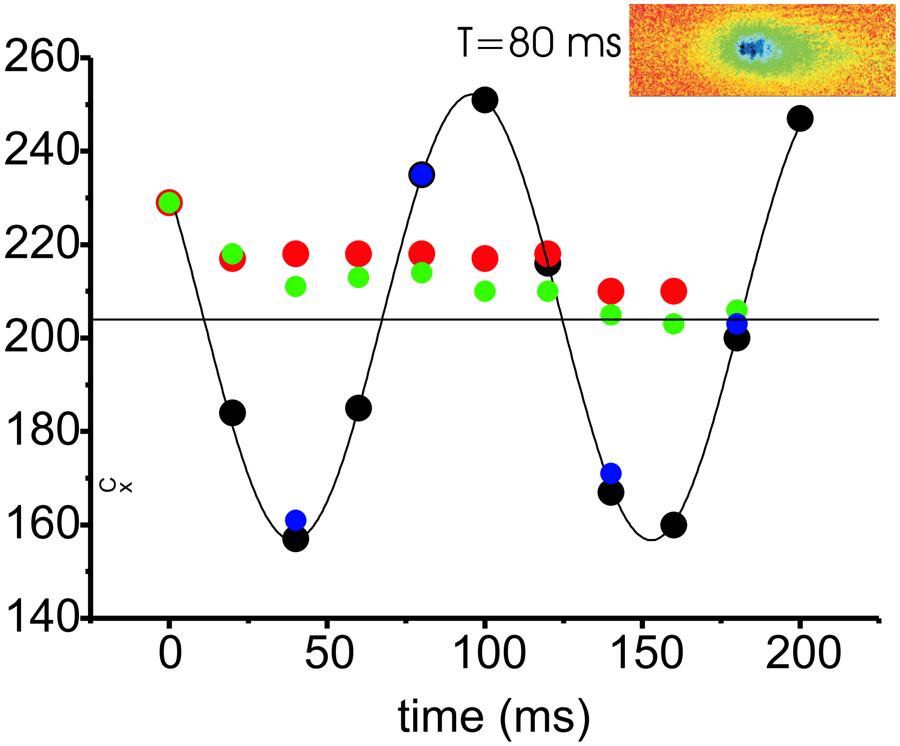

Figure 2.14: Preliminary experimental results of the LENS group on the occurrence of MI in arrays of weakly coupled BECs. Blue and black points: oscillations of the center of mass after the expansion ($t = 26.5ms$) without optical lattice (only harmonic trap); green points: the optical lattice is turned on with $V_0 = 3E_R$; red points: $V_0 = 5E_R$. The number of particles is $N_T = 50000$ and the center of mass is in arbitrary units.

Chapter 3

Superfluidity versus disorder

3.1 Introduction

In Chapters 1 and 2 we studied the properties of a BEC in a deep optical lattice, showing that the dynamics is governed by a discrete nonlinear Schrödinger equation. We also remarked that the possibility to have a physical system modeled by a such widely studied equation is one important reason of interest of the study of arrays of BECs. Yet, the inclusion of (possibly random) defects in the system BEC + periodic potential would allow to investigate the interplay between nonlinearity (provided by the interatomic potential), discreteness (given by the optical lattice) and disorder (e.g. the random potentials added to laser beams). The study of a such interplay has become one of the fundamental issues of the last decades in the study of many physical and biological systems (both discrete and continuous) [39].

It is well known that nonlinearity *or* disorder may lead to localized excitations - "solitonic" structures [78] and "Anderson localization" [53], respectively. The natural questions that arise are what happens when both nonlinearity *and* disorder are present and how the transport properties are affected. This problem is of central experimental relevance, since impurities can be reduced but never completely eliminated. In particular, it can be asked if random defects will (and, if so, how) destroy the propagation of traveling plane waves or localized excitations (allowed by the nonlinearity), and what are the conditions for crossing from a “superfluid” regime with propagation (and coherence) preserved (due to, for instance, a large nonlinearity), to a ”normal” regime with disorder induced damping.

In this chapter we consider the dynamical properties of DNLSE in an annular geometry and in the presence of impurities. Apart from the already mentioned fact that a BEC in an optical lattice map on a DNLSE, there are also other reasons which motivate such analysis: 1) the DNLSE is a general equation [16] which has all the required ingredients: nonlinearity, disorder and discreteness; 2) the continuum nonlinear Schrödinger equation (CNLSE) limit is exactly integrable; 3) other real physical systems, like optical fibers, map onto the DNLSE and also provide the ideal framework to investigate experimentally the competition between superfluidity and disorder in discrete systems. The annular geometry is paradigmatic for studying superfluid properties [54], and allows a clear comparison between the discrete and continuous limits.

With regard to optical fibers, a typical experimental setup is realized with an array of one dimensional nonlinear coupled waveguides [51]. As the light propagates along the array, the coupling induces an exchange of power among the single waveguides. In the low power limit (i.e. when the nonlinearity is negligible), the optical field spreads over the whole array. Upon increasing the power, the output field narrows until it is localized in a few waveguides, and discrete solitons can finally be observed [51, 79]. The evolution of $E_n(\tau)$, the electrical field in the nth waveguide, as a function of the position, τ, is governed by the DNLSE Eq.(3.1). In this case Λ is proportional to the Kerr nonlinearity and the on-site potentials ϵ_n are the effective refraction indices of the individual waveguides. In [80] a linearly growing index was considered, which allowed the observation of Bloch oscillations.

In this chapter we show that a traveling plane wave with initial wave vector k splits, in momentum space, into two waves with $\pm k$. The DNLSE dynamics with a single defect can be mapped onto an effective non-rigid pendulum Hamiltonian. The different predicted (and numerically confirmed) regimes include large amplitude pendulum oscillations, corresponding to the complete reflection and refocusing of the initial wave due to the impurity, fixed points given by solitonic structures, and self-trapped (or superfluid) states due to the pendulum rotations (section 3.2). With two impurities on the lattice in the dynamics enters not the spatial distance between the defects, but the relative phase between them and the creation of barriers transparent to incident waves is made possible. These (and additional) regimes are also present given an arbitrary (including random) distribution of defects, the dynamics still being governed by a non-rigid pendulum Hamiltonian with parameters depending on the distribution of defects (sections 3.3 and 3.4 and also [21]).

3.2 The discrete nonlinear Schrödinger equation with a single impurity

The DNLSE with defects ϵ_n is (in the dimensionless form used in the previous chapters):

$$i\frac{\partial \psi_n}{\partial \tau} = -\frac{1}{2}(\psi_{n-1} + \psi_{n+1}) + (\epsilon_n + \Lambda \mid \psi_n \mid^2)\psi_n, \tag{3.1}$$

where Λ is the nonlinear coefficient and $n = 1, \cdots, N$ (N number of sites). These defects can be spatially localized or extended; for instance, the impurities in optical fibers can be induced by different (possibly random) effective refraction indices of the guides or with varying spatial separations between them. In BEC's trapped in optical lattices, the defects can be created with additional lasers and/or magnetic fields; the presence of a thermal component can also be phenomenologically modeled, in some limits, by a random distribution of defects.

First, we consider the DNLSE with a single defect

$$\epsilon_n = \epsilon\, \delta_{n,\bar{n}} \tag{3.2}$$

at the site $\bar{n}$, and we study the propagation of a plane wave $\psi_n(\tau = 0) = e^{ikn}$. In the following we assume $\Lambda > 0$ (which corresponds to a repulsive interatomic interaction in BEC's, as is the case for ^{87}Rb atoms). Note, however, that Eq.(3.1) is invariant with respect to the transformation $\Lambda \to -\Lambda$, $\epsilon_n \to -\epsilon_n$, $\tau \to -\tau$ and $\psi_n \to \psi_n e^{i\pi n}$. Since we consider periodic boundary conditions (due to the annular geometry), we have $k = 2\pi l/N$ with l integer ($l = 0, \cdots, N-1$).

In the CNLSE (translationally invariant) limit of the DNLSE, a well know argument suggested by Landau implies that the finite nonlinearity allows a superfluid regime when the traveling speed is smaller than the sound velocity (for weak perturbations). The key point of this argument is that the nonlinearity provides an energy barrier for the creation of elementary excitations which would dissipate the energy of the incident wave [54].

This scenario is completely changed by the discreteness. First, as we discussed in Chapter 2, when $\cos k < 0$ the system becomes modulationally unstable [73]. Stability analysis reveals that the eigenfrequencies of the linear modes become imaginary driving an exponential growth of small perturbations. This modulation instability disappears, for $\Lambda > 0$, in the CNLSE limit.

Let us consider, then, the case in which $\cos k > 0$. We anticipate that when $\Lambda = 0$ and the strength of the impurity is not too strong (i.e. not greater than the hopping term, which is 1 in our units), the wave is always reflected by the defect, and the angular momentum, defined as

$$L(\tau) = i \sum_n (\psi_n \psi_{n+1}^* - c.c), \tag{3.3}$$

oscillates between the initial value L_0 and $-L_0$. What is very different from the continuum case is that only plane waves with wave vector $\pm k$ play a role, while the excitation of the other modes is inhibited by higher energy barriers. The occurrence of such barriers in the discrete case will be explained in the following. In Fig.1 we plot (in log-log scale) the frequency of the oscillations of the angular momentum; the dashed line is the result of the-mode model (3.5) in which only the plane waves $\pm k$ enter on the dynamics. As we will show below, when $\Lambda = 0$, the oscillation of L are sinusoidal and their frequency is given by

$$\nu = \frac{\epsilon}{\pi N}. \tag{3.4}$$

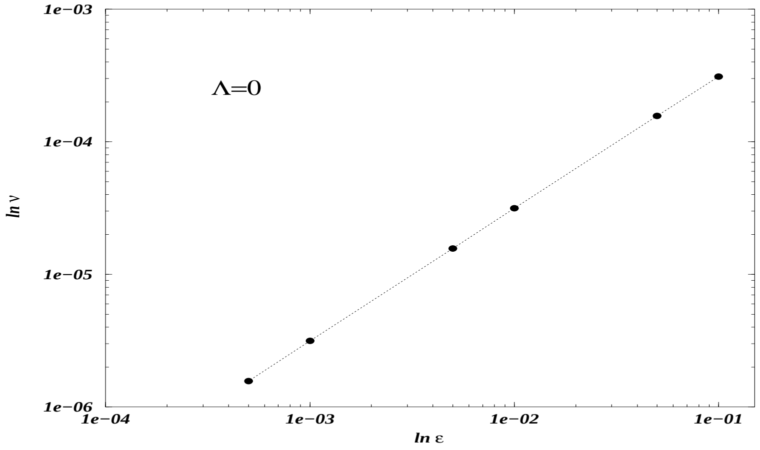

Figure 3.1: Numerical (black circles) and analytical (dashed line) frequency of the oscillations of the angular momentum as a function of the strength ϵ of the impurity without nonlinearity. A log-log scale is used. Numerical parameters of the simulations: $N = 100$, $l = 10$. The numerical analysis shows that there is not dependence of ν on the momentum $k = 2\pi l/N$.

The argument for which only the modes $\pm k$ plays a role can be extended to the case of a finite nonlinearity, $\Lambda \neq 0$. In Fig.2 we plot, as an example, the angular momentum L (normalized to the initial value L_0) for a finite value of Λ. The plot of the Fourier transforms of ψ_n at four different times is in Fig.3: it shows that the most part of the Fourier transform is peaked around $\pm k$.

Therefore we introduce a two-mode ansatz for the dynamical evolution of the wave function:

$$\psi_n(\tau) = A(\tau)e^{ikn} + B(\tau)e^{-ikn}. \tag{3.5}$$

We put $A, B = \sqrt{n_{A,B}(\tau)}e^{i\phi_{A,B}(\tau)}$, $z = n_A - n_B$ and $\phi = \phi_A - \phi_B$. We will compare the numerical solution of (3.1) with the analytical solution of (3.10) obtained from the ansatz (3.5).

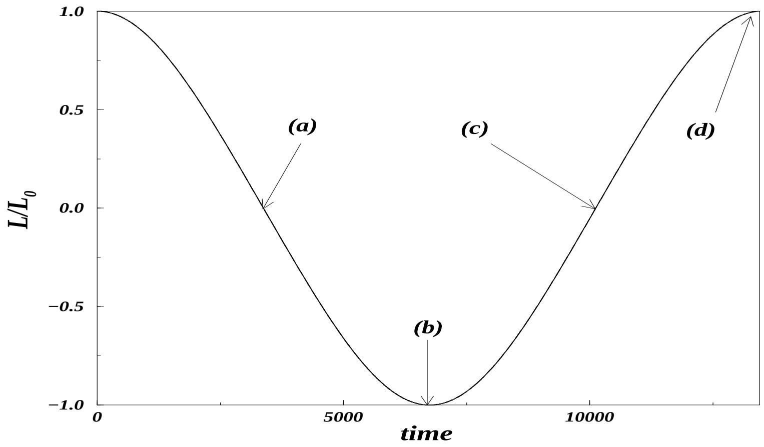

Figure 3.2: Numerical (solid line) and analytical (dashed) angular momentum, normalized to the initial value L_0, vs. time. Numerical parameters of the simulations: $\epsilon = 0.01$, $N = 40$, $l = 4$, $\Lambda/\Lambda_c = 0.5$, where $\Lambda_c = 4\epsilon/N$. The Fourier transform at points $(a), \cdots, (d)$ is reported in Fig.3.

Let us, for the moment, discuss the validity of (3.5). With an impurity smaller than the hopping term, $\epsilon << 1$, the momentum distributions, peaked around $\pm k$, do not overlap. This condition preserves the two-mode dynamics through all the time scales we have been able to explore numerically. The situation changes in the (quasi-)continuum limit. In this case phonons can be emitted only with quasi-momentum close to k, a condition which allows the applications of the Landau superfluidity criteria. The crossover between continuum and discrete limit is a very interesting one, and deserves further investigations. Here we stress, and we will show it explicitly below at the end of the present section, that the pendulum (two-mode) dynamics is crucially related to discreteness and nonlinearity, and disappears in the continuum limit. Yet, there is a striking analogy: in both cases (in the Landau and in the "pendulum" criteria) the phonon emission out of the incident wave

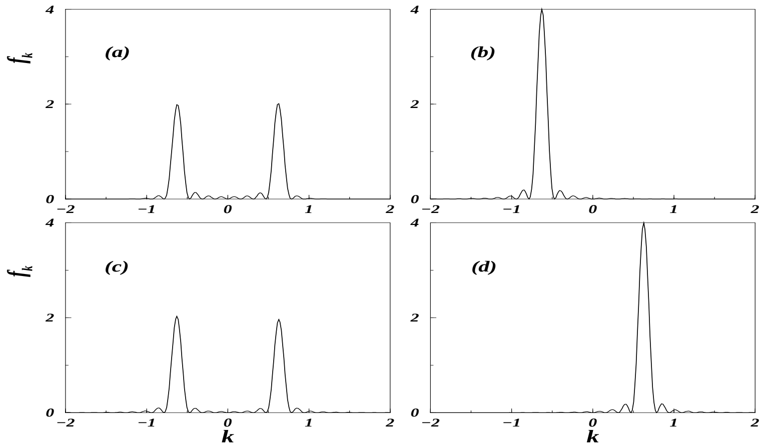

Figure 3.3: Fourier transform f_k of ψ_n at times marked respectively as $(a), \cdots, (d)$ in Fig.2.

(which, therefore, dissipates its energy) can be inhibited by an effective energy barrier. The key difference lies on the corresponding spectrum of the emitted phonons, which leads to a completely different dynamics.

A further important point is that the two mode ansatz (3.5) remains valid even with a time-dependent, extended or random distribution of defects, so long as the sum of the impurity strengths remains small compared to unity (in our dimensionless units). These situations will be discussed in this chapter. Furthermore, when the initial wave function is given by the sum of more waves $\psi_n(0) = \sum_j A_j e^{ik_j n}$ the ansatz (3.5) can be straightforwardly generalized so long as the quasi-momentum distributions peaked around k_j do not overlap. The collision of a soliton with a single impurity has been studied, from a different perspective, in [44]. A numerical analysis of the propagation of plane waves across a segment with defects was done in [81].

Let us now come back to the derivation of the equations of motion for a single defect. We can define an effective Lagrangian as

$$\mathcal{L} = \sum_n i\dot{\psi}_n \psi_n^* - \mathcal{H}, \tag{3.6}$$

where

$$\mathcal{H} = \sum_n [-\frac{1}{2}(\psi_n \psi_{n+1}^* + \psi_n^* \psi_{n+1}) + \epsilon_n \mid \psi_n \mid^2 + \frac{\Lambda}{2} \mid \psi_n \mid^4] \tag{3.7}$$

(both the Hamiltonian $\mathcal{H}$ and the norm $\sum_n \mid \psi_n \mid^2 = N$ are conserved). Substituting the ansatz (3.5) in (3.6), we find

$$\mathcal{L} = -Nn_A\dot{\phi}_A - Nn_B\dot{\phi}_B - \Lambda n_A n_B - \frac{2\epsilon}{N}\sqrt{n_A n_B}\cos(\phi_A - \phi_B + 2k\bar{n}) \tag{3.8}$$

where we used the relation

$$\sum_n e^{2ikn} = 0. \tag{3.9}$$

From (3.8), the Euler-Lagrange equations $\frac{d}{dt}\frac{\partial \mathcal{L}}{\partial \dot{q}_i} = \frac{\partial \mathcal{L}}{\partial q_i}$ for the variational parameters $q_i(\tau) = n_{A,B}, \phi_{A,B}$ give:

$$\begin{cases} \dot{z} = -\frac{2\epsilon}{N}\sqrt{1-z^2}\sin\phi \\ \dot{\phi} = \frac{2\epsilon}{N}\frac{z}{\sqrt{1-z^2}}\cos\phi + \Lambda z, \end{cases} \tag{3.10}$$

with the replacement $\phi + 2k\bar{n} \rightarrow \phi$. The total (conserved) energy is:

$$H = \frac{\Lambda z^2}{2} - \frac{2\epsilon}{N}\sqrt{1-z^2}\cos\phi \tag{3.11}$$

and the equations of motion (3.10) can be written in the Hamiltonian form $\dot{z} = -\frac{\partial H}{\partial \phi}$ and $\dot{\phi} = \frac{\partial H}{\partial z}$ with z and ϕ canonically conjugate variables. We observe that when $\Lambda = 0$, the Eqs.(3.10) give

$$\ddot{z} = -\left(\frac{2\epsilon}{N}\right)^2 z, \tag{3.12}$$

from which Eq.(3.4) is readily found.

The Eqs.(3.10) have been studied in very different contexts, including the polaron dynamics, where the dimer Eq.s(3.10) had been solved analytically [82], and in the Josephson dynamics of two weakly coupled Bose-Einstein condensates [35]. Eqs.(3.10) are those of a nonrigid pendulum: ϕ is the angular position and z its conjugate momentum. The non-rigidity of the pendulum is due to its momentum dependent length. The study of a non-rigid pendulum enriched by internal modes will be presented in Chapter 4.

The pendulum phase portrait, z-ϕ, has been studied in detail in [36]. Let us briefly recall the main results. We have a) oscillations around $<\phi>=0$ and $<z>=0$ (0-*states*); b) oscillations around $<z>\neq 0$ with running phase $<\phi>\propto t$ (*self-trapped states*); c) oscillations around $<z>=0$ and $<\phi>=\pi$ (π-*states*); d) oscillations about $<z>\neq 0$ and $<\phi>=\pi$ (*self-trapped* π-*states*). The $<\ldots.>$ stand for a time average.

To understand the meaning of these regimes in our system, we observe that the angular momentum is proportional to z. Using the ansatz (3.5) in (3.3) we get

$$L = 2Nz\sin k \tag{3.13}$$

or, expressing the momentum in units of its initial value L_0:

$$\frac{L}{L_0} = z. \tag{3.14}$$

Therefore $<z>=0$ implies that the wave is completely reflected, and $<z(\tau)>>0$ (or $<z(\tau)><0$) that the wave is only partially reflected by the impurity. The latter regime is given by a complete rotation of the pendulum about its center, and can be considered as a self-trapping of the angular momentum. Equivalently, there is an effective energy barrier which forbids the complete reflection of the incident wave, and preserve its coherence. The observation of a persistent current is associated to a superfluid regime of the DNLSE equation.

We can derive the critical value for the occurrence of the transition between the regimes with $< z >= 0$ (reflection of the wave) and the regimes with $< z > \neq 0$ in the following way. Let us consider initial values $z(0) = 1$ and $\phi(0) = 0$: the (conserved) initial energy is $H_0 = \frac{\Lambda}{2}$. We want to find the condition for which z cannot reach the value 0. Since $H(z = 0) = -(2\epsilon/N)\cos\phi \leq 2\epsilon/N$, we find a critical value for the pendulum oscillations about its center given by

$$\Lambda_c = \frac{4\epsilon}{N} : \tag{3.15}$$

when $\Lambda < \Lambda_c$, z oscillates around 0. When $\Lambda = \Lambda_c$, asymptotically $z(\tau) \to 0$ and with $\Lambda > \Lambda_c$, $< z(\tau) > \neq 0$. In Fig.4 we plot the normalized angular momentum $L(\tau)/L_0$ vs. time for different Λ/Λ_c in order to illustrate the transition. In Fig.5 we plot the time average value of the normalized angular momentum for different values of Λ/Λ_c and $z(0) = 1$, $\phi(0) = 0$. The numerical solutions of Eq.(3.1) are in agreement with the two-mode approximation (3.10), dashed line. For $\Lambda < \Lambda_c$ there is, on average, no transport in the lattice.

For arbitrary initial conditions, the critical value of Λ is given by

$$H(\phi(0), z(0) = 2\epsilon/N \tag{3.16}$$

As a further difference from the Landau criteria, we remark that the critical value for self-trapping (and superfluidity) in the case of a single impurity does depend on the strength of the defect, but not on the quasi momentum k.

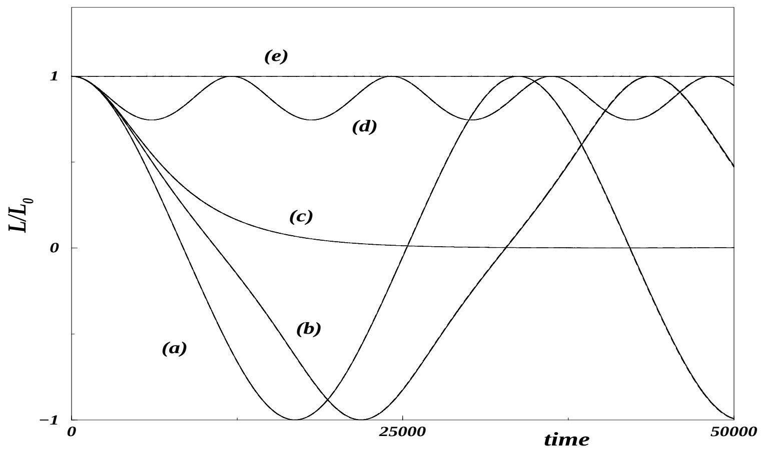

Figure 3.4: Normalized angular momentum $L(\tau)/L_0$ vs. time for different values of $\Lambda/\Lambda_c = 0.5, 0.75, 1, 1.5, 25$ respectively corresponding to $(a), \cdots, (e)$ ($\Lambda_c = 4\epsilon/N$). Numerical parameters in the simulation: $\epsilon = 0.01$, $N = 100$, $z(0) = 1$, $\phi(0) = 0$.

Let us now study the fixed points of Eqs.(3.10) and the related physical regimes. By solving for $\dot{z} = 0$, $\dot{\phi} = 0$, we find first

$$\begin{cases} z = 0 \\ \phi = 2m\pi \end{cases} \tag{3.17}$$

with $\mid A \mid = \mid B \mid$ (m is an integer). It corresponds to a time-independent solution $\psi_n \propto \cos(kn)$ and to a minimum of the energy (3.11). The fixed point (3.17) is stable and the oscillations about it are the 0-states: the small-amplitude oscillations have frequency $\propto \sqrt{1 + \Lambda}$. In Fig.6 we show the large amplitude oscillations, comparing numerical and analytical solutions: we fix Λ and $\phi(0) = 0$ and we vary the initial imbalance $z(0)$. By using the same argument as before, when $z(0)$ is smaller than a critical value $z_{cr}(0)$ we have $< z(0) >= 0$. By approaching to $z_{cr}(0)$ the oscillations become more and more anharmonic, and they goes to 0 asymptotically for $z_{cr}(0)$. For $z(0) >$

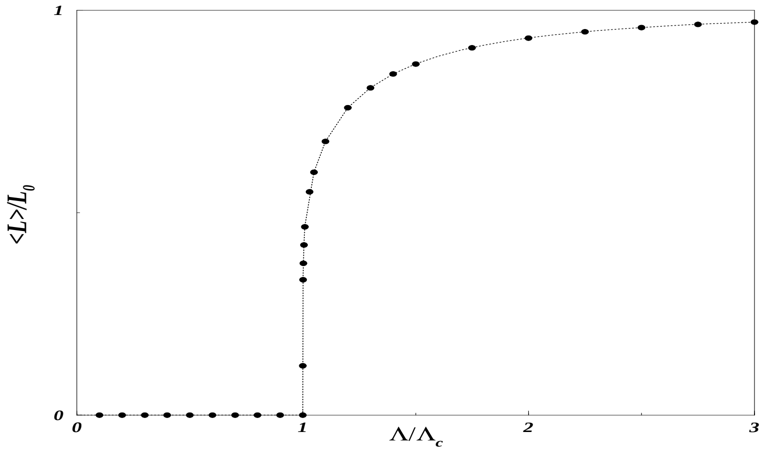

Figure 3.5: Average value of the normalized angular momentum vs. the nonlinear coefficient Λ/Λ_c. The filled circle are the numerical solutions of Eq.(3.1), the dashed line is obtained from equations (3.10). Numerical parameters as in Fig.4.

$z_{cr}(0)$ the self-trapped regime is retrieved. By using Eq.(3.16), it is found

$$z_{cr}^2(0) = \frac{2\frac{\Lambda}{4\epsilon/N} - 1}{\left(\frac{\Lambda}{4\epsilon/N}\right)^2} \tag{3.18}$$

The other fixed points of Eqs.(3.10) are

$$\begin{cases} z = 0 \\ \phi = (2m+1)\pi \end{cases} \tag{3.19}$$

and

$$\begin{cases} z = \pm\sqrt{1 - \frac{2\epsilon/N}{\Lambda}} \\ \phi = (2m+1)\pi \end{cases} \tag{3.20}$$

The fixed point (3.19) correspond to a time-independent solution of Eq.(3.1) of the form $\psi_n \propto \sin(kn)$ and the oscillations around him are the π-states previously introduced. The oscillation around (3.20) are the self-trapped π-states, in which the nonrigid pendulum does complete oscillations on its top.

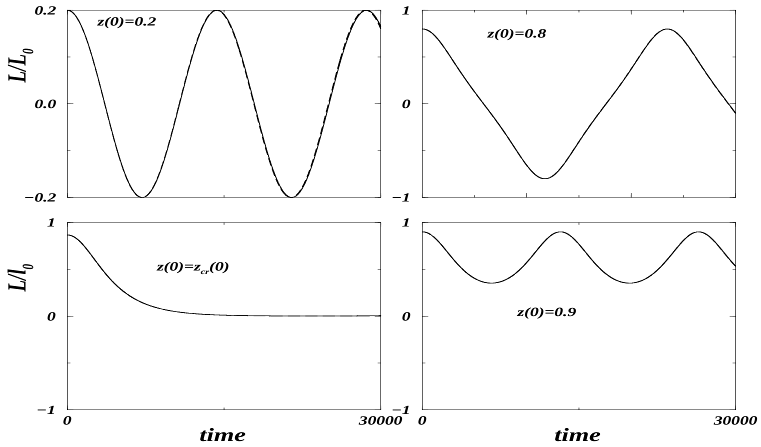

Figure 3.6: Normalized angular momentum as a function of time for $\Lambda = 8\epsilon/N$, $\phi(0) = 0$ and different values of $z(0)$. From Eq.(3.18), $z_{cr}(0) = \sqrt{3/4} = 0.866$. Solid line: numerical results; dashed line: analytical model. In the numerical simulations $\epsilon = 0.01$, $N = 100$, $l = 10$.

Let us fix $z(0)$ and $\phi(0) = \pi$ and vary Λ. By using Eq.(3.16) we find the following critical value for the nonlinearity:

$$\Lambda_c = \frac{4\epsilon(1 - \sqrt{1 - z^2(0)})}{Nz^2(0)} \tag{3.21}$$

When $\Lambda < \Lambda_c$, z oscillates around 0 and ϕ around π. For $\Lambda = \Lambda_c$, z asymptotically reaches 0 and ϕ reaches π. Above Λ_c, we have oscillations around a value of $\neq 0$: this means that we are in a superfluid regime with the plane wave passing through the defects. In this region of parameters, the phase difference between the transmitted wave and the reflected one is on average π. This system can be therefore used to tune this phase difference. There are effectively two kind of these self-trapped π-states and they are separated by the value Λ_f corresponding to fixed point (3.20). We find

$$\Lambda_f = \frac{2\epsilon/N}{\sqrt{1 - z^2(0)}}. \tag{3.22}$$

When $\Lambda < \Lambda_f$, z oscillates around a value smaller than $z(0)$. When $\Lambda = \Lambda_f$, we are on the fixed point and it is $z(t) = z(0)$. When $\Lambda > \Lambda_f$, z oscillates around a value greater than $z(0)$. In all these three cases, the average value of $\phi = \pi$. We want to remark that

$$\frac{\Lambda_f}{\Lambda_c} = \frac{z^2(0)}{2\sqrt{1-z^2(0)}\big(1-\sqrt{1-z^2(0)}\big)}$$

and therefore, since z never is greater than 1, is always $\Lambda_f > \Lambda_c$, as might.

In Figs.7-8 we plot the angular momentum and the phase ϕ for: $\Lambda < \Lambda_c$ (where $< z >= 0$), $\Lambda = \Lambda_c$ (where for large times $< z >\to 0$), $\Lambda < \Lambda_f$ (where $< z >< z(0)$), $\Lambda < \Lambda_f$ (where $z(t) = z(0)$) and $\Lambda < \Lambda_f$ (where $< z >> z(0)$). In all the cases $< \phi >= \pi$ and the numerical solutions of Eq.(3.1) is compared with our analytical model.

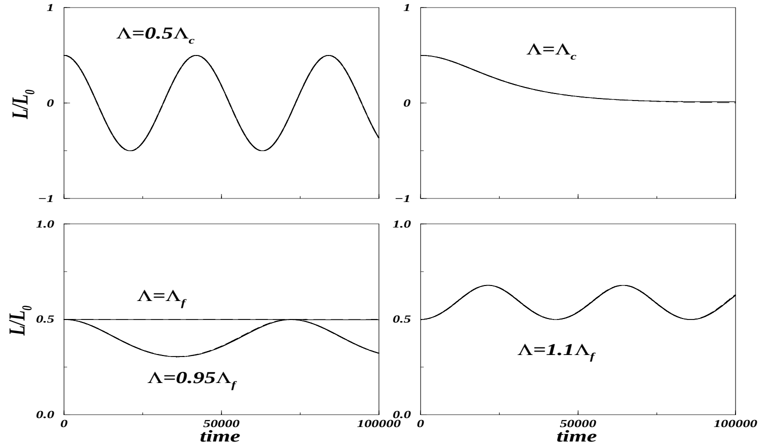

Figure 3.7: Normalized angular momentum as a function of time for $\Lambda < \Lambda_c$, $\Lambda = \Lambda_c$, $\Lambda < \Lambda_f$, $\Lambda = \Lambda_f$, $\Lambda > \Lambda_f$. Λ_c and Λ_f are given respectively by Eqs.(3.21) and (3.22). Solid line: numerical results; dashed line: analytical model. In the numerical simulations $\epsilon = 0.01$, $N = 100$, $l = 10$, $\phi(0) = \pi$, $z(0) = 0.5$.

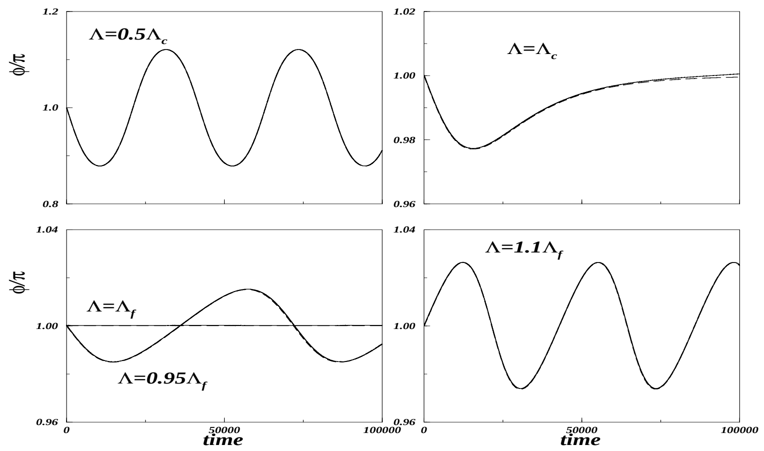

Figure 3.8: Phase vs. time for the cases of Fig.7.

3.2.1 The continuum limit

We briefly discuss the limits for recovering the CNLSE equation (in an annular geometry) from the DNLSE Eq.(3.1). Writing

$$\Lambda = \frac{2mg_0}{\hbar^2 N},$$

$$\epsilon_n = \frac{V_n m L^2}{\hbar N^2}$$

and

$$t = \frac{mL^2}{\hbar N^2 \tau},$$

with $V_n \equiv V(x = x_n)$ the defect potential in x_n, L the length of the annulus and τ the dimensionless time entering in Eq.(3.1), the CNLSE is obtained in the limit $N \to \infty$. In particular, the critical value for the pendulum oscillations Eq.(3.15) becomes $\Lambda_c = V_n m L^2/\hbar N^3 \to 0$. Therefore, approaching the continuous limit, the DNLSE pendulum regime collapses to a (strongly) self-trapped state. This prevents the emission of phonons with opposite momentum respect to the incident wave, whose energy will be eventually dissipated on a much longer time scale, according to the Landau argument.

3.3 Two and more defects

Let us consider the case of two isolated impurities

$$\epsilon_n = \epsilon_1\, \delta_{n,\bar{n}_1} + \epsilon_2\, \delta_{n,\bar{n}_2}. \tag{3.23}$$

Proceeding as in the previous chapter and using the ansatz (3.5), we find the following equations of motion for z and ϕ:

$$\begin{cases} \dot{z} = -\frac{2\epsilon_1}{N}\sqrt{1-z^2}\sin\phi - \frac{2\epsilon_2}{N}\sqrt{1-z^2}\sin(\phi+\Delta\phi_{12}) \\ \dot{\phi} = \Lambda z + \frac{2\epsilon_1}{N}\frac{z}{\sqrt{1-z^2}}\cos\phi + \frac{2\epsilon_2}{N}\frac{z}{\sqrt{1-z^2}}\cos(\phi+\Delta\phi_{12}), \end{cases} \tag{3.24}$$

where $\Delta\phi_{12} = 2k(\bar{n}_2 - \bar{n}_1)$. The effective Hamiltonian (3.11) becomes now

$$H = \frac{\Lambda z^2}{2} - \frac{2\epsilon_1}{N}\sqrt{1-z^2}\cos\phi - \frac{2\epsilon_2}{N}\sqrt{1-z^2}\cos(\phi+\Delta\phi_{12}). \tag{3.25}$$

We see that the spatial distance between the two impurities enter in the dynamics only through the relative phase $\Delta\phi_{12}$ $(mod\, 2\pi)$. Now the critical value Λ_c, and therefore the transparency of the system to the impurities, depends on this phase difference.

In the case $\epsilon_1 = \epsilon_2 \equiv \epsilon$ is easily seen that when $\Delta\phi_{12} = \pi$ the system does not feel the impurities and always the plane wave is transmitted. Similarly, when $\Delta\phi_{12} = 2\pi$, defects add and the effective defect is given by $\epsilon_{eff} = 2\epsilon$. In Fig.9 we consider the case of two equal impurities: we choose $N = 40$ sites and $l = 2$, so that $2k = \pi/5$ and $\Delta\phi_{12} = (\bar{n}_2 - \bar{n}_1)\pi/5$. When the distance between the two impurities is 5 sites, then $\Delta\phi_{12}$ and we have transparency to the impurities. This can be numerically seen by fixing $z(0)$, $\phi(0)$ and Λ and varying the distance between the impurities, as in Fig.9. In Fig.10 we plot the dynamical evolution of the angular momentum and phase for two different distances of the impurities: the numerical solution is compared with the solution of Eqs.(3.24). We see that the phase has fast jumps, because the Hamiltonian (3.25) describes two coupled non-rigid pendulum which are frustrated from $\Delta\phi_{12}$. Apart from the time intervals in which this jumps occurs, the agreement is excellent.

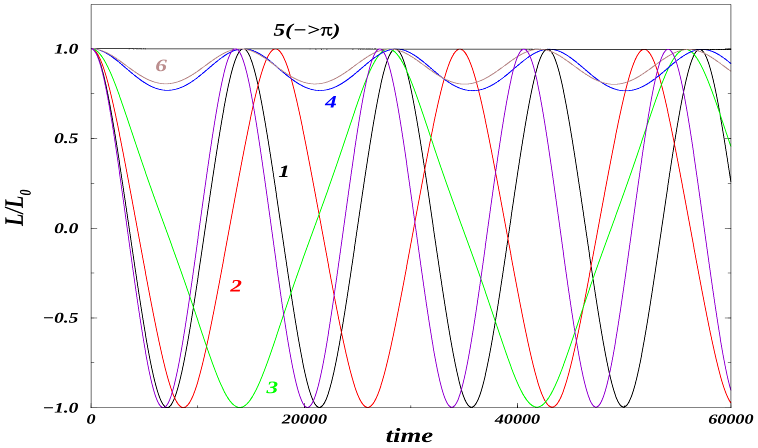

Figure 3.9: Normalized angular momentum vs. time for different distances (in sites) of two equal impurities. The different distances are signed with colors corresponding to the line under consideration. Since $\Delta\phi_{12} = (\bar{n}_2 - \bar{n}_1)\pi/5$, when the distance is 5 sites the corresponding critical value for the transition is $\Lambda_c(\Delta\phi_{12} = \pi) = 0$ and the system does not feel the impurities. When the distance is 10 sites, $\Lambda(\Delta\phi_{12} = 2\pi) = 8\epsilon/N$ and the system does not feel the effect of the impurities. The critical value for different $\Delta\phi_{12}$ is given by Eq.(3.26) and determine the transmission or not of the wave. Numerical values: $\epsilon_1 = \epsilon_2 = 0.005$, $N = 40$, $l = 2$, $\Lambda/\Lambda_c(\Delta\phi_{12} = 2\pi) = 0.5$, $z(0) = 1$, $\phi(0) = 0$.

The critical value Λ_c is determined in the following way. Let us suppose for simplicity $z(0) = 1$ and $\phi(0) = 0$: the conserved energy is $H(0) = \Lambda/2$. In the instant in which $z = 0$ it is $H(z = 0) \equiv h(\phi)/N$, where $h(\phi) =$

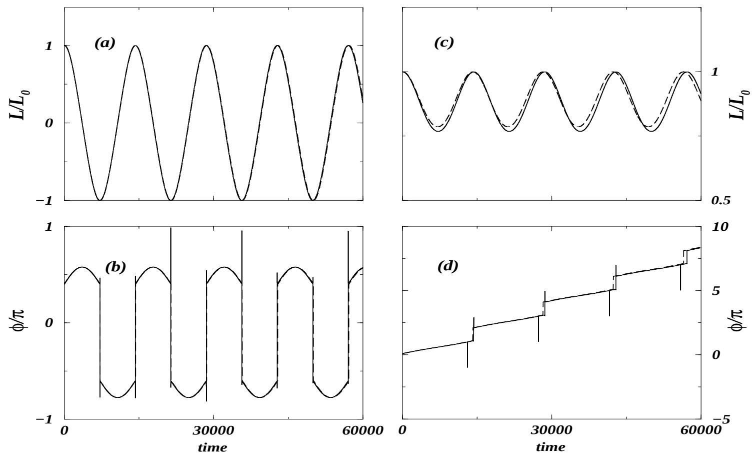

Figure 3.10: Normalized angular momentum (a) and phase (b) vs. time for distances 1 and 11 sites: $\Delta\phi_{12}$ differs by 2π and the numerical results are almost equals, as explained in the text. The solid line correspond to the numerical solution and the dashed line to the solution of Eqs.(3.24). In (c) and (d) we plot L/L_0 and ϕ/π for distances of 4 and 14. Since the critical value of Λ_c is decreased, as predicted by Eq.(3.16), we obtain a self-trapped solution, unlike of (a) and (b) where the same values are used with a different distance between the impurities. Numerical values used in the simulations: $\epsilon_1 = \epsilon_2 = 0.005$, $N = 40$, $l = 2$, $\Lambda/\Lambda_c(\Delta\phi_{12} = 2\pi) = 0.5$, $z(0) = 1$, $\phi(0) = 0$.

$-2\epsilon[\cos\phi + \cos(\phi + \Delta\phi_{12})]$. The function h has a maximum in ϕ_{max}, which is given by

$$\tan\phi_{max} = -\sin\Delta\phi_{12}/(1 + \cos\Delta\phi_{12}) :$$

the critical value for which z asymptotically reaches 0 is given by

$$\Lambda_c = \frac{2}{N} h(\phi_{max}). \tag{3.26}$$

We have a similar formula for the general case $\epsilon_1 \neq \epsilon_2$. In Fig.11 we plot Λ_c vs. $\Delta\phi_{12}$ by choosing $2k = \pi/5$ (i.e. $\Delta\phi_{12} = \pi/5$ when the two impurities are in neighbour sites) and the comparison between the numerical values and the Eq.(3.26) is showed: the system is transparent (i.e. $\Lambda_c = 0$, i.e. the wave always passes) when $\Delta\phi_{12} = 2\pi$, as the two-mode Eq.(3.25) predicts.

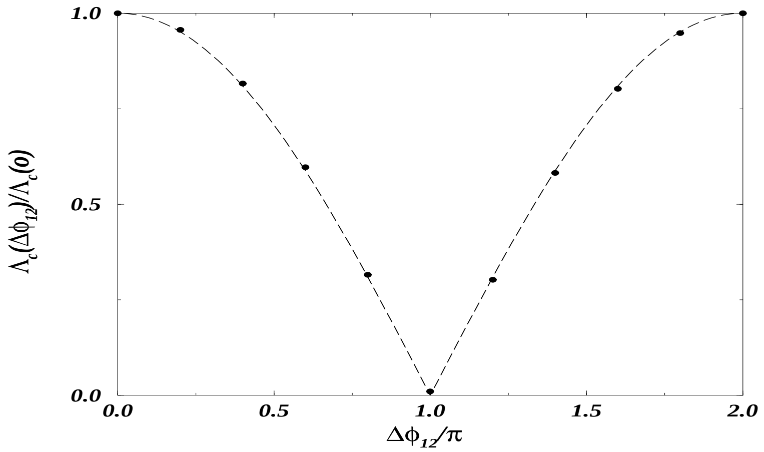

Figure 3.11: Plot of the critical value Λ_c vs. the phase difference $\Delta\phi_{12}$ associated to two equal impurities $\epsilon_1 = \epsilon_2 \equiv \epsilon$. Numerical simulations (black points) are done with $N = 40$ and $l = 2$, so $\Delta\phi_{12} = \Delta n\,\pi/5$ with Δn distance between the two impurities. The dashed line is Eq.(3.26), $\epsilon = 0.005$, $z(0) = 1$, $\phi(0) = 0$. The dashed line is Eq.(3.26) and in the plot Λ is normalized to the critical value $\Lambda_c(\Delta\phi_{12} = 0)$, i.e. with $\Delta\phi_{12}$ multiple of 2π.

The previous discussion can be generalized to the case of many impurities. The effective Hamiltonian becomes:

$$H = \frac{\Lambda z^2}{2} - \frac{2}{N}\sqrt{1-z^2}\sum_n \epsilon_n \cos\left(\phi + 2kn\right). \qquad (3.27)$$

As an example, let us consider an extended, step-like barrier: $\epsilon_n =$ *constant* for $\bar{n}_1 \leq n \leq \bar{n}_2$. Similarly to the case of two isolated impurities, we can choose the length of the step in such a way that the system does not feel the defects: e.g. with $2k = \pi/5$, when the length of the barrier is 10 sites, the sum of cosines in Eq.(3.27) vanishes and the system becomes transparent. This is illustrated in Fig.12, where we consider the same initial conditions

($z(0) = 1$ and $\phi(0)$) and different length L of the step: when this goes from 1 to 10, the system displays the "pendulum" transition to superfluidity.

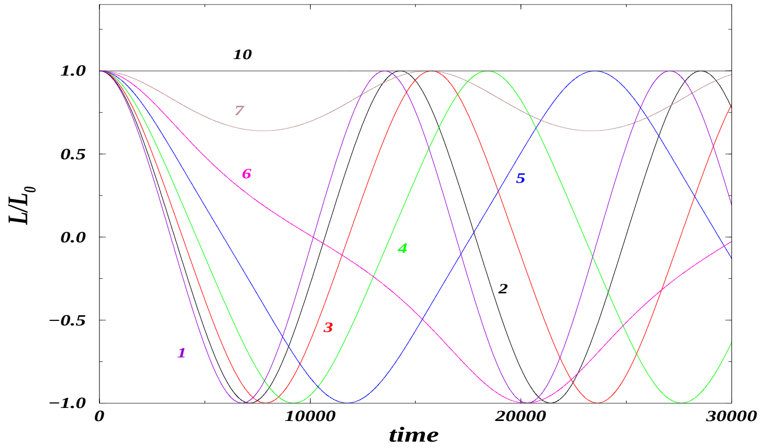

Figure 3.12: Plot of the normalized angular momentum vs. time for different lengths L of the step ($\epsilon_n = constant$ for $\bar{n} \leq n \leq \bar{n} + L - 1$). Numerical values: $N = 40$, $l = 2$, $z(0) = 1$, $\phi(0) = 0$. Λ is chosen $2\epsilon/N$, where $\epsilon = 0.01$ is the sum of the impurities. Since $2k = \pi/5$, when the length of the barrier is 10, the system is transparent to the impurities.

In the last part of this chapter we apply Eq.(3.26) to consider two important cases: an extended (gaussian) barrier and a random distributions of defects.

3.3.1 A gaussian barrier

In this subsection we consider a gaussian barrier with width σ centered in the site $\bar{n}$:

$$\epsilon_n = \frac{\epsilon}{\sqrt{\pi}\sigma} e^{-(n-\bar{n})^2/\sigma^2}. \tag{3.28}$$

We choose the coefficient in order that by changing the sum with integrals, which is correct for large N and for $\sigma > 1$, as Eq.(A.4) shows, we have

$\sum_n \epsilon_n \approx \int dn\epsilon_n = \epsilon$. As we discussed in section 3.1, the two-mode ansatz (3.5) works if ϵ is smaller than the hopping term. Always substituting sums with integrals, by using Eq.(3.26) we get

$$H \approx \frac{\Lambda z^2}{2} - \frac{2\epsilon e^{-k^2\sigma^2}}{N}\sqrt{1-z^2}\cos(\phi + 2k\bar{n}). \qquad (3.29)$$

This means that the effect of an extended barrier is equal to be a single impurity with effective strength

$$\epsilon_{eff} = \epsilon e^{-k^2\sigma^2}. \qquad (3.30)$$

E.g, with initial values $z(0) = 1$ and $\phi(0) = 0$, the critical value is obtained from Eq.(3.15) and it is given by

$$\Lambda_c = \frac{4\epsilon_{eff}}{N}. \qquad (3.31)$$

In Fig.13 we plot the normalized angular momentum for different values of Λ: the critical value found is in reasonable agreement with Eq.(3.31) and the agreement improves by increasing the number of the sites of the lattice.

It is important to remark that now the critical value depends on the momentum of the incident plane wave: when $k\sigma >> 1$, then $\Lambda_c \to 0$. This means that a wave plane with large momentum will always pass trough the barrier, as expected. In Fig.14 we compare the critical value Λ_c numerically found for different wave vectors k with the analytical prediction (3.31). The agreement is good.

3.4 Random defects

All the predicted regimes discussed so far have been found in agreement with full numerical analysis also in the case of a random distribution of de-

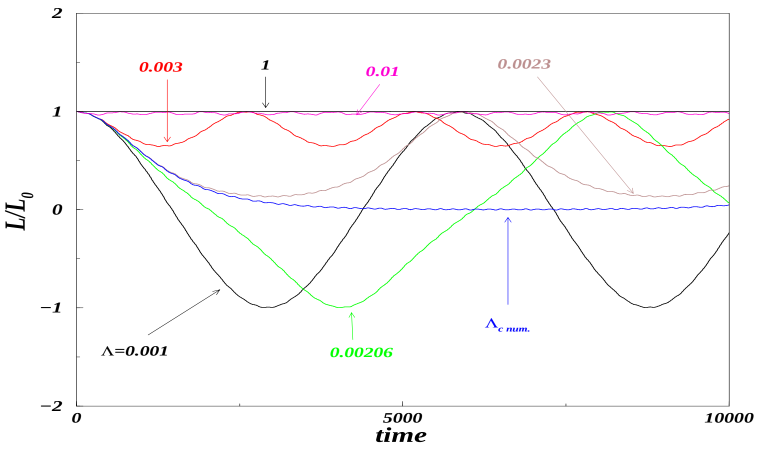

Figure 3.13: Angular momentum vs. time for different values of Λ in the case of a gaussian barrier with width $\sigma = 3$ and normalized to $\epsilon = 0.05$. The numerical critical value is 0.00228 and the value retrieved from Eq.(3.31) is 0.00206. Numerical values in the simulations: $N = 40$, $l = 2$, $z(0) = 1$, $\phi(0) = 0$.

fects. In Fig.15 we plot L/L_0 as a function of time for various Λ and a random distribution of defects ϵ_n. The critical value Λ_c calculated from Eq.(3.26), as well as the oscillations profiles, are compared with the numerical finding. As in the case of a single impurity, shown in Fig.1, also for a random uniform distribution of defects there is a critical transition of the average angular momentum. The excellent agreement between the numerical solution and the solution of Eq.(3.27), and the robustness of the two-mode ansatz in presence of an arbitrary distribution of defects, opens to the possibility of studying the competition between disorder and nonlinearity in a new perspective. The Eq.(3.27) is simple enough to offer analytical insights, and still it seems to contain all the essential ingredients to investigate the details of the superfluid - normal transition in DNLSE.

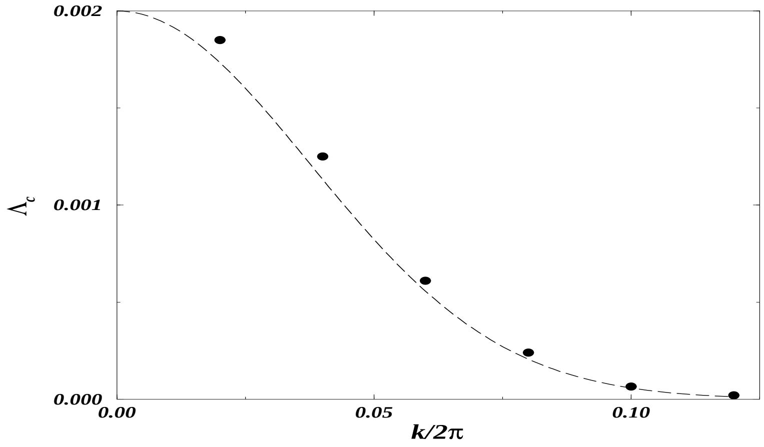

Figure 3.14: Critical value of Λ as a function of the wave vector k of the incident plane wave. Black circles: numerical results; dashed line: Eq.(3.31). Numerical values in the simulations: $N = 100$, $z(0) = 1$, $\phi(0) = 0$. The width of the barrier is $\sigma = 3$ and the sum of the impurities is 0.05. We see that, if we compare Fig.13, there is a better agreement between the numerical and analytical results: this is due to the fact that we are using a large number of sites and therefore the approximation in which Eq.(3.31) has been obtained works better.

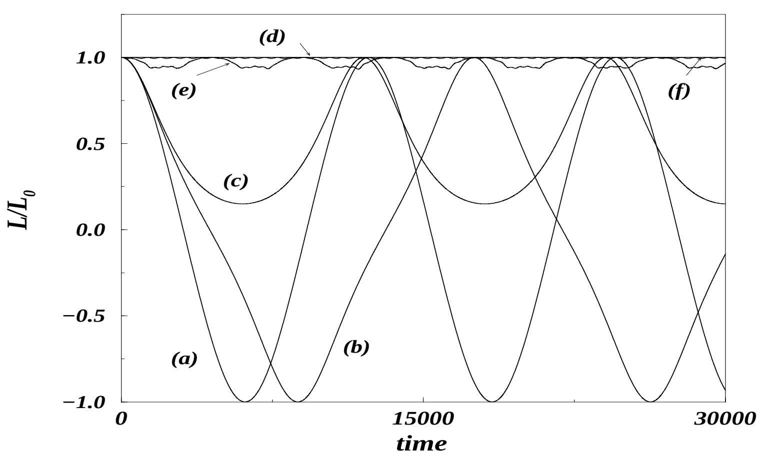

Figure 3.15: Angular momentum vs. time with a random distribution of defects for different values of $\Lambda/\Lambda_c = 0.45, 0.90, 1.01, 10, 100, 1000$ (corresponding to $(a), \cdots, (f)$) and $z(0) = 1$ and $\phi(0) = 0$. The sum of the strengths of the random impurities is 0.1 and the critical value Λ_c is given by Eq.(3.26).

Part II

OSCILLATING CURRENTS AND INTERNAL COLLECTIVE MODES IN TWO WEAKLY COUPLED BOSE-EINSTEIN CONDENSATES

Chapter 4

The Josephson current-phase relation in presence of collective modes

4.1 Introduction

In this chapter we study the Josephson effect between two Zeeman states of trapped bosonic gases. The equations which describes the dynamics are the same of the tunneling between actual double wells: the case of multiple wells (realized with an optical potential) has been considered in the previous chapters, but neglecting the dynamics of the other degrees of freedom on the traps.

The main goals of Chapters 4 and 5 are: 1) to investigate the effects of the internal modes on the Josephson oscillations [83]; 2) to discuss a way to physically realize a weak link between different hyperfine levels of a BEC and experimentally detect the Josephson oscillations between them; 3) to present experimental results of the LENS group in Firenze on the internal Josephson effect [24]. We remark that, to present date, Josephson oscillations in a double well or between two different hyperfine levels have not been yet observed. A discussion of the detection of Josephson oscillations in multiple wells has been done in Chapters 1 and 2.

In section 4.2 we consider two different hyperfine levels coupled by a laser, that induces a Josephson-like coupling between the states. The two components feel different effective harmonic traps (with different harmonic trap-curvatures and/or different positions of trap minima). Using two gaussian-profile variational wavefunctions we determine dynamical equations coupling the fractional number difference, the effective phase difference, and the rocking and breathing motions of the BEC profiles. These equations, as already mentioned, also describe one-component ground state BEC tunneling between actual double wells, considered previously in a fixed-position and rigid-profile-case, but now with BEC center-of-mass motion and collective modes included. The equations map onto the dynamics of a momentum-shortened pendulum, as found in the previous work, but now with additional pendulum-length stretching variables dependent on the profile deviations from equilibrium position and width. The five fixed point classifying five pendulum modes of oscillation about average values of 0 or π found previously are preserved, but the modes are enriched and modified. They are studied in section 4.3. In particular, the macroscopic quantum self-trapping regime still remains, in which the population imbalance between the two traps in maintained by the interatomic interaction. For arbitrary initial conditions with different frequencies competing, in terms of pendulum coordinates there is a remarkable tracing out of Lissajous-like trajectories to completely fill sharp sided figures as rectangles. The different regimes of the quantum phase dynamics show up in characteristic oscillations of the center-of-mass and density profiles, providing an experimental tool to detect and study the Josephson oscillations.

4.2 Josephson dynamics between hyperfine levels

The quantum mechanical phase-coherence of Bose-Einstein condensates (BEC) [32] reveals itself in interference fringes between overlapping freely-falling condensates [84]; in states of quantized angular momentum of vortices [85] and toroidal trap circulating flows [86]; and in Josephson-like tunneling oscillations between double-wells trap [35, 68, 87, 88]. Assuming a linear superposition of fixed-position and rigid-profile wavefunctions with time-dependent coefficients, the tunneling oscillations are described by coupled nonlinear equations for the time-dependent interwell phase difference $\phi(t)$ and the fractional number imbalance $\eta(t)$ [35]. The equations map onto the dynamics of a momentum-shortened pendulum with five distinct oscillation modes [89]. These include three types of π-states corresponding to inverted-orientations of the momentum-shortened pendulum, with restricted phase excursions about a time-averaged value $<\phi(t)>=\pi$. Two of these 'π-states' as well another running state correspond to nonzero pendulum angular momentum $<\eta(t)>\neq 0$, with self-maintained number imbalance, or “macroscopic quantum self-trapping” (MQST). Dynamical transitions at the onset of MQST states through zero frequency dips are predicted, on varying parameters through critical values [35].

Another Josephson-like tunneling systems consist of two condensate components, or BEC atoms in ground and excited states, in a single ellipsoidal trap [90, 91]. Since the two types of atoms are in different hyperfine states, they feel different effective trap potentials, with two different trap-minimum positions [90] and/or trap curvatures [91]. A full numerical solutions of the Gross-Pitaevskii equations (GPE) for the two species with strong overlap between the wavefunctions yields a rocking oscillation of the centers of mass (COM) of the wavefunctions, with varying well populations. It would be useful to generalize the two-state-tunneling model to include the BEC-profile COM and widths in order to make contact with previous works [35, 36] and to see if the pendulum analog carries through in the changed physical regime.

Here we use two gaussian-profile variational wavefunctions with time-varying positions and widths to obtain a reduced dynamical description of the interplay between oscillations of two-species phase-difference, fractional number difference and BEC-profile positions and widths (see also [92]). The oscillations are understood in a pendulum analogy. The trap potentials are harmonic, with species-dependent curvatures and positions of minima. The generalized tunneling dynamics also formally applies to one-species BEC cloud in actual double-well trap, with positions and widths that are free to oscillate. In the limit of rigid positions and widths, we recover the previous two-state model whose mechanical analog is the momentum-shortened pendulum with five distinct modes [35]. In the general case, with time-dependent positions and widths of the two condensates, we obtain an enriched momentum-shortened pendulum, with an additional “spring” stretching of the pendulum and an effective phase difference, both related to the new degrees of freedom. The fixed points and the tunneling modes of the pendulum analog are preserved, allowing for the classification and the understanding of the rich dynamics. For general initial conditions, the rocking/breathing act as oscillating torques and the trajectories of the pendulum trace out Lissajous-like patterns that fill sharp sided figures. The various types of tunneling oscillations affect the COM and centering coordinates that serve as a classical diagnostic for the quantum phase state.

4.2.1 Two-species Gross-Pitaevskii equations

The condensates are different Zeeman levels of alkali atoms. They are in harmonic trap: to fix the experimental numbers, we will refer to the experiments by JILA at Boulder [90] and by LENS at Florence [91]. We denote the two condensates of ^{87}Rb atoms by $|1>$ and $|2>$. For the LENS set-up (L), it is $|1>=|F=2,m_F=1>$ and $|2>=|2,2>$. In the JILA set-up (J), it is $|1>=|1,-1>$ and $|2>=|2,1>$. The condensates $|1>$ and $|2>$ have different magnetic momenta and feel different magnetic potentials $V_j^{(M)}$ $(j=1,2)$, which we write in the general ellipsoidal form

$$\begin{cases} V_1^{(M)}(\vec{r}) = \frac{1}{2}m[\omega_{x1}^2 x^2 + \omega_{y1}^2 y^2 + \omega_{z1}^2 (z+z_0)]^2 \\ V_2^{(M)}(\vec{r}) = \frac{1}{2}m[\omega_{x2}^2 x^2 + \omega_{y2}^2 y^2 + \omega_{z2}^2 (z-z_0)]^2 \end{cases} \tag{4.1}$$

where m is the atomic mass. In (J) the frequencies of the two traps are equals and in (L) are different. In both cases the system is cigar-shaped and the motion of condensates is along the z-direction. The main difference is that in (J) the distance between the minima of the trap potentials is smaller than the dimensions of the condensates, while is (L) is larger. This allows the study of different physical situations. The experimental values of the parameters are:

$$\begin{array}{cc} JILA & LENS \\ \omega_{x1} = \omega_{y1} = \omega_{x2} = \omega_{y2} = 2\pi \cdot 24Hz & \omega_{y2} = \omega_{z2} = \sqrt{2}\omega_{y1} = \sqrt{2}\omega_{z1} = 2\pi \cdot 130Hz \\ \omega_{z1} = \omega_{z2} = 2\pi \cdot 65Hz & \omega_{x2} = \sqrt{2}\omega_{x1} = 2\pi \cdot 12.6Hz \\ z_0 = 0.2\mu m & z_0 = 7.5\mu m \end{array}$$

The two Zeeman states $|1>$ and $|2>$ are coupled by an e.m. field with frequency ω_{ext} and strength characterized by Rabi frequency Ω_R (see Fig.1a). The detuning is defined as $\delta = \omega_{ext} - \omega_0$, where $\hbar\omega_0$ is the energy splitting between the two states (e.g., in (L) $\hbar\omega_0 \approx 2MHz$). The system is described in the rotating wave approximation by two coupled GPE (see App.C). Since

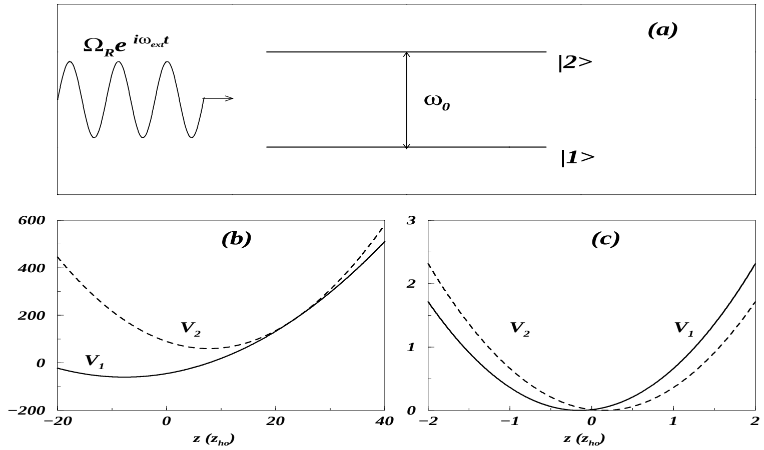

Figure 4.1: (a) Josephson coupling of the two Zeeman level $|1>$ and $|2>$ through an e.m. field with frequency ω_{ext} and strength characterized by the Rabi frequency Ω_R. (b) Magnetic potentials in LENS setup [91]: position is in units of $z_{ho} = \sqrt{\hbar/m\omega_{z1}}$ and energy in units of $\hbar\omega_{z1}$. (c) Magnetic potentials in JILA setup [90]

the motion of the condensates is almost in the z-axis, we can, to a good approximation, reduce the problem to $1D$ integrating over the transverse directions. Expressing position in units of $z_{ho} = \sqrt{\hbar/m\omega_{z1}}$, time in units of $1/\omega_{z1}$ and energy in units of $\hbar\omega_{z1}$, we obtain

$$i\begin{pmatrix}\dot{\psi}_1\\ \dot{\psi}_2\end{pmatrix} = \begin{pmatrix} T+V_1+u_{11}\mid\psi_1\mid^2+u_{12}\mid\psi_2\mid^2 & -\Omega_0 \\ -\Omega_0 & T+V_2+u_{21}\mid\psi_1\mid^2+u_{22}\mid\psi_2\mid^2\end{pmatrix}\begin{pmatrix}\psi_1\\ \psi_2\end{pmatrix} \tag{4.2}$$

with $T = -\frac{1}{2}\frac{\partial^2}{\partial z^2}$, $\Omega_0 = \Omega_R/2$ and u_{ij} (normalized) scattering lengths (see App.C). The total number of particles $N_T = N_1 + N_2$ is conserved, with $\int dz \mid \psi_j^V \mid^2 = N_j$. In (L) it is (Fig.1b)

$$\begin{cases} V_1 = \frac{1}{2}(z+z_0)^2 + \delta/2 \\ V_2 = \frac{1}{4}(z-z_0)^2 - \delta/2 \end{cases} \tag{4.3}$$

and in (J) (Fig.1c)

$$\begin{cases} V_1 = \frac{1}{2}(z+z_0)^2 + \delta/2 \\ V_2 = \frac{1}{2}(z-z_0)^2 - \delta/2 \end{cases} \tag{4.4}$$

The scattering lengths are almost degenerate: in (J) is $a_{11} : a_{12} : a_{22} = 1.03 : 1.00 : 0.97$ and in (L) $a_{11} : a_{12} : a_{22} = 1.00 : 1.00 : 0.97$. For this reason let us put $u_{11} = u_{12} = u_{22} = u$ ($u_{12} = 0$ refers to case of two non-ideal non-interacting gases). With the notation

$$\Psi = \begin{pmatrix}\psi_1\\ \psi_2\end{pmatrix},$$

the effective Lagrangian is

$$\mathcal{L} = i < \Psi^\dagger\dot{\Psi} > - < \Psi^\dagger\hat{H}\Psi > \tag{4.5}$$

where $< \cdots > = \int dz \cdots$ and

$$\hat{H} = \begin{pmatrix} T + V_1 + \frac{u}{2}\,\big(\mid \psi_1 \mid^2 + \mid \psi_2 \mid^2\big) & -\Omega_0 \\ -\Omega_0 & T + V_2 + \frac{u}{2}\,\big(\mid \psi_1 \mid^2 + \mid \psi_2 \mid^2\big) \end{pmatrix}.$$

To study the dynamics, we make a variational ansatz for the wavefunctions by using a gaussian profile and we introduce the variational wavefunctions ψ_j^V $(j = 1, 2)$ in the following way:

$$\psi_j^V(z,t) = [2/\pi\alpha_j(t)]^{1/4}\sqrt{N_j(t)}\; e^{i\phi_j(t)} \exp\Big\{ - \frac{[z - z_j(t)]^2}{\alpha_j(t)} \Big\} \cdot$$

$$\cdot \exp\Big\{ i p_j(t) \cdot [z - z_j(t)] + i\frac{\delta_j(t)}{2} \cdot [z - z_j(t)]^2 \Big\}. \tag{4.6}$$

The variational parameters are the number of particles N_j of the two condensates $(j = 1, 2)$, the phases ϕ_j, their centers z_j along the z-axis, the squares α_j of their dispersions and their respective momenta p_j (associated to z_j) and δ_j (associated to α_j) . The wavefunctions ψ_j^V are normalized in such way that $\int dz \mid \psi_j^V \mid^2 = N_j$. Let us introduce the fractional number difference

$$\eta = \frac{N_1 - N_2}{N_T}\ : \tag{4.7}$$

it is $N_{1,2} = \frac{N_T}{2}(1 \pm \eta)$.

Substituting (4.6) in (4.5), we find the Lagrangian (C.2). Using the Euler-Lagrange equations, we can derive the equations of motion for the time-dependent variational parameters. We observe that making a variational ansatz for the full $3D$ case (variational parameters are the centers $\vec{r}_j$ and the the widths in the three directions) we found a simple generalization of the equations in App.C.

4.2.2 Limiting cases

Equilibrium vales

We consider in turn increasingly complex cases, starting with equilibrium. Here, all variational parameters are time independent: we will denote the equilibrium values with a bar. We consider, for simplicity, the case of symmetrical potential (J). We have, for the symmetry, equal number of particles ($\bar{N}_1 = \bar{N}_2 = N_T/2$), equal widths ($\bar{\alpha}_1 = \bar{\alpha}_2 \equiv \bar{\alpha}$) and opposite centers ($\bar{z}_1 = -\bar{z}_2$). Furthermore $p_1 = p_2 = 0$; for $\Omega_0 > 0$ it is $\phi_1 = \phi_2 = 0$ and for $\Omega_0 < 0$ it is $\phi_1 = \pi$, $\phi_2 = 0$. The Lagrangian is $\mathcal{L} = -\bar{\mathcal{E}}$ and the energy per particle is

$$\frac{\bar{\mathcal{E}}}{N_T} = \frac{uN_T}{4\sqrt{\pi\bar{\alpha}}}(1 + e^{-4\bar{z}_1^2/\bar{\alpha}}) + \frac{1}{2\bar{\alpha}} + \frac{\bar{\alpha}}{8} + \frac{1}{2}(\bar{z}_1 + z_0)^2 - \Omega_0 e^{-2\bar{z}_1^2/\bar{\alpha}}$$

Minimizing $\bar{\mathcal{E}}$ we find the variational ground state. For $u = 0$ and $\Omega = 0$, it is $\bar{z}_1 = -z_0$. In Figs.2-3 we report the equilibrium values for $\bar{z}_1$ and $\bar{\alpha}$ for different values of Ω_0 and uN_T. As we expect, increasing uN_T the equilibrium distance between the two condensates increases for the repulsion; similarly, increasing Ω_0 the distance between the two condensates decreases.

Pure tunneling case

In the Lagrangian (C.2), the three main process are considered: tunneling (particle exchange between condensates), rocking (the condensates move in their trap potential) and breathing (the widths vary in the dynamics). As we will show, for realistic values of experimental parameters these three kind of motions interact strongly and the system shows rich dynamical behavior. But, to clarify the significant physical limits, we pass to simpler case first, in which only tunneling occurs. The condensates are supposed rigid and fixed in their equilibrium positions: $\alpha_1 = \alpha_2 = \bar{\alpha}$, $z_1 = -z_2 = \bar{z}_1$, $\delta_1 = \delta_2 = 0$ and $p_1 = p_2 = 0$. This would happen with very large frequency trap ω. The

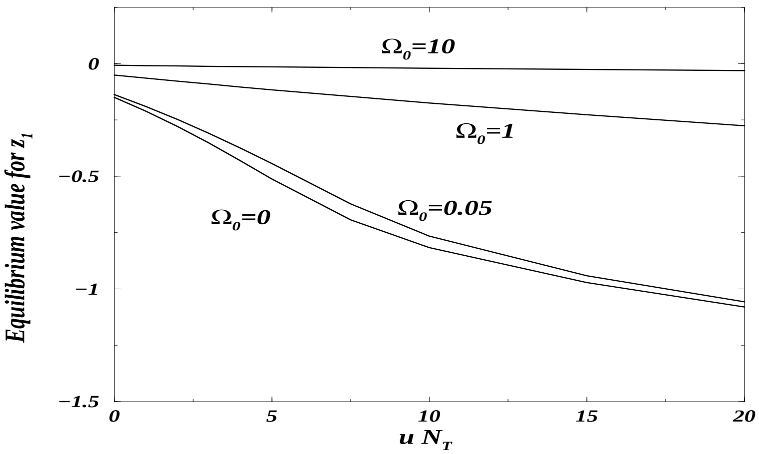

Figure 4.2: Equilibrium value for the center of mass of condensate $|1>$ vs. the mean field energy uN_T for different values of the coupling Ω_0 obtained minimizing the energy (C.3) with the JILA values.

Lagrangian (C.2) simplify

$$\mathcal{L} = -N_1\dot{\phi}_1 - N_2\dot{\phi}_2 - \frac{u}{2\sqrt{\pi\bar{\alpha}}}(N_1^2+N_2^2+2N_1N_2e^{-\bar{z}^2/\bar{\alpha}}) + 2\bar{\Omega}\sqrt{N_1N_2}\cos\phi. \quad (4.8)$$

where $\phi = \phi_2 - \phi_1$, $\bar{z} = \bar{z}_1 - \bar{z}_2$ and $\bar{\Omega} = \Omega_0\ e^{-\bar{z}^2/2\bar{\alpha}}$, and the equations are given by

$$\begin{cases} \dot{\eta} = -2\bar{\Omega}\sqrt{1-\eta^2}\sin\phi \\ \dot{\phi} = 2\bar{\Omega}\left[\frac{\eta}{\sqrt{1-\eta^2}}\cos\phi + \Lambda\eta\right] + \Delta E \end{cases} \quad (4.9)$$

where $\Lambda = \frac{uN_T(1-e^{-\bar{z}^2/\bar{\alpha}})}{2\bar{\Omega}\sqrt{\pi\bar{\alpha}}}$ and, e.g. in (J), $\Delta E = \frac{1}{2}(\bar{z}_1 - z_0)^2 - \frac{1}{2}(\bar{z}_2 + z_0)^2 + \delta$: with $\delta = 0$ is $\Delta E = 0$. Similar formulas for ΔE holds in (F). Furthermore the parameter

$$\Lambda = \frac{uN_T(1-e^{-\bar{z}^2/\bar{\alpha}})}{2\bar{\Omega}\sqrt{\pi\bar{\alpha}}} \quad (4.10)$$

governs the transitions between different dynamical regimes, as we now discuss.

The dynamical equations (4.9) for the phase and the current were first obtained in [7] for the single-component (ground state) tunneling between

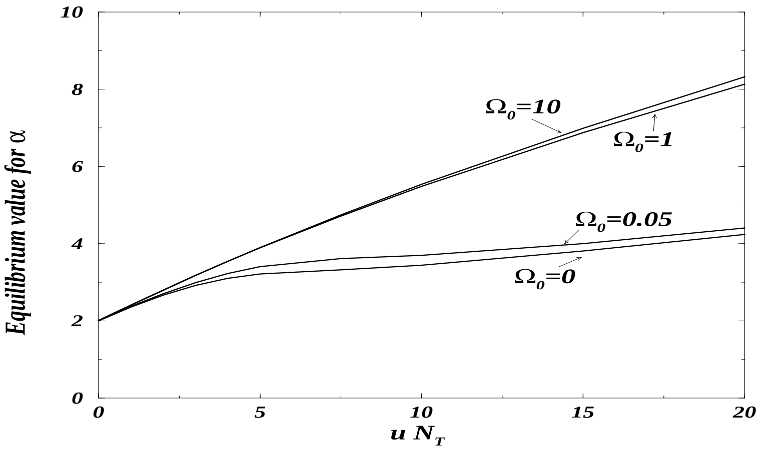

Figure 4.3: Equilibrium value for the width of condensate $|1>$ vs. the mean field energy uN_T for different values of the coupling Ω_0.

double-wells. The oscillations correspond to those of a pendulum of momentum p_ϕ ($\equiv \eta$), tilt angle ϕ, and Hamiltonian $H/2\bar{\Omega} = \frac{1}{2}\Lambda p_\phi^2 - \sqrt{1-p_\phi^2}\cos\phi$. The (unit-normalized) length of the pendulum $\sqrt{1-p_\phi^2}$ is reduced by the momentum: 'faster'='shorter'. The locus of the pendulum is traced out [7] by its coordinates $(X,Y) = (\sqrt{1-p_\phi^2}\sin\phi, -\sqrt{1-p_\phi^2}\cos\phi)$. There are five distinct types of oscillations (with characteristic small-amplitude frequencies found by linearization) around fixed points ϕ^*, η^* and with different time average values $<\phi>$, $<\eta>$. These are summarized as below and displayed in Figs.4-5:

a) zero-state oscillations around $\phi^* = 0$, $\eta^* = 0$, with time average values $<\phi>_t = 0$, $<\eta>_t = 0$ and $\sqrt{1+\Lambda}$, as in Figs.4a-5a; the small oscillations have (linearized) frequency $\omega_0 = \bar{\Omega}\sqrt{1+\Lambda}$;

b) running-state rotations with $<\eta>_t \neq 0$, $<\phi>_t \sim t$, as in Figs.4b-5b;

c) π-state oscillations around $\phi^* = \pi$, $\eta^* = 0$, with $<\phi>_t = \pi$, $<\eta>_t = 0$ and $\omega_0 = \bar{\Omega}\sqrt{1-\Lambda}$ ($\Lambda < 1$), as in Figs.4c-5c; the small oscillations have (linearized) frequency $\omega_0 = \bar{\Omega}\sqrt{1-\Lambda}$ ($\Lambda < 1$);

d) π-state rotations around $\phi^* = \pi$, $\eta \neq 0$, corresponding to π self-trapping, as in Figs.4d-5d. (There are two different kinds of such self-trapped π-states: $< \eta >_t < \eta_c$ and $< \eta >_t > \eta_c$, with η_c.)

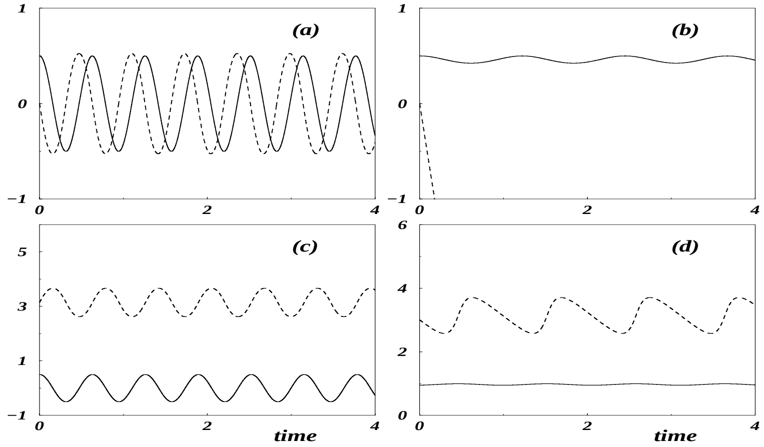

Figure 4.4: Plot of the population imbalance η (solid line) and the phase ϕ (dashed line) in the pure tunneling case for: (a) zero-state oscillations ($\Omega_0 = 5$, $\eta(0) = 0.5$, $\phi(0) = 0$); (b) self-trapped states ($\Omega_0 = 0.2$, $\eta(0) = 0.5$, $\phi(0) = 0$); (c) π-oscillations ($\Omega_0 = 5$, $\eta(0) = 0.5$, $\phi(0) = \pi$); (d) π-rotations ($\Omega_0 = 0.85$, $\eta(0) = 0.85$, $\phi(0) = 3$). The value of the other parameters are from [90]: $N_T = 23000$ and $z_0 = 0.15$.

We observe that, with $\Omega \to \infty$, then $\bar{z}_i \to 0$, $\bar{\Omega} \to -\Omega_0$ and the tunneling frequency ω_T is given by $\omega_T^2 = 4\Omega_0^2$ as we expected [35].

The non-zero average angular momentum 'rotation' states b), d) in the pendulum analogy correspond to a non-zero, self-maintained population imbalance $p_\phi \equiv \eta \neq 0$: macroscopic quantum self-trapping (MQST) [7,8]. The transition from non-MQST to MQST oscillations can be induced (for given initial conditions) by varying Λ in such way that $H(t=0) > 2\bar{\Omega}$: this defines

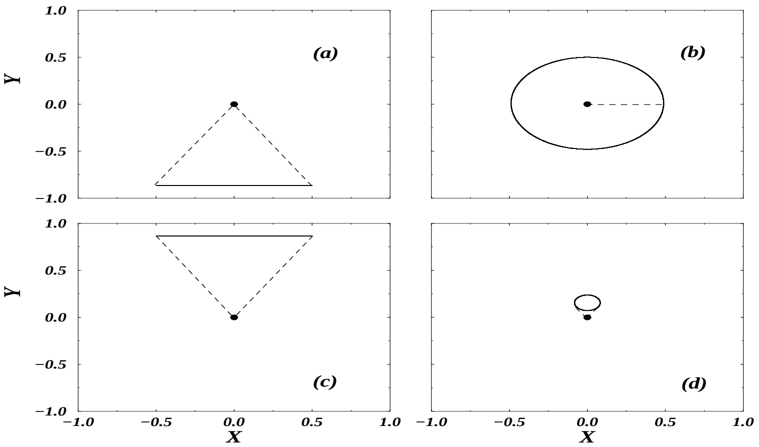

Figure 4.5: Plots of the (unit normalized) pendulum coordinates $(X, Y) = (\sqrt{1-\eta^2}\sin\phi, -\sqrt{1-\eta^2}\cos\phi)$ corresponding to cases (a),...,(d) of Fig.5.

a critical value Λ_c, depending upon the initial conditions such that for $\Lambda > \Lambda_c$ we have MQST.

Experimentally, we can vary Λ simply by varying the strength of the coupling e.m. field. Fig.6 shows, for the JILA setup, the dependence of Λ on Ω_0. To have an idea of the experimental numbers, when $\eta(0) = 1$ and $\phi(0) = 0$, the critical value of Λ is $\Lambda_c = 4$: when $\Omega_0 \approx 300\,Hz$ it is $\Lambda \approx 0.01$ and for $\Omega_0 \approx 20\,Hz$ it is $\Lambda \approx 10$, allowing for the detection of the transition.

Rocking and breathing without tunneling

To understand the interplay between rocking and breathing, we consider the Lagrangian (C.2) with $\Omega = 0$. First, we consider the case of two non-interacting non-ideal gases ($u_{12} = 0$ and $u_{11} = u_{22} = u$): each condensate is then uncoupled to the other. In the equilibrium, the energy for particle for condensate (e.g.) $|1>$ is $\bar{\mathcal{E}}/N_1 = uN_1/2\sqrt{\pi\bar{\alpha}_1} + 1/2\bar{\alpha}_1 + \bar{\alpha}_1/8$, with $N_1 = N_T/2$. In the case $u_{11} = 0$, minimizing $\bar{\mathcal{E}}$ in respect to $\bar{\alpha}_1$ gives $\bar{\alpha}_1 = 2$, as might: indeed the ground state is proportional to $e^{-(z-z_0)^2/2z_{ho}^2}$. In the

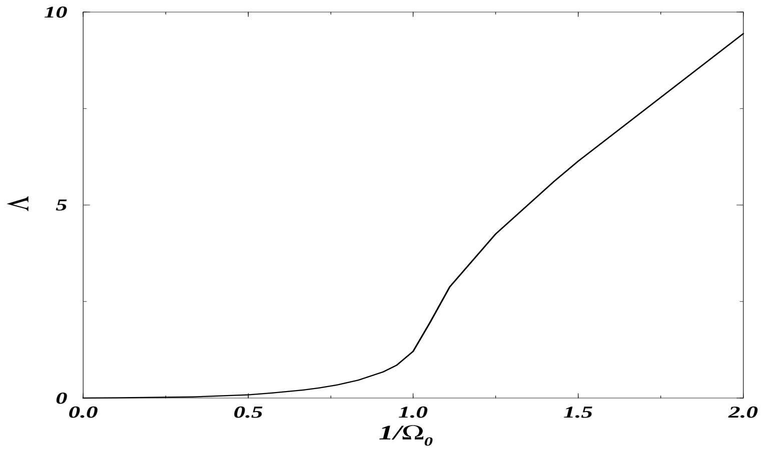

Figure 4.6: Plot of the parameter Λ vs. the inverse of the coupling Ω_0: when Λ is smaller (greater) than the critical value Λ_c, zero- (π-)states are found.

case $u_{11} \neq 0$, it is $\bar{\alpha}_1 = \sqrt{4 + u_{11} N_T \sqrt{\bar{\alpha}_1/\pi}}$, from which we can see that $\bar{\alpha}_1$ increases with $u_{11} N_T$.

Let compare the frequencies of rocking and breathing, respectively ω_R and ω_B. The equation for the center of mass z_1 is given by $\ddot{z_1} = -(z_1 + z_0)$, i.e. $\omega_R = 1$. In scaled unit this means that the frequency of condensate oscillations is equal to the trap frequency. We retrieve in our case that the mean-field interactions in a single BEC, contained in u_{11}, does not affect the center of mass motion of the condensate, according exact results (see e.g. [32]). For the breathing, denoting the deviations from equilibrium with a tilde ($\tilde{\alpha}_1 = \alpha_1 - \bar{\alpha}_1$), it is $\ddot{\tilde{\alpha}}_1 = -\omega_B^2 \tilde{\alpha}_1$, with

$$\omega_B^2 = \frac{16}{\bar{\alpha}_1^2} + 3\frac{u_{11} N_T}{\sqrt{\pi}\bar{\alpha}_1^{3/2}}. \tag{4.11}$$

With typical values, in (J) is $\omega_B^2 \approx 5 - 10$ (with Ω_0 ranging from $10\,Hz$ to $1\,kHz$). We observe also that with $u_{11} = 0$ we retrieve the known result $\omega_B = 2\omega_R$.

To conclude, we consider the case in which the interspecies scattering length $u_{12} = u$ is present. Let $\tilde{z} = \tilde{z}_1 - \tilde{z}_2$ and $\tilde{\alpha} = \tilde{\alpha}_1 - \tilde{\alpha}_2$: linearizing we find $\ddot{\tilde{z}} = -\omega_R^2 \tilde{z}$ and $\ddot{\tilde{\alpha}} = -\omega_B^2 \tilde{\alpha}$, with $\omega_R^2 = 1 + (1/N_T)(\partial^2 \mathcal{E}_{MF}/\partial z_1^2)_{eq}$ and ω_B given by (4.11). We conclude that for experimental values the rocking and breathing are both present and that the breathing frequency is ≈ 3 times than the rocking frequency.

4.2.3 Exact relations

In the general case, we can use some important exact relations. From the equations of motion we can show, as expected, that

$$\begin{cases} < \hat{z} >= N_1 z_1 + N_2 z_2 \equiv N_T \mathcal{Z}_{COM} \\ < \hat{P} >= N_1 p_1 + N_2 p_2 \equiv \mathcal{P}_{COM} \\ \frac{d}{dt} < \hat{z} >= \mathcal{P}_{COM} \\ \frac{d}{dt} \mathcal{P}_{COM} = -\frac{\partial}{\partial z_1} < V_1 > -\frac{\partial}{\partial z_2} < V_2 > \end{cases} \tag{4.12}$$

with $< V_j >=< \psi_j^* V_j \psi_j >$, $< \hat{z} >=< \Psi_V^\dagger \; z \; \Psi_V >$ and $< \hat{P} >=< \Psi_V^\dagger \; (-i\frac{\partial}{\partial z}) \; \Psi_V >$. We find for the JILA experimental setup

$$\ddot{\mathcal{Z}}_{COM} = -\mathcal{Z}_{COM} - z_0 \eta. \tag{4.13}$$

Notice that these classical position and momentum variables are not directly dependent on the quantum phase difference and its sinusoidal Josephson variations, being dependent on number imbalance η. It turns out therefore that π-states with $< \phi > \neq 0$ have their signature in characteristic variations of the position variables, that serves as classical diagnostic of quantum states.

Furthermore, it has to be stressed that Eq.(4.13) is the analog with the two coupled condensates of the cited exact result, valid for one single condensate, that the mean-field interactions does not enter in the equation of the center of mass. Now the two condensates are coupled by the two-body interactions between the particles of $|1>$ and those of $|2>$ (proportional to u_{12}), and by the external e.m. field (proportional to Ω_0). In agreement to the previous result, only the latter term affects the COM dynamics: if z_0=0, despite the mean-field terms, the COM harmonically oscillates.

4.3 Internal collective modes versus Josephson oscillations

In this section we discuss how the oscillation modes are modified by the motion of condensates and how they are experimentally detectable. We also study the interplay between the current-phase dynamics and the motion of the center of mass. Indeed, while it is an hard job to measure the interwell phase $\phi(t)$, the positions of the centers $z_i(t)$ and the population imbalance η are pretty easy to measure and they gives $\mathcal{Z}_{COM} = \frac{1}{2}(z_1 + z_2) + \frac{\eta}{2}(z_1 - z_2)$. In such way the motion of the COM gives a clear signature of the various oscillation modes.

Time-averaging the (4.13) we can easily see that the average value of the imbalance η determine the average value of the COM position. Let $<\eta>_t = \frac{1}{t}\int_0^t d\tau \eta(\tau)$: when $<\eta>_t = 0$, as in zero-state oscillations, we have $<\mathcal{Z}_{COM}>_t$ vanishing. In the same way, when $<\eta>_t \neq 0$, as in running states, then $<\mathcal{Z}_{COM}>_t \neq 0$. In particular, varying the strength of the laser Ω_0 (or/and the distance z_0 between the traps), we can go from the zero-state oscillations regime (with $<\mathcal{Z}_{COM}>_t = 0$) to the MQST regime (with $<\mathcal{Z}_{COM}>_t \neq 0$): measuring $\mathcal{Z}_{COM}$ we can detect the transition.

We will consider as initial condition for the widths

$$\alpha_1(0) = \alpha_2(0) = \bar{\alpha}. \tag{4.14}$$

From an experimental point of view, the initial condition (4.14) is very reasonable, because from an experimental point of view it is quite simple to move suddenly the magnetic traps, changing therefore the initial positions and not the initial widths. However, we stress that with a sudden change of trap frequency, the initial width could be different to the equilibrium ones.

Since the breathing frequency is greater than the rocking frequency (as previously discussed), first we will study the case in which the condensate can move, but they are rigid ($\bar{\alpha}_1 = \bar{\alpha}_2 \equiv \bar{\alpha}$). The effect of the breathing will be also considered, but the qualitative results of the "tunneling+rocking" case will hold.

The Lagrangian (C.2) is now

$$\mathcal{L} = -N_1\dot{\varphi}_1 - N_2\dot{\varphi}_2 + N_1 p_1 \dot{z}_1 + N_2 p_2 \dot{z}_2 - \frac{u}{2\sqrt{\pi\bar{\alpha}}}(N_1^2 + N_2^2 + 2N_1N_2 e^{-z^2/\bar{\alpha}}) +$$

$$-\frac{N_1}{2}p_1^2 - \frac{N_2}{2}p_2^2 - \frac{N_1}{2}(z_1+z_0)^2 - \frac{N_2}{2}(z_2-z_0)^2 + 2\Omega_{eff}\sqrt{N_1N_2}\cos\tilde{\phi}. \tag{4.15}$$

and the equations of motion for the relative population and the phase are

$$\left\{ \begin{array}{l} \dot{\eta} = -2\Omega_{eff}\sqrt{1-\eta^2}\sin\tilde{\phi} \\ \dot{\tilde{\phi}} = 2\Omega_{eff}\frac{\eta}{\sqrt{1-\eta^2}}\cos\tilde{\phi} + \frac{uN_T(1-e^{-z^2/\bar{\alpha}})}{\sqrt{\pi\bar{\alpha}}}\ \eta + \Delta E_{eff} \end{array} \right. \tag{4.16}$$

where $z = z_1 - z_2$, $p = p_1 - p_2$, $\tilde{\phi} = \phi_2 - \phi_1 + \frac{1}{2}z(p_1+p_2)$ and the effective Josephson coupling is

$$\Omega_{eff}(t) = \Omega_0\, e^{-z^2/2\bar{\alpha} - \bar{\alpha}p^2/8}. \tag{4.17}$$

Furthermore $\Delta E_{eff} = \frac{1}{2}(z\dot{P} - p\dot{Z}) + \frac{<V_1>}{N_1} - \frac{<V_2>}{N_2} + \frac{p_1^2}{2} - \frac{p_2^2}{2}$ (with $Z = z_1 + z_2$ and $P = p_1 + p_2$). According the general result shown in the App.C, the effective Josephson coupling does not depend on the center-of-mass variables.

The (4.16) have the standard form of the Josephson equations (4.9), but now the Josephson coupling and the others parameters are time dependent and they are connected to the dynamics of the whole system. Furthermore we have the phase difference $\phi = \phi_2 - \phi_1$ is substituted by the dynamical phase $\tilde{\phi}$ (in particular, in COM frame they are identical). For brevity, from now we omit the tilde on ϕ.

We stress that the effective Josephson coupling (4.17) depends now also on the relative distance between the two centers: in such way, using the pendulum analogy, the normalized length of the pendulum is

$$\sqrt{1-\eta^2}\, e^{-z^2/2\bar{\alpha} - \bar{\alpha}p^2/8}, \tag{4.18}$$

where η is the momentum: the previous momentum-shortened pendulum is enriched by an additional compression of the pendulum length with an anharmonic spring. The question arises on what happens to the five oscillation modes: we will see it in the next sections.

The equations for the relative position z and the relative impulse p are

$$\begin{cases} \dot{z} = p + \bar{\alpha}\Omega_{eff}\frac{p\cos\phi}{\sqrt{1-\eta^2}} - z\frac{d}{dt}\log\sqrt{1-\eta^2} \\ \dot{p} = -\eta\dot{P} + \frac{2uN_T}{\bar{\alpha}\sqrt{\pi\bar{\alpha}}}ze^{-z^2/\bar{\alpha}}(1-\eta^2) - (z - 2z_0 + \eta Z) - 4\Omega_{eff}\sqrt{1-\eta^2}\frac{z}{\bar{\alpha}}\cos\phi. \end{cases} \tag{4.19}$$

The linearization of Eqs. (4.16), (4.19) shows that there is a peculiar decoupling of the relative motion dynamics from the population dynamics: e.g. we linearize around $\eta^* = 0$ and $\phi^* = 0, \pi$ (with $\Omega_0 > 0$). Denoting with tildes the deviation from equilibrium values, we found

$$\Delta E_{eff} \approx (z_0 + \bar{z}_1)\tilde{Z}$$

where, we remember, $Z = z_1 + z_2$ and $P = p_1 + p_2$. To have the correct linearized equation for $\dot{p}$ we observe that $\frac{d}{dt}(N_i p_i) = -\frac{\partial \mathcal{E}}{\partial z_i}$: using the fact that $(\partial \mathcal{E}/\partial z_i)_{eq} = 0$ we obtain finally

$$\begin{cases} \ddot{\eta} \approx -\omega_T^2 \eta - 2\bar{\Omega}(z_0 + \bar{z}_1)\tilde{Z} \\ \ddot{\tilde{Z}} = -2(z_0 + \bar{z}_1) - \tilde{Z}. \end{cases} \tag{4.20}$$

and

$$\ddot{\tilde{z}} \approx -\omega_R^2 \tilde{z} \tag{4.21}$$

where $\omega_T^2 = 4\bar{\Omega}^2(1 + \Lambda)$ and $\omega_R^2 = (1 + \bar{\alpha}\bar{\Omega})(4B/N_T + 4C/N_T + 1)$, with $B = (\partial^2 \mathcal{E}_{MF}/\partial z_1^2)_{eq}$ and $C = (\partial^2 \mathcal{E}_{Jos}/\partial z_1^2)_{eq}$. In the small oscillations regime we have the relative position z decouples from the population dynamics. Furthermore in the $uN_T \to 0$ limit (for which $\bar{z}_1 = -z_0$) all the oscillation modes decouples. This decoupling is the main reason for which the motions of the condensates does not destroy the oscillation modes of the momentum-shortened pendulum.

4.3.1 Zero-state oscillations

These oscillations around $\eta = 0$ and $\phi = 0$ correspond to small values of the control parameter (4.10): with the values given in [90], Ω_0 has to take e.g. the reasonable value of $\sim 500\ Hz$. To begin, we consider two types of initial conditions: the centers displaced in such way that $z_1(0) + z_2(0) = 0$, with $\eta(0) = 0$; and a deviation from the equilibrium population ($\eta(0) \neq 0$).

In Fig.7, we consider the following initial conditions: (1) only displacement of the centers from their equilibrium values ($z_1(0) = 4\bar{z}_1$, $z_2(0) = -z_1(0)$, $\eta(0) = 0$); (2) only displacement of η from its equilibrium values ($z_1(0) = \bar{z}_1$, $z_2(0) = \bar{z}_2$, $\eta(0) = 0.5$). In the case (1) the population does not oscillate: since in the dynamics $\eta = 0$, from (4.13) follows that $\mathcal{Z}_{COM}$ harmonically oscillates (Fig.7a). Then the pendulum length (4.18) oscillates in this anharmonic way and the trajectory in the plane (X, Y) is proportional to Y-axis (Fig.7b). In the case (2), at contrary, η oscillates: also $\mathcal{Z}_{COM}$, with average vanishing (Fig.7c). The trajectory in the plane (X, Y) is as in Figs.5, and for the particular values considered, it is almost a line proportional to X-axis (Fig7d).

The composition of these two motions results in a Lissajous figure. Choosing both an initial deviation of η and a displacement of the centers ($z_1(0) = 4\bar{z}_1$, $z_2(0) = -z_1(0)$, $\eta(0) = 0.5$), we have $< \eta >_t = 0$ and $< \mathcal{Z}_{COM} >_t = 0$ (Fig.8a). The trajectory in the (X, Y) plane is in Fig.8b. The same structure of the zero-state oscillations has been verified for other more irregular initial conditions. In Fig.8 we plot also the case in which the two traps are suddenly displaced of a same amount. With $z_1(0) = 4\bar{z}_1$, $z_2(0) = z_1(0) + 2 \mid \bar{z}_1 \mid$ and $\eta(0) = 0$ (Fig.8c) or $\eta(0) = 0.5$ (Fig.8d): in both cases $< \eta >_t = 0$ and $< \mathcal{Z}_{COM} >_t = 0$ and zero-state oscillations are found. Varying Ω_0 and moving the trap, we can directly detect the MQST transition (see below).

What is really interesting is that such structure of oscillations holds both for small and huge displacements from the equilibrium values. When the centers and η are both heavily displaced, the combination of the two motion always results in a Lissajous figure, but $< \eta >_t = 0$ and $< \mathcal{Z}_{COM} >_t = 0$. The reason for which these highly nonlinear equations have this behavior is that, when $Z_{COM} >> z_0\eta$, then from (4.13) its motion is harmonic.

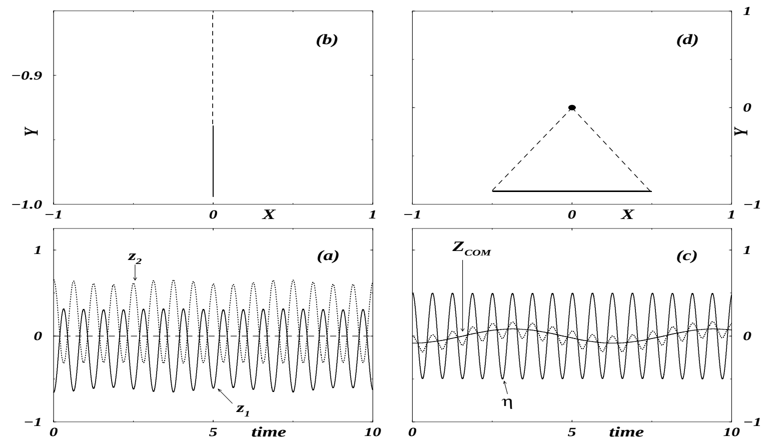

Figure 4.7: (a) Plot of the centers positions z_1, z_2 and (dashed line) η. Initial conditions: traps equally populated ($\eta(0) = 0$) and displacements of the centers from their equilibrium values ($z_1(0) = 4\bar{z}_1$, $z_2(0) = -z_1(0)$). (b) Plot of the pendulum coordinates X, Y and same initial conditions as before. (c) Plot of the center of mass Z_{COM}, population imbalance η and (dotted line) geometrical center $Z = z_1 + z_2$. Initial conditions: only displacement of η from its equilibrium values ($z_1(0) = \bar{z}_1$, $z_2(0) = \bar{z}_2$, $\eta(0) = 0.5$). (d) Pendulum coordinates with initial conditions as in (c). In all cases we use experimental values from [90]: $\Omega_0 = 5$, $N_T = 23000$, $z_0 = 0.15$, $\phi(0) = 0$.

Before to conclude the discussion of 0-states, we remark that including in the dynamics also the widths time-dependent (with the initial condition (4.14)) does not modify the previous discussion: yet, the Figs.7-8 are practically the same.

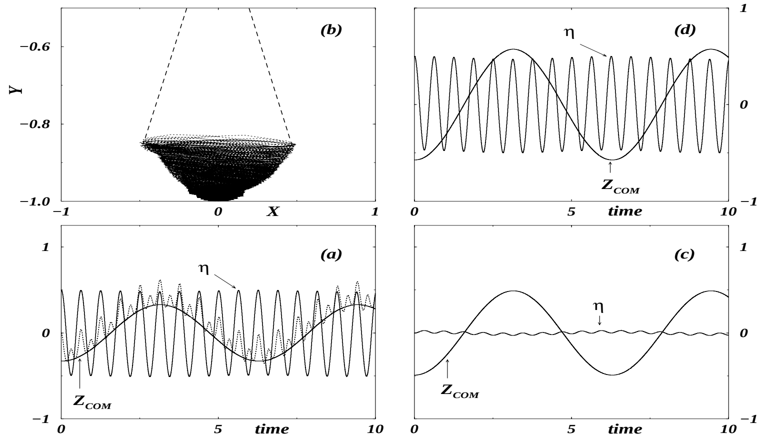

Figure 4.8: (a) Plot of the center of mass Z_{COM}, population imbalance η and (dotted line) geometrical center $Z = z_1 + z_2$. Initial conditions: both an initial deviation of η and a displacement of the centers ($z_1(0) = 4\bar{z}_1$, $z_2(0) = -z_1(0)$, $\eta(0) = 0.5$). (b) Plot of the pendulum coordinates X, Y and same initial conditions as before. (c) Plot of Z_{COM} and η when the two traps are suddenly displaced of a same amount ($z_1(0) = 4\bar{z}_1$, $z_2(0) = z_1(0) + 2 \mid \bar{z}_1 \mid$) and $\eta(0) = 0$. (d) Plot of Z_{COM} and η as in (c), but with $\eta(0) = 0.5$. The other parameters are the same indicated in the caption of Fig.7.

4.3.2 Running states: Macroscopic Quantum Self-Trapping

Let vary Ω_0 and/or the trap distance z_0, in such way that the parameter Λ, given by (4.10), is in the self-trapping region. In Fig.9 we consider the case of $z_0 = 2$ and $\Omega_0 = 0.1$. The MQST is characterized by $< \eta >_t \neq 0$ and $< \phi >_t \sim t$; in the pendulum analog, this means that the pendulum does complete oscillations. The classical signature, as previously discussed, is given by $< \mathcal{Z}_{COM} >_t \neq 0$.

The numerical solution of the equations of motion shows that the MQST is not destroyed by the internal modes. In Fig.9a we plot the time average $<$

$\eta >_t$ and $< \mathcal{Z}_{COM} >_t$: both are not equal to 0. The corresponding behaviour of the pendulum is illustrated in Fig.9b. We see that the trajectory is not closed as in the pure case (i.e. without internal modes), but yet the pendulum does full oscillations. and, correspondingly, the phase ϕ runs (Fig.9c). The inclusion of time-dependent widths make the full oscillations of the pendulum chaotic, but the self-trapped structure is preserved. In Fig.9d we plot the pendulum coordinates in this case.

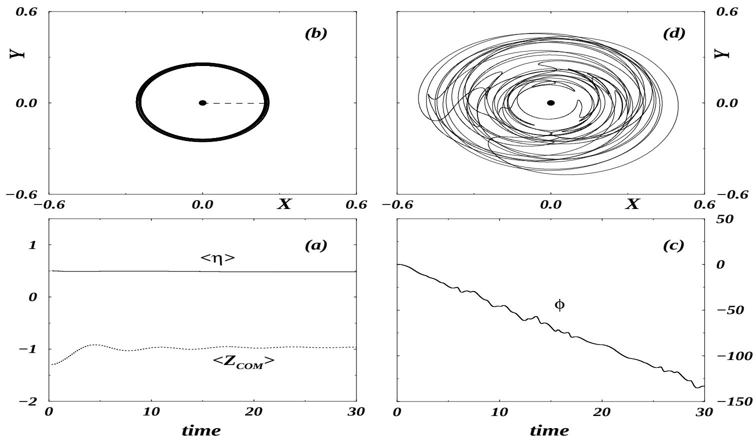

Figure 4.9: (a) Plot of the time averages of the center of mass Z_{COM} and population imbalance η. (b) Plot of the pendulum coordinates X, Y. (c) Plot of phase ϕ. (d) Plot of the pendulum coordinates X, Y when the width of the condensates is taken time-dependent (with initial value (4.14). In all cases the initial conditions are $\eta(0) = 0.5$ and centers in their equilibrium position ($z_1(0) = 4\bar{z}_1$, $z_2(0) = -z_1(0)$). Furthermore, $\Omega_0 = 0.1$, $N_T = 23000$, $z_0 = 2.0$, $\phi(0) = 0$.

4.3.3 π-state oscillations and rotations

In this subsection we discuss the π-state oscillations and rotations in presence of the internal modes. In Fig.10a, we plot the population imbalance and the phase for a π-state: we see that the motion of the center of mass preserve this regime. If we plot the pendulum portrait for long time (until $t = 100$ in Fig.10b), we see that the Lissajous trajectory fill a closed rectangle. We also show in Fig.10c what happens if the initial condition for the centers is not the equilibrium value which minimize the energy (C.3), but it is given by the minimum of (C.3) with $\phi = \pi$: we can see that the π-state is not longer maintained. We remark that the initial condition $\phi(0) = \pi$ and the initial equilibrium values for the centers and the widths of the condensates can be in principle realized using phase-engineering techniques [93]. The effect of the inclusion of the breathing mode is dramatic: in Fig.10d we plot the pendulum portrait for long times (as in Fig.10b, until $t = 100$): for small times, there is no difference, but after the pendulum goes down. However, the time window in which the π-state can be detect in the full case is the order of $\approx 100\,ms$, which is a very reasonable time from an experimental point of view.

In conclusion we mention that the effect of the center of mass motion is to destroy the π-rotations with the experimental numbers and that a possible scenario in which the π-rotations can be detect is connected to a variation of the scattering lengths (obtained with Feshbach resonances).

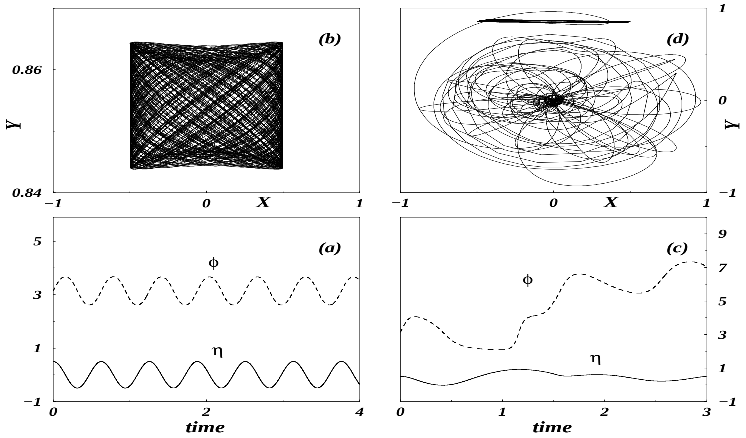

Figure 4.10: (a) Plot of the population imbalance η and the phase ϕ in a π-state. (b) Pendulum portrait (until $t = 100$, scaled units). (c) Plot of η and ϕ with initial position of centers given by energy minimization with $\phi = \pi$. (d) Pendulum coordinates X, Y until $t = 100$ when the width of the condensates is taken time-dependent, with initial value (4.14). In all cases the initial conditions are $\eta(0) = 0.5$, $\phi(0) = \pi$ and centers in their equilibrium position ($z_1(0) = 4\bar{z}_1$, $z_2(0) = -z_1(0)$); furthermore, $\Omega_0 = 5$, $N_T = 23000$, $z_0 = 0.15$.

Chapter 5

Experimental Observation of the Internal Josephson Effect

5.1 Introduction

The manifestation of phase coherence on macroscopic scales is among the most spectacular phenomena occurring in superfluids and superconductors [94]. According to quantum mechanics, only the relative phase between two quantum systems is observable while the phase of a single one is not [95]. If a weak link is created between two quantum fluids, as a small perturbation on the uncoupled systems, a particle current driven by the relative phase oscillates through the junction, providing a non-destructive test of phase coherence. This is at the heart of the eponymous phenomenon predicted by Josephson in the sixties [57], and verified experimentally, up to date, with superconductors and superfluid Helium [56, 58, 59]. In this chapter we discuss the creation of a weak link between two hyperfine levels of ^{87}Rb with a non-resonant electromagnetic field and the observation of an oscillating

Josephson current between them. The response above the critical condensation temperature of ^{87}Rb thermal gases, driven by the same external field, is different: we will show that the thermal oscillations damp quickly with respect to those of the condensate. This evidence gives a clear signature of the BEC's macroscopic phase coherence.

While the Josephson effect was observed in superconducting systems soon after its proposal [56], the search in neutral superfluids has always been problematic owing to the difficulty of creating weak links. Evidences of Josephson oscillations across a micropore connecting two ^{3}He-B baths were reported by Avenel and Varoquoax [58] and their first direct observation has been recently reported by Davis, Packard and collaborators [59]. The weak link was provided by the spatial overlap of the two superfluid wavefunction tails inside the micropore [96]. In the "internal" Josephson effect, on the other hand, the states which are coupled differ by some intrinsic (spin) quantum number, and are not necessarily separated spatially. An example is the longitudinal magnetic resonance in superfluid ^3He-A [97]; in this case the relevant degree of freedom is the hyperfine (nuclear spin) index of a Cooper pair. Oscillations between two coupled ^{87}Rb condensates trapped in different hyperfine levels have been observed by the JILA group [85]. Josephson currents in an array of weakly coupled condensates [8] has been described in Chapter 2.

The key point in experiments in which population oscillations between two coupled levels are observed is to distinguish if they are Josephson or Rabi. We want to remark that this is not a terminological problem: the condition to have Josephson oscillations is the coherence of the two condensates and the fact that each condensate is described by its own *macroscopic* wave function.

The Rabi oscillations are instead *single* particle oscillations, in the sense that each particle oscillate between the two coupled state independently from the others. In other word, the Josephson effect regards with a non-destructive manifestation of phase coherence on a (macroscopic) quantum fluid. The idea is to couple two quantum fluids, and then inquire about their (if any) well definite relative phase, but, and this is the crux, without perturbing the two fluids. Of course, the words "without perturbing" mean that the energy scale of the coupling probe should be small as compared with the chemical potential of both fluids. In the current literature it is common to talk, in this case, of a *weak link*. From the historical point of view, the first weak link achieved was a tunneling barrier between two superconducting systems. Soon after, it was realized that tunneling was just one way among others to create a weak link, and "contact junctions" (with the two superconducting systems sharing a small area) were implemented [56]. The creation of weak links in Helium superfluid systems was technically more difficult, and has been achieved only recently [59]. The junction was provided by a small hole in a membrane which connected two reservoirs of superfluid $He^3 - B$, the diameter of the hole being of the same order of magnitude of the healing length ($\sim 100\ nm$). It is clear and well established, therefore, that tunneling is a sufficient, but not a necessary condition to create a weak link, nor to observe the Josephson effect.

The most important result presented here is the creation, for the first time, of a weak link between two Bose-Einstein condensates, and the direct observation of a Josephson current. The effective creation of a weak link is shown: 1) by a perturbative calculation; 2) by a comparison with the oscillations of the thermal cloud, which quickly damp.

The Rabi effect (RE) is different from the Josephson effect (JE) for two basic reasons. The RE regards the manifestation of coherence between internal states in the single atom dynamics, but does not require coherence among several atoms (indeed it has been observed with thermal, non-condensate, clouds). In this respect the RE is a manifestation of quantum effects on a microscopic (atomic) scale. As expected, the quantum effects are washed out, when reaching the macroscopic scale, by the incoherent collisions and well known dephasing effects between atoms.

The collective coherence of the condensate, on the other hand, is expected to be naturally robust due to the interatomic interaction (in other words, due to the superfluid nature of the condensate emerging from the low energy linear excitation spectrum [54]). Superfluidity is the consequence of phase locking, which preserves the coherent dynamics on a much longer time scale respect to a normal fluid. Therefore, the JE regards the manifestation of quantum effects (the same quantum effects driving the Rabi single atom dynamics) on macroscopic scales. In this section (see below) we include a rigorous proof that we are indeed in the weak-coupling regime.

The second important result is that the condensate oscillation mode persists on a much longer time scale respect to the non-condensate mode. The words "much longer", of course, are not synonymous, in our experimental system, of "several orders of magnitude". This because the thermal cloud is very dilute, and the thermal atoms are weakly interacting; yet, there is a clear difference on the relaxation time scale, that it is possible to read as a clear signature of phase coherence.

5.2 A weak link with two atomic species

In this section we briefly discuss the experimental setup realized at the LENS and we show that the system realizes a weak link. A single condensate in the Zeeman state $|F = 2, m_F = 2 > \equiv |2>$ is created first. Subsequently, we apply a first strong (and, therefore, very short) radiofrequency field to create, out of it, a second condensate in the Zeeman state $|F = 2, m_F = 1 > \equiv |1>$. Both (equally populated) condensates are fully overlapped in space. This gives our initial ($t = 0$) configuration.

Having different magnetic momenta, the atoms of the two species feel different trapping potentials $V_2 = \frac{1}{2} m\omega^2 \{x^2 + l^2(y^2 + z^2)\} + mgz$ and $V_1 = \frac{1}{4} m\omega^2 \{x^2 + l^2(y^2 + z^2)\} + mgz$. Therefore, they begin to separate from each other, each one following its own potential. In Fig.1 we report these potentials along the z-direction, in which the motion of the condensates effectively occurs: the center of two potentials are separated by approximately 15 μm (which is a large amount respect to the width of the condensates, $4.3 \mu m$). While the condensate $|1>$ begins to move, we turn on an external rf field $\hbar \Omega_R e^{i\omega_{rf} t}$ with detuning $\delta = \omega_{rf} - \omega_0$ ($\omega_0 \approx 2\pi \cdot 2MHz$ is the energy shift between the two states) in order to create the weak link. In $\approx 500 \mu s$ the two condensates would get completely separated, but in the typical time scale of our experiment ($\approx 100 \mu s$), they are still almost completely overlapped and the motion of $|1>$ is basically ballistic.

In order to see the Josephson oscillations, an experimental value of Ω_R of, at least, $0.5 kHz$ is necessary. Since the scattering lengths are almost degenerate, the effective mean-field contribution to the chemical potential difference is of the order of $50 Hz$, which is completely negligible in the dynamics.

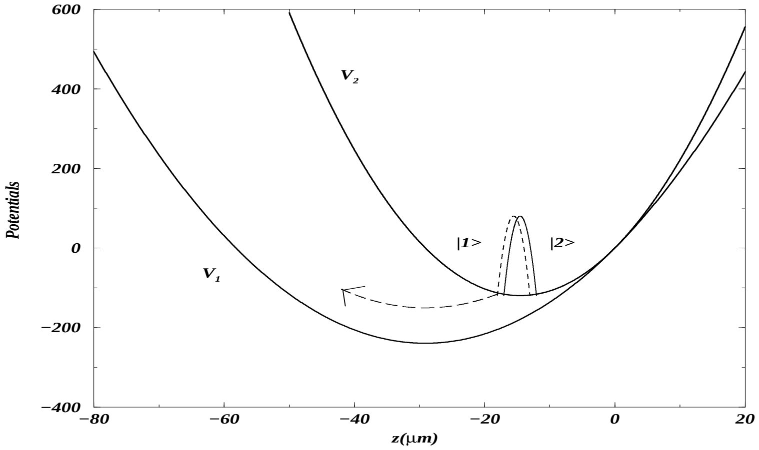

Figure 5.1: Potentials (in unity of $\hbar\omega$) felt by the two condensates along the z-axis, in which the motion effectively occurs. Initially, the two condensates are completely overlapped; the complete oscillations of the condensate $|1>$ around its center have a period of order 10 ms. In the typical time scale of the experiment ($\approx 100\mu$s), $|1>$ moves at most of 0.02 μs and the two condensates remain essentially overlapped.

The order parameters $\psi_j(\vec{r},t)$ for the condensate j ($j=1,2$) obey, in the rotating wave approximation, a set of two-coupled Gross-Pitaevskii equations:

$$i\hbar \begin{pmatrix} \dot{\psi}_2 \\ \dot{\psi}_1 \end{pmatrix} = \begin{pmatrix} \hat{H}_2 - \hbar\delta/2 & \hbar\Omega_R/2 \\ \hbar\Omega_R/2 & \hat{H}_1 + \hbar\delta/2 \end{pmatrix} \begin{pmatrix} \psi_2 \\ \psi_1 \end{pmatrix}. \tag{5.1}$$

If we neglect the mean-field term in the dynamics, as previously discussed, the Hamiltonians of the uncoupled systems (i.e., without the external e.m. field) are $\hat{H}_2 = -\frac{\hbar^2}{2m}\nabla^2 + V_2$ and $\hat{H}_1 = -\frac{\hbar^2}{2m}\nabla^2 + V_1$.

The Eq.(5.1) can be written in the form

$$i\hbar \begin{pmatrix} \dot{\psi}_2 \\ \dot{\psi}_1 \end{pmatrix} = (\hat{H}_0 + \hat{W}_{e.m.}) \begin{pmatrix} \psi_2 \\ \psi_1 \end{pmatrix} \tag{5.2}$$

where

$$\hat{H}_0 = \begin{pmatrix} \hat{H}_2 & 0 \\ 0 & \hat{H}_1 \end{pmatrix} \tag{5.3}$$

is the Hamiltonian of the uncoupled systems.

At $t = 0$, we turn on the coupling e.m. field:

$$\hat{W}_{e.m.} = \frac{\hbar\delta}{2} \begin{pmatrix} -1 & \Omega_R/\delta \\ \Omega_R/\delta & 1 \end{pmatrix}. \tag{5.4}$$

It is possible to see that we have a "weak link" (i.e. a small perturbation on the uncoupled systems) when the ratio $\Omega_R/2\delta$ is small. Indeed, a basis for $\hat{H}_0$ is given by

$$\left\{ \begin{pmatrix} \psi_{2n} \\ 0 \end{pmatrix}, \begin{pmatrix} 0 \\ \psi_{1m} \end{pmatrix} \right\}$$

with $\hat{H}_2\psi_{2n} = E_{2n}\psi_{2n}$ and $\hat{H}_1\psi_{1m} = E_{1m}\psi_{1m}$. Applying the standard first order perturbation theory, we see that the correction to, for instance, the wavefunctions $\begin{pmatrix} \psi_{2n} \\ 0 \end{pmatrix}$ is given by

$$\begin{pmatrix} 0 \\ \sum_m \frac{1}{2} \frac{\Omega_R \int d\vec{r}\psi_{2m}\psi_{1n}}{E_{2m} - E_{1n} + \delta} \psi_{2m} \end{pmatrix} \tag{5.5}$$

from which we can see the standard first order perturbation theory correctly applies when $\Omega_R/2\delta << 1$: in this condition, the external rf field is a weak link. We note that, with $\delta \approx 70kHz$, when the denominator is very small the numerator also vanishes. Similarly, this is valid also for the dynamics.

5.3 Macroscopic quantum oscillations between weakly linked Bose-Einstein condensates

In the previous section we showed that coupling with a far-detuned e.m. field two different levels we create a weak link between them. This weak link has been realized at LENS and the Josephson oscillations observed. In this section we discuss in detail this experiment and we present the data obtained.

The experiment goes as follows: a dilute gas of ^{87}Rb atoms is trapped and cooled below the critical temperature for Bose-Einstein condensation [32], $T_c \simeq 130\, nK$, with a combination of laser and evaporative cooling. The atoms are confined by dc magnetic fields generated by a set of four coils, arranged so as to create an axially symmetric harmonic potential [91]. We prepare the Bose-Einstein condensate initially in the $|F = 2, m_F = 2 >\equiv |2>$ Zeeman state. A first resonant rf field is applied to transfer half of the condensate population into the $|F = 2, m_F = 1 >\equiv |1>$ state (there is a small transfer of population into the other three accessible Zeeman levels that can be neglected in the dynamics of the system). The two condensates, having different magnetic momenta, experience the different trapping potentials V_2 and V_1, whose centers z_2 and z_1 are separated by approximately 15 μm (while the width of the condensates is ≈ 4.3 μm). At the end of the first pulse, the two condensates are equally populated and completely overlapped (their position is given by z_2). Now, a new rf far-detuned field is applied: the relative population between the two levels oscillates and its time evolution is recorded by a series of destructive measurements. During the far-detuned pulse, the condensates begin to separate: $|1>$ goes towards the center of its potential,

z_1, initially following a ballistic motion; in the typical time scale of the experiment it moves apart along the vertical z-axis at most by 0.02 μm. The two condensates then remain essentially overlapped and with no change in shape.

In the far-detuned regime ($\delta \gg \Omega_R$), the external field is a weak link. Therefore, the condensates dynamics can be described in the two-mode approximation [35, 36, 90, 98] and the two wavefunctions can be parameterized (in the center of mass frame) as $\psi_j(\vec{r};t) = \sqrt{N_j(t)}e^{i\phi_j(t)}\,\Phi(\vec{r})e^{\frac{i}{\hbar}p_j(t)\cdot z}$ ($j = 1, 2$, $\int d\vec{r}|\psi_j|^2 = N_j$, p_j is the condensate momentum and $\Phi(\vec{r})$ the $|2, 2>$ wavefunction at $t = 0$). The temporal evolution of $\Phi(\vec{r})$ can be neglected. The equations of motion for the particle number N_j and its conjugate momentum ϕ_j, can be retrieved from the two coupled Gross-Pitaevskii equations describing the system and discussed in the previous section. The current-phase dynamics is given by:

$$\begin{cases} I(t) = I_c(t)\sqrt{1-\eta^2(t)}\sin\phi(t) \\ \frac{\partial}{\partial t}\phi = -\Delta\mu(\phi,\eta) \end{cases} \tag{5.6}$$

with $\eta = \frac{N_2-N_1}{N_2+N_1}$, $I_c(t) = \Omega_R \int d\vec{r}\Phi(\vec{r})\Phi(\vec{r})e^{ip(t)z/\hbar}$, $p = p_1 - p_2$ and, in the far-detuned case, the chemical potential difference $\Delta\mu = \mu_1 - \mu_2 \simeq \delta$. We remark that the atomic current $I = \frac{\partial}{\partial t}\eta$ depends on the relative average phase $\phi(t) = \phi_1(t) - \phi_2(t)$. In the strong-coupling limit ($\delta < \Omega_R$), the two-mode approximation breaks down, and hence Eqs.(5.6) cannot be retrieved. We observe that the scattering lengths of the two condensates are almost degenerate, and that the mean-field term in Eqs.(5.6) is of the order of 50 Hz so it can be neglected.

Eqs.(5.6) are generalized Josephson equations, similar to those governing a voltage-driven superconducting junction [56]. Here, however, the critical current $I_c(t)$ depends explicitly on time due to the dynamical phase, $e^{\frac{i}{\hbar}p(t)z}$, accumulated by the two condensates. The spin dynamics can be decoupled from the much slower spatial dynamics so, to a good approximation, $p \simeq -mgt/2$. This gives a decreasing critical current $I_c(t) \approx \Omega_R \, e^{-t^2/\Gamma^2}$ with a relaxation time $\Gamma \simeq \; 132\mu$s. A further departure from the standard Josephson current relation is given by the term $\sqrt{1-\eta^2}$ [35, 36], absent in superconducting systems where $\eta \approx 0$ [56] due to the presence of external circuits which suppress charge imbalances. In Fig.2a the time evolution of the fractional relative population observed experimentally is compared with the solution of the Josephson Eqs.(5.6).

In order to highlight the macroscopic quantum nature of the condensate oscillations, we show that those of a non-condensate (thermal) atomic cloud, driven by the same external rf field, die out on a much shorter time scale. The difference between the two relaxation times is a manifestation of the BEC long-range order respect to the microscopic coherence length of the non-condensate cloud. Indeed, the relaxation of the condensate oscillation is purely dynamical (due to the different trapping potentials felt by the two Zeeman states), while the decay of the thermal gas is mainly due to a strong dephasing. In our experiment, a thermal atomic cloud is initially trapped in the Zeeman level $|2>$, at a temperature $T \simeq 3 \; T_c$. In first approximation, the gas is very dilute and can be seen as a swarm of non-interacting particles. After the first $\pi/2$ pulse, the far-detuned rf field is applied, and the atomic population recorded. The oscillations die out in $\sim 40\mu$s (see Fig.2b), which should be compared with the $\sim 200\mu$s in which the condensate oscillations disappear. If we describe the thermal cloud by the density matrix $\rho = \sum_\alpha \rho^{(\alpha)} = \sum_\alpha |\psi^{(\alpha)} >< \psi^{(\alpha)}|$, where α runs over the number of particles and $< \psi^{(\alpha)}| = \Big(\sum_n a_n^{(\alpha)*} e^{-ip_1 z/\hbar} < \varphi_n| \ , \ \sum_m b_m^{(\alpha)*} e^{-ip_2 z/\hbar} < \varphi_m| \Big)$. the dynamical evolution of the density matrix is given by

$$\begin{cases} i\dot{a}_n^{(\alpha)} = (\epsilon_n - \frac{\delta}{2}) a_n^{(\alpha)} + \frac{1}{2} \sum_m \Omega_{nm}(t) b_m^{(\alpha)} \\ i\dot{b}_n^{(\alpha)} = (\epsilon_n - \frac{\delta}{2}) b_n^{(\alpha)} + \frac{1}{2} \sum_m \Omega^*_{mn}(t) a_m^{(\alpha)} \end{cases} \tag{5.7}$$

The transfer matrix elements are calculated as overlap integrals of the two-species wave-functions $\Omega_{nm}(t) = \Omega_R \int d\vec{r} \varphi_n(\vec{r}) \varphi_m(\vec{r}) e^{ip(t)z/\hbar}$. The orthogonality of the wavefunctions is gradually lost so, after a transient time, the diagonal and non-diagonal matrix elements become comparable, allowing for an incoherent exchange between states of different quantum numbers and, therefore, leading to a strong dephasing of the thermal oscillations. From our simulations $\Omega_{n,n} \sim \Omega_{n,n\pm1}$ at $t \sim 30$ μs.

We observe that, if the two trapping potentials were the same, all diagonal matrix elements in Eqs.(5.7) would be equal to $\Omega_{nn} = \Omega_R$, while the off-diagonal terms would vanish $\Omega_{nm} = 0$. Therefore the thermal cloud would exhibit undamped Rabi oscillations [99], indistinguishable from the condensate Josephson oscillations. In Fig.2b we show the time evolution of the relative population of the two thermal clouds, which is in fairly good agreement with our predictions.

The theoretical and experimental results here reported allow us to conclude that 1) the far-detuned rf field behaves like a superfluid weak link, 2) the current-phase dynamics is governed by generalized Josephson equations, 3) the persistence of condensate oscillations for times much longer than those of the thermal cloud yields a clear signature of the macroscopic quantum coherence in Bose-Einstein condensates.

Our experimental set-up would also enable one to study the analogous of several phenomena present in superconducting and superfluid Josephson junctions [55], as well as to address problems in the foundation of quantum mechanics, like the possibility to define a phase standard [95]. This might be investigated populating all the Zeeman sublevels, thus creating an array of Josephson junctions, whose relative phases can be properly manipulated by tuning the external rf field. Furthermore, the comparison between the condensate and normal components of an atomic gas opens a new experimental way to testing theories of decoherence and dephasing mechanisms [54,98,100] by studying the Josephson dynamics of a condensate embedded in a thermal bath.

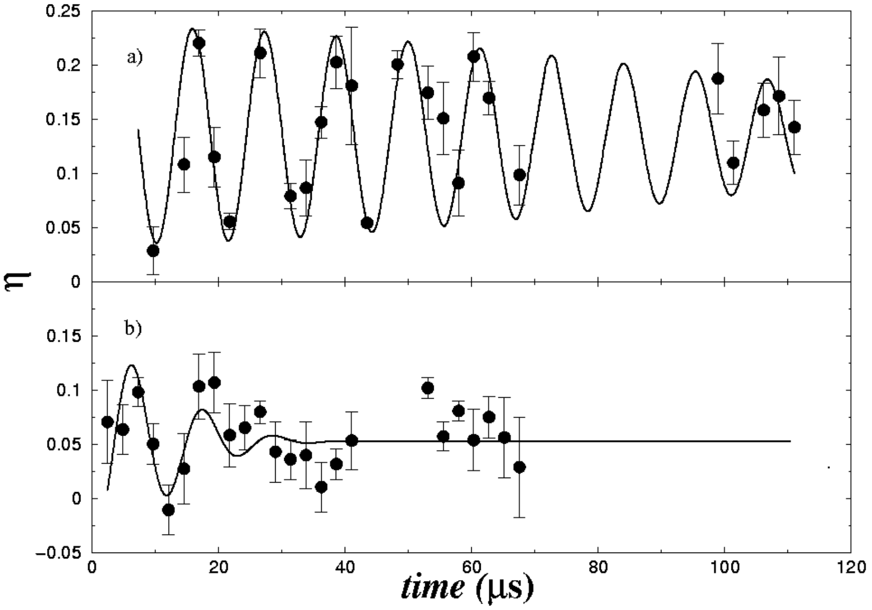

Figure 5.2: a) Time evolution of the fractional relative population of the two condensates, $\eta = (N_2 - N_1)/(N_2 + N_1)$. The experimental data (dots) are compared with the theoretical prediction (solid line) as described in the text. $\Omega_R = 2\pi \times (13 \pm 2) kHz$ and $\delta = 2\pi \times (80 \pm 10) kHz$. At the end of the second pulse the trap is turned off, and the population of both condensates is destructively measured with laser imaging techniques. The frequency of the oscillations is $\nu = 88\ kHz$, and the relaxation time is $\Gamma \simeq 130\ \mu s$. b) Time evolution of the fractional relative population of the thermal clouds $\eta = (N_2 - N_1)/(N_2 + N_1)$. The temperature is $T \simeq 0.4\ \mu K\ \simeq 3T_c$. The parameters are the same as in Fig.2a. The theoretical frequency of the oscillations is $\nu = 88\ kHz$, as for the condensate oscillations, while the relaxation time is $\Gamma \simeq 15\ \mu$s, which has to be compared with the value (130μs) for the condensate.

Appendix A

Variational dynamics of arrays of Bose-Einstein condensates

A.1 Lagrangian

The wave packet dynamical evolution for a BEC in an optical lattice can be obtained by a variational principle from the Lagrangian

$$\mathcal{L} = \sum_{n=-\infty}^{\infty} i\dot{\psi}_n \psi_n^* - \mathcal{H}, \tag{A.1}$$

with the equations of motion for the variational parameters $q_i(t) = \xi, \alpha, p, \delta$ given by

$$\frac{d}{dt}\frac{\partial \mathcal{L}}{\partial \dot{q}_i} = \frac{\partial \mathcal{L}}{\partial q_i}. \tag{A.2}$$

Substituting the variational ansatz (1.13) $\psi_V^n(t) = \sqrt{k} \cdot \exp\Big\{ -\frac{(n-\xi)^2}{\alpha} + ip(n-\xi) + i\frac{\delta}{2}(n-\xi)^2 \Big\}$ in (A.1), we obtain

$$\mathcal{L} = k \sum_{n=-\infty}^{\infty} e^{-(2n^2+2n-4n\xi+2\xi^2-2\xi+1)/\alpha} \cos\left[\delta(n+1/2-\xi)+p\right] +$$

$$+k\sum_{n=-\infty}^{\infty}\big\{-\frac{\dot\delta}{2}(n-\xi)^2+\delta\dot\xi(n-\xi)-\dot p(n-\xi)+p\dot\xi\big\}\,e^{-2(n-\xi)^2/\alpha}+$$

$$-k\sum_{n=-\infty}^{\infty}E_n e^{-2(n-\xi)^2/\alpha}-\frac{\Lambda}{2}k^2\sum_{n=-\infty}^{\infty}e^{-4(n-\xi)^2/\alpha}. \tag{A.3}$$

With α not too small ($\alpha > 1$), we can replace the sums over n with integrals: to evaluate the error committed, we recall that [101]

$$\sum_{n=-\infty}^{\infty}e^{-\frac{(n-\xi)^2}{\alpha}}\Bigg/\int_{-\infty}^{\infty}e^{-\frac{(n-\xi)^2}{\alpha}}dn=1+O(e^{-\pi^2\alpha}). \tag{A.4}$$

In this limit the normalization factor becomes $k=\sqrt{2/\pi\alpha}$. We finally get

$$\mathcal{L}=p\dot\xi-\frac{\alpha\dot\delta}{8}-\frac{\Lambda}{2\sqrt{\pi\alpha}}+\cos p\,\cdot\,e^{-\eta}-V(\alpha,\xi) \tag{A.5}$$

where $V=k\int_{-\infty}^{\infty}dn\,E_n e^{-\frac{2(n-\xi)^2}{\alpha}}$ and $\eta=\frac{1}{2\alpha}+\frac{\alpha\delta^2}{8}$. Also it is possible to show explicitly that $Im\mathcal{L}=0$, as might. Using the Euler-Lagrange equations (A.2), Eqs.(1.14) and (1.15) are obtained.

A.2 Phase diagrams for the horizontal array

In this case, the on-site energies E_n, as well as $V(\xi,\alpha)$, are constant. The momentum is, therefore, conserved: $p(t)=p(t=0)\equiv p_0$. We will consider the case $\Lambda>0$, in order to make contact with the experiments done with ^{87}Rb, as discussed in chapter 1. The phase diagrams for the collective coordinates which describe the boson wave packet can be determined from the Eq.(1.14)- (1.18) in the following way [34]. Let us suppose $\cos p_0>0$ (i.e. a positive effective mass) and initial values α_0 and $\delta_0=0$. The initial value of the Hamiltonian is given by $H_0=\Lambda/2\sqrt{\pi\alpha_0}-\cos p_0\cdot e^{-1/2\alpha_0}$. Since the

Hamiltonian (1.18) is a conserved quantity, we have $H_0 = \Lambda/2\sqrt{\pi\alpha} - \cos p_0 \cdot e^{-1/2\alpha - \alpha\delta^2/8}$: therefore

$$\frac{\Lambda}{2\sqrt{\pi\alpha}} - H_0 > 0. \tag{A.6}$$

The trajectories in the $\alpha - \delta$ plane are given by

$$\delta^2 = -\frac{8\alpha \log\left(\frac{\Lambda/2\sqrt{\pi\alpha} - H_0}{\cos p_0}\right) + 4}{\alpha^2} \tag{A.7}$$

From (A.6), we can see that when $H_0 > 0$, the width α_0 has to remain finite and that $\alpha < \alpha_{max}$, where the maximum value of the width is

$$\alpha_{max} = \frac{\Lambda^2}{4\pi H_0^2}. \tag{A.8}$$

Using Eqs.(A.7), we can see that $\delta \to \infty$ for $t \to \infty$; therefore for large t $\dot{\xi} \approx \sin p_0 e^{-1/2\alpha_{max} - \alpha_{max}\delta^2/8} \to 0$ and $1/m^* \approx \cos p_0 e^{-1/2\alpha_{max} - \alpha_{max}\delta^2/8} \to 0$. The center of the BEC wave packet stops and the effective mass goes to infinity: there is an energy transfer from the kinetic energy to the internal modes, since δ is the momentum associated to the width α.

When $H_0 < 0$, on the other hand, we have for $t \to \infty$ that $\alpha \to \infty$ and $\delta^2 \approx -8 \log(-H_0/\cos p_0)/\alpha \to 0$. The center of mass does not stop since $\dot{\xi} \approx -H_0/\tan p_0 \neq 0$ and the effective mass is given by $1/m^* \approx -H_0 > 0$. This regime is a diffusive one, with an asymptotic complete spreading of the wave function.

The transition between these two regimes is given by $H_0 = 0$: the critical value for the nonlinearity is

$$\Lambda_c = 2\cos p_0 \sqrt{\pi\alpha_0}\, e^{-1/2\alpha_0}. \tag{A.9}$$

For large times, when $\Lambda > \Lambda_c$, $\alpha \to \alpha_{max}$ and $\dot{\xi} \to 0$ (*self-trapping*); for $\Lambda < \Lambda_c$, $\alpha \to \infty$ and $\dot{\xi} \to$ *const* (*diffusion*). In Fig.A1 we plot the critical value vs. the initial width: we observe that the greater the initial width, the greater is the critical value of the nonlinearity in order to have self-trapping and localization. Furthermore, we observe that using Eqs.(A.8) we get

$$\frac{\alpha_{max}}{\alpha_0} = \left(\frac{\Lambda}{\Lambda - \Lambda_c}\right)^2 : \tag{A.10}$$

from which we can see that at Λ_c the width goes to ∞. Moreover, from (A.10) we can argue that $\alpha_{max} > \alpha_0$. This is illustrated in Fig.2, where we plot the trajectories in the space $\alpha - \delta$ for different values of Λ. In Fig.3 we plot the inverse of the effective mass (1.21): it is seen that for $\Lambda > \Lambda_c$, $1/m^* \to 0$.

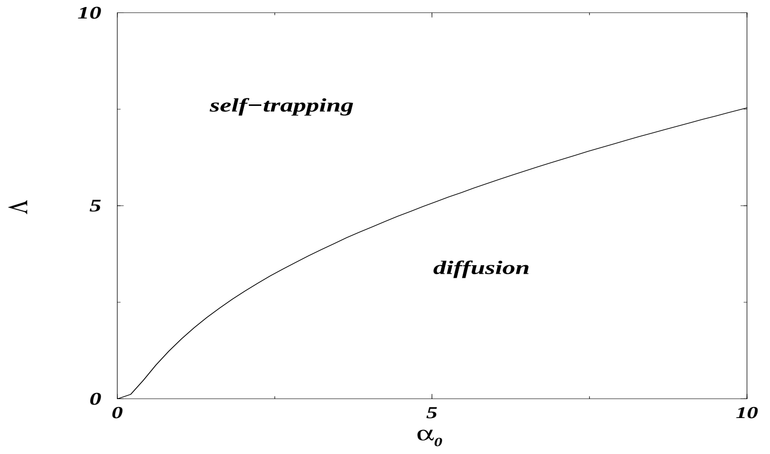

Figure A.1: Plot of the critical value Λ_c vs. the initial wave packet width α_0 in the case $\cos p_0 > 0$ ($p_0 = \pi/4$).

The phase diagram, as we discussed, is richer in the case $\cos p_0 < 0$ (i.e. when the effective mass is negative). Indeed, for $\cos p_0 > 0$ the Eqs.(1.15) do not admit fixed points $\dot{\alpha} = 0$ and $\dot{\delta} = 0$; while, with $\cos p_0 < 0$, Eqs.(1.15) have the stationary solution $\alpha(t) = \alpha_0$ and $\delta(t) = 0$ when the nonlinear coefficient is equal to

$$\Lambda_{sol} = 2 \mid \cos p_0 \mid \sqrt{\frac{\pi}{\alpha_0}}\, e^{-1/2\alpha_0}. \tag{A.11}$$

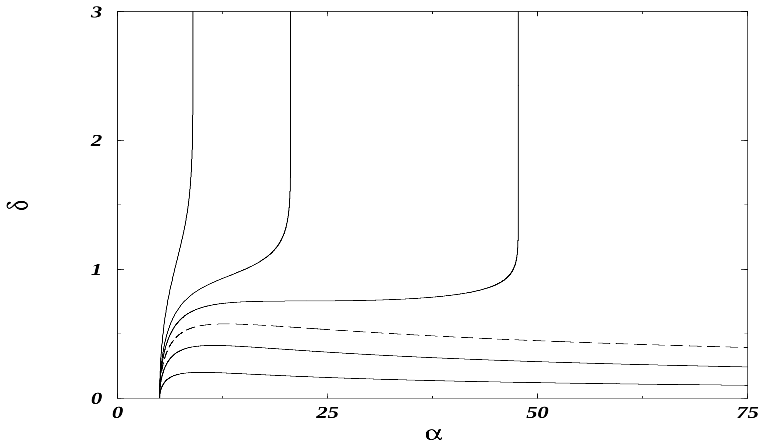

Figure A.2: Trajectories in the space $\alpha - \delta$ for different values of Λ in the case $\cos p_0 > 0$. The initial values of the width and the momentum are respectively $\alpha_0 = 5$ and $p_0 = \pi/4$: the critical value is $\Lambda_c = 5.072$. Beginning from the bottom of the figure it is $\Lambda = 0, 2.5, \Lambda_c$(dashed line)$, 7.5, 10, 20$.

For $\Lambda = \Lambda_{sol}$ the center of mass moves with constant velocity $\dot{\xi} = \sin p_0 \, e^{-1/2\alpha_0}$ and the gaussian shape does not change with time - a bright soliton. The soliton solution is a maximum of the energy (1.18): indeed, if we fix Λ, from $(\partial H/\partial\alpha)_{\delta=0} = 0$ we find the corresponding width α_{sol} of the stationary solution. The relation, between Λ and α_{sol} is given by $\Lambda = 2 \mid \cos p_0 \mid \sqrt{\frac{\pi}{\alpha_{sol}}} \, e^{-1/2\alpha_{sol}}$. Using this relation it is possible to show that $(\partial^2 H/\partial\alpha^2)_{\delta=0,\alpha=\alpha_{sol}} = -\cos p_0 e^{-1/2\alpha_{sol}}(1-\alpha_{sol})/4\alpha_{sol}^4 < 0$ for $\alpha = \alpha_{sol}$ (we recall that the approximation (A.4) requires α greater than 1).

Furthermore, proceeding as in the case $\cos p_0 > 0$, we observe that $H_0 = \Lambda/2\sqrt{\pi\alpha_0} + \mid \cos p_0 \mid e^{-1/2\alpha_0} > 0$ and $\Lambda/2\sqrt{\pi\alpha} = H_0 - \mid \cos p_0 \mid e^{-\eta}$. Therefore, for $H_0 > \mid \cos p_0 \mid$, the width α has to remain finite. For $H_0 < \mid \cos p_0 \mid$, $\alpha \to \infty$, $\delta^2 \approx -8 \log{(H_0/\mid \cos p_0 \mid)}/\alpha \to 0$ and $\dot{\xi} \to -H_0/\tan p_0 \neq 0$. The

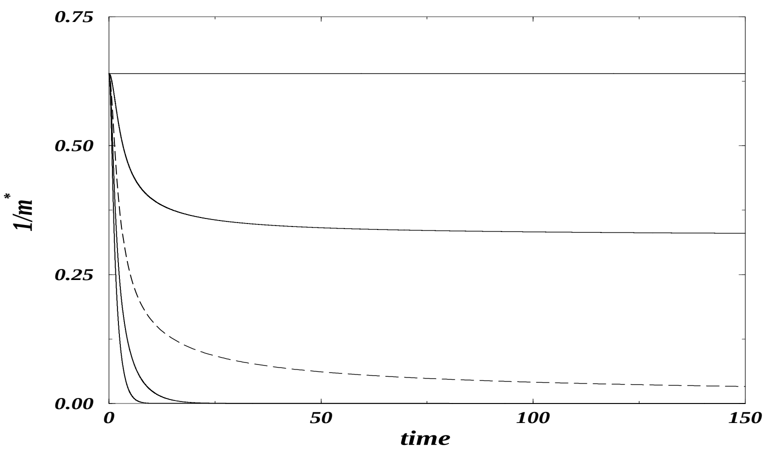

Figure A.3: Inverse of the effective mass vs. time for different values of Λ ($\alpha_0 = 5$ and $p_0 = \pi/4$ as in Fig.2): from the top of the figure it is $\Lambda = 0, 2.5, \Lambda_c(\text{dashed line}), 7.5, 10$.

transition occurs at

$$\Lambda_c = 2 \mid \cos p_0 \mid \sqrt{\pi\alpha_0}\,(1 - e^{-1/2\alpha_0}). \qquad \text{(A.12)}$$

We observe that for $\alpha_0 > 1$, $\Lambda_{sol} > \Lambda_c$.

For $\Lambda > \Lambda_c$ we have $\alpha(t)$ finite: but, while in the case $\cos p_0 > 0$, we have $\alpha \to \alpha_{max} > \alpha_0$ and $\delta \to \infty$, now the situation is different. For $\Lambda_c < \Lambda < \Lambda_{sol}$, we have $\alpha(t)$, $\delta(t)$ and the effective mass (1.21) oscillating with time: the trajectories in the $\alpha - \delta$ plane are closed and α oscillates between the initial value α_0 and a value $\alpha_{osc}^{max} > \alpha_0$. When Λ approach to Λ_{sol}, the area enclosed in the trajectories shrinks to 0 at the stationary point. In this region $\Lambda_c < \Lambda < \Lambda_{sol}$, $\dot{\xi}$ oscillates around a constant value: we have a *breather* solution, with the center of mass traveling with a nearly constant velocity and with an oscillating width. The breather region extends until the value Λ_{breath}: for $\Lambda_{sol} < \Lambda < \Lambda_{breath}$, α oscillates between the initial value α_0 and a value $\alpha_{osc}^{min} < \alpha_0$. Both the values $\alpha_{osc}^{max,min}$ are roots (together with α_0) of the Eq.(A.7). The condition for which Eq.(A.7) does not have another root $\alpha_{osc}^{min} < \alpha_0$ (apart from α_0) gives Λ_{breath}.

The determination of Λ_{breath} goes as follows. When $\Lambda_{sol} < \Lambda < \Lambda_{breath}$, the point $(\alpha = \alpha_{osc}^{min} < \alpha_0, \delta = 0)$ is determined by using the energy conservation:

$$H_0 = \frac{\Lambda}{2\sqrt{\pi \alpha_{osc}^{min}}} - \cos p_0 \cdot e^{-1/2\alpha_{osc}^{min}}$$

(this equation is satisfied, of course, also by α_0). With the position $\alpha_{osc}^{min} \equiv x\alpha_0$, with $x < 1$, we can find

$$\frac{\Lambda}{\Lambda_{sol}} = \frac{\alpha_0 \sqrt{x}}{1 - \sqrt{x}} \cdot \left(1 - e^{(x-1)/2\alpha_0 x}\right) \tag{A.13}$$

From this it is possible to see that when $x \to 1$, then $\Lambda \to \Lambda_{sol}$, as expected. Moreover, with $\alpha_0 < 1$, the value of Λ/Λ_{sol} from Eq.(A.13) is never greater than 1: this means that above Λ_{sol} there are not anymore breather solution. In the more interesting case $\alpha_0 > 1$, the maximum value of the rhs of Eq.(A.13) gives $\Lambda_{breath}/\Lambda_{sol}$. This value is always greater than 1, it depends on α_0 and not on p_0. The full phase diagram for $\cos p_0 < 0$, including Λ_c, Λ_{sol} and Λ_{breath} is reported in Fig.4.

For $\Lambda > \Lambda_{breath}$, moreover, $\alpha \to \alpha_{min} < \alpha_0$, $\delta \to \infty$ and $\dot{\xi} \to 0$, with a self-trapping of the wave-packet. The value of α_{min} is given by

$$\alpha_{min} = \alpha_0 \left(\frac{\Lambda}{\Lambda + \tilde{\Lambda}} \right)^2 . \tag{A.14}$$

where $\tilde{\Lambda} = 2\sqrt{\pi\alpha_0} \mid \cos p_0 \mid e^{-1/2\alpha_0}$. Eq.(A.14) is the generalization of the relation (A.10) to the case of $\cos p_0 < 0$ and it shows that for $\Lambda \to \infty$ it is $\alpha_{min} \to \alpha_0$: a large nonlinearity forbids any spreading of the wave packet. In Fig.5 we plot the $\alpha - \delta$ trajectories for different values of Λ: in the inset of Fig.5 we illustrate the transition at Λ_{breath}. In Fig.6 we plot the behaviour of the effective mass.

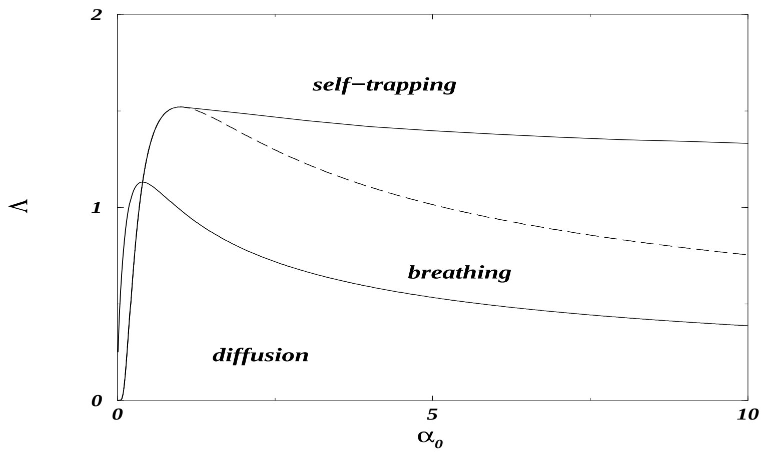

Figure A.4: Phase diagram in the case $\cos p_0 < 0$ ($p_0 = 3\pi/4$). The dashed line is the solitonic solution and the two solid line are, beginning from the bottom of the figure, Λ_c and Λ_{breath}: $\Lambda_c < \Lambda < \Lambda_{breath}$ defines the breather region.

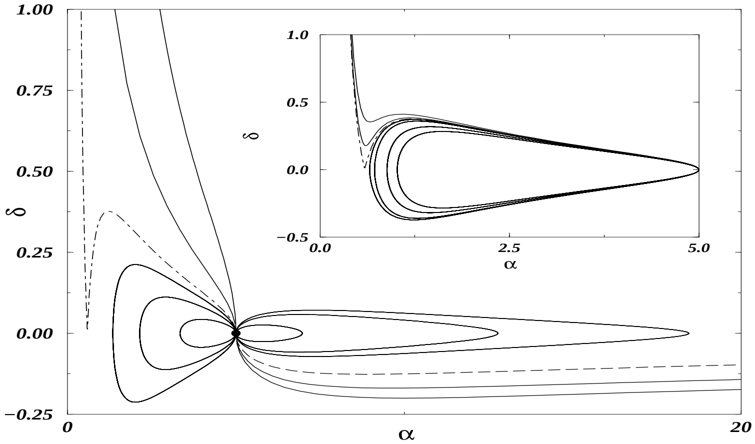

Figure A.5: Trajectories in the space $\alpha - \delta$ for different values of Λ in the case $\cos p_0 < 0$. The initial values of the width and the momentum are respectively $\alpha_0 = 5$ and $p_0 = 3\pi/4$: the critical values for the different transitions are $\Lambda_c = 0.534$, $\Lambda_{sol} = 1.014$ and $\Lambda_{breath} = 1.397$. For $\Lambda_c < \Lambda < \Lambda_{breath}$ the trajectories are closed. Beginning from the bottom of the figure it is $\Lambda = 0, 0.25, \Lambda_c$(dashed line)$, 0.8, 0.85, 0.95, \Lambda_{sol}$ (black circle)$, 1.1, 1.2, 1.3, \Lambda_{breath}$(dot-dashed line)$, 2, 5$. In the inset we show the phase trajectories $\alpha - \delta$ near Λ_{breath}: the different values from the left are $\Lambda = 1.35, 1.37, 1.39, \Lambda_{breath}$(dot-dashed line)$, 1.4, 1.41$.

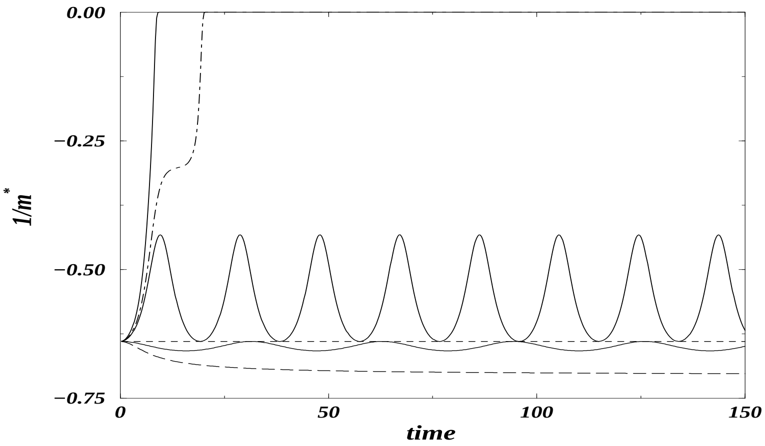

Figure A.6: Inverse of the effective mass vs. time for different values of Λ ($\alpha_0 = 5$ and $p_0 = 3\pi/4$ as in Fig.5): from the bottom of the figure it is $\Lambda = \Lambda_c$(dashed line), $0.95, \Lambda_{sol}$ (dotted line),1.35, Λ_{breath}(dot-dashed line), 1.5. For $\Lambda < \Lambda_c$, the effective mass goes to a constant value, for $\Lambda_c < \Lambda < \Lambda_{breath}$ it oscillates and for $\Lambda > \Lambda_{breath}$ goes to 0 (furthermore for $\Lambda = \Lambda_{sol}$ it is constant).

Appendix B

Variational estimate of the coefficients of the discrete nonlinear Schrödinger equation

In this Appendix we report a variational calculation of the coefficients K, U and ϵ_n of the DNLSE: we remember that $K = -\int d\vec{r} \left[\frac{\hbar^2}{2m}\vec{\nabla}\Phi_n \cdot \vec{\nabla}\Phi_{n+1} + \Phi_n V_{ext} \Phi_{n+1}\right]$, $U = g_0 N_T \int d\vec{r}\, \Phi_n^4$ and $\epsilon_n = \int d\vec{r} \left[\frac{\hbar^2}{2m}(\vec{\nabla}\Phi_n)^2 + V_{ext}\Phi_n^2\right]$ with the external potential given by Eq.(2.4). We use the variational ansatz given in section 1.4:

$$\Phi_n(\vec{r}) = C e^{-(x-x_n)^2/2\sigma_x^2} e^{-y^2/2\sigma_y^2} e^{-z^2/2\sigma_z^2} \tag{B.1}$$

with C normalization factor, $x_n = n\lambda/2$ center of the n-th well along the optical trap and $\sigma_{x,y,z}$ widths to determine We will take $\sigma_x = \sigma_y \equiv R$ from the experimental data: $R \approx 5.6\mu m$. As we discussed in the main text, we are neglecting the site-dependence the width and we take rather an average value. From $\int d\vec{r}\Phi_n^2 = 1$ we get $C = (\pi^{3/2}R^2\sigma_x)^{-1/2}$. Since

$$\int d\vec{r}\Phi_n^2 \cdot \frac{1}{2}m[\omega_x^2 x^2 + \omega_r^2(y^2+z^2)] = \frac{1}{2}m\omega_x^2(x_n^2 + \frac{\sigma_x^2}{2}) + \frac{1}{2}m\omega_r^2 R^2,$$

neglecting constant terms in the energy, the formula (2.9) is obtained. Furthermore we get

$$U = \frac{g_0 N_T}{(2\pi)^{3/2}R^2\sigma_x} \tag{B.2}$$

and

$$K = -e^{-\lambda^2/16\sigma_x^2}\left\{\frac{\hbar^2}{2mR^2} + \frac{\hbar^2}{2m\sigma_x^4}\Big(\frac{\sigma_x^2}{2} - \frac{\lambda^2}{16}\Big) + \frac{V_0}{2}(1+e^{-4\pi^2\sigma_x^2/\lambda^2})\right\}. \tag{B.3}$$

Now we have to determine the σ_x: for simplicity, let us introduce the adimensional quantities

$$\alpha = \frac{V_0}{E_R}$$

(E_R energy recoil) and

$$x = \frac{\sigma_x}{\lambda}.$$

The conserved energy of the GPE is

$$E[\Psi] = \int d\vec{r}\,\Big[\frac{\hbar^2}{2m}(\vec{\nabla}\Psi)^2 + V_{ext} \mid \Psi \mid^2 + \frac{g_0}{2} \mid \Psi \mid^4 \Big] :$$

when we use the tight-binding approximation, $\Psi(\vec{r},t) = \sqrt{N_T}\sum_j \psi_j(t)\Phi_j(\vec{r})$, the energy in the i-th well is

$$E[\psi_i\Phi_i]/N_T \approx \int d\vec{r}\,\Big[\frac{\hbar^2}{2m}(\vec{\nabla}\psi_i\Phi_i)^2 + V_{ext} \mid \psi_i \mid^2 \Phi_i^2 + \frac{g_0 N_T}{2} \mid \psi_i \mid^4 \Phi_i^4\Big] :$$

by using $\mid \psi_i \mid^2 \approx \frac{N_i}{N_T}$, where N_i is the average value of particle per site, we get an expression for the energy in the i-th well given by

$$E[\sigma_x] \approx N_i\frac{\hbar^2}{4m\sigma_x^2} + N_i^2\frac{g_0}{2(2\pi)^{3/2}R^2\sigma_x} + N_i\frac{V_0 k^2\sigma_x^2}{2} + N_i\frac{m\sigma_x^2}{4}(\omega_x^2 + 2\omega_r^2).$$

From $\frac{\partial E}{\partial \sigma_x} = 0$ we get σ_x: using the numerical values, we see that there is a very weak dependence on the mean field term, and therefore to number of particles in each site. Furthermore the laser term $\propto V_0$ is much greater of the "harmonic" term $\propto (\omega_x^2 + 2\omega_r^2)$. Finally we obtain

$$x^4 \approx \frac{\hbar^2}{2mV_0k^2\lambda^4} = \frac{1}{(k\lambda)^4\alpha}$$

from which

$$x \approx \frac{1}{2\pi}\alpha^{-1/4}.$$

We see that the variational width depends on the strength of the laser: finally it is

$$K/E_R \approx \frac{1}{4\pi^2x^4}\left(\frac{1}{16} - \frac{x^2}{2}\right)e^{-1/16x^2} - \frac{\alpha}{2}(1 + e^{-4\pi^2x^2})e^{-1/16x^2}$$

and

$$U = \frac{g_0 N_T}{(2\pi)^{3/2}R^2\lambda x}.$$

Appendix C

Effective Lagrangian for the Josephson oscillations in presence of the internal modes

The system of two Zeeman level coupled by an e.m field is described, in the rotating-wave approximation, by two coupled GPE: being $\psi_{1,2}(\vec{r},t)$ the order parameters of the two condensates, they read

$$i\begin{pmatrix}\dot{\psi}_1\\ \dot{\psi}_2\end{pmatrix}=$$

$$=\begin{pmatrix}-\frac{1}{2}\nabla^2+V_1+\lambda_{11}\mid\psi_1\mid^2+\lambda_{12}\mid\psi_2\mid^2 & -\Omega_0\\ -\Omega_0 & -\frac{1}{2}\nabla^2+V_2+\lambda_{21}\mid\psi_1\mid^2+\lambda_{22}\mid\psi_2\mid^2\end{pmatrix}\begin{pmatrix}\psi_1\\ \psi_2\end{pmatrix} \tag{C.1}$$

with $\Omega_0=\Omega_R/2$, $\lambda_{ij}=4\pi a_{ij}/z_{sho}$ and a_{ij} scattering length between the species i and j (furthermore $g_{12}=g_{21}$). The position in expressed in units of $z_{sho}=\sqrt{\hbar/m\omega_{z1}}$, time in units of $1/\omega_{z1}$ and energy in units of $\hbar\omega_{z1}$. The total number of particles is conserved: $\int d\vec{r}(\mid \psi_1 \mid^2 + \mid \psi_2 \mid^2) = N_T$. When the motion is almost one-dimensional along the z-axis, we can substitute to a good approximation $\psi_j(\vec{r},t) \approx \psi(z,t)X_j(x)Y_j(y)$ in the previous (scaled) GPE. In such way we find Eq.(4.2) with $u_{ij} = \lambda_{ij}\int dx X_i^2 X_j^2 \int dy Y_i^2 Y_j^2$.

Substituting (4.6) in (4.5) we find the effective Lagrangian

$$\mathcal{L} = -N_1\dot{\phi}_1 - N_2\dot{\phi}_2 + N_1 p_1 \dot{z}_1 + N_2 p_2 \dot{z}_2 - \frac{1}{8}N_1\alpha_1\dot{\delta}_1 - \frac{1}{8}N_2\alpha_2\dot{\delta}_2 - \mathcal{E} \quad \text{(C.2)}$$

The explicit expressions for the different parts of the energy

$$\mathcal{E} = \mathcal{E}_{MF} + \mathcal{E}_{kin} + \mathcal{E}_{pot} + \mathcal{E}_{Jos} \quad \text{(C.3)}$$

are: the kinetical energy

$$\mathcal{E}_{kin} = \frac{N_1}{2}\left(p_1^2 + \frac{1}{\alpha_1} + \frac{\alpha_1\delta_1^2}{4}\right) + \frac{N_2}{2}\left(p_2^2 + \frac{1}{\alpha_2} + \frac{\alpha_2\delta_2^2}{4}\right),$$

the potential energy (written for (J) e.g.)

$$\mathcal{E}_{pot} =< V_1 > + < V_2 >= \frac{N_1}{2}\left[\frac{\alpha_1}{4} + (z_1+z_0)^2 + \delta\right] + \frac{N_2}{2}\left[\frac{\alpha_2}{4} + (z_2-z_0)^2 - \delta\right]$$

(where $< V_j >= \int dz V_j \mid \psi_j \mid$), the mean-field energy

$$\mathcal{E}_{MF} = \frac{uN_1^2}{2\sqrt{\pi\alpha_1}} + \frac{uN_2^2}{2\sqrt{\pi\alpha_2}} + \sqrt{\frac{2}{\pi}}\frac{uN_1N_2}{\sqrt{\alpha_1+\alpha_2}}e^{-2(z_1-z_2)^2/(\alpha_1+\alpha_2)}$$

and the Josephson energy, proportional to $\int dz(\psi_1^{V*}\psi_2^V + \psi_1^V\psi_2^{V*})$,

$$\mathcal{E}_{Jos} = 2\Omega_{eff}\sqrt{N_1N_2}\ \cos\tilde{\phi}$$

where $\tilde{\phi} = \phi_1 - \phi_2 - p_1z_1 + p_2z_2 + \delta_1z_1^2/2 - \delta_2z_2^2/2 + \frac{1}{2}arctan\frac{\mathcal{P}}{\mathcal{A}} + \frac{\rho}{4\mathcal{D}}$ is the effective dynamical phase difference, where $\mathcal{A} = 1/\alpha_1 + 1/\alpha_2$, $\mathcal{P} = \frac{1}{2}(\delta_1 - \delta_2)$, $\mathcal{B} = -2(z_1/\alpha_1 + z_2/\alpha_2)$, $\mathcal{Q} = p_1 - p_2 - \delta_1z_1 + \delta_2z_2$, $\xi = \mathcal{A}(\mathcal{B}^2 - \mathcal{Q}^2) + 2\mathcal{B}\mathcal{P}\mathcal{Q}$,

$\rho = \mathcal{P}(\mathcal{B}^2 - \mathcal{Q}^2) - 2\mathcal{A}\mathcal{B}\mathcal{Q}$ and $\mathcal{D} = \mathcal{A}^2 + \mathcal{P}^2$. Using these notations the effective Josephson coupling is given by

$$\Omega_{eff} = \sqrt{2}\Omega_0[\alpha_1\alpha_2\mathcal{D}]^{-1/4}\ e^{-z_1^2/\alpha_1 - z_2^2/\alpha_2 + \xi/4\mathcal{D}}\ :$$

after some algebraic manipulations, the coupling can be cast in the form

$$\Omega_{eff} = \sqrt{2}\Omega_0[\alpha_1\alpha_2\mathcal{D}]^{-1/4} exp\Big\{ -\frac{z^2}{\mathcal{D}}\Big[\frac{1}{\alpha_1\alpha_2}\Big(\frac{1}{\alpha_1} + \frac{1}{\alpha_2}\Big) + \frac{1}{4}\Big(\frac{\delta_1^2}{\alpha_2} + \frac{\delta_2^2}{\alpha_1}\Big)\Big]\Big\} \cdot$$
$$\cdot\, exp\Big\{\frac{zp}{2\mathcal{D}}\Big(\frac{\delta_1}{\alpha_2} + \frac{\delta_2}{\alpha_1}\Big) - \frac{p^2}{4\mathcal{D}}\Big(\frac{1}{\alpha_1} + \frac{1}{\alpha_2}\Big)\Big\} \qquad \text{(C.4)}$$

where $z = z_1 - z_2$ and $p = p_1 - p_2$. The Eq.(C.4) shows that the effective Josephson coupling depends only on the relative position z, and not on the center-of-mass variables. The main consequence of this is that, to leading order, the population oscillations decouple from the COM dynamics.

The equations of motion can be written by the Euler-Lagrange equations $\frac{d}{dt}\frac{\partial\mathcal{L}}{\partial\dot{q}} = \frac{\partial\mathcal{L}}{\partial q}$, with $q = N_j, \phi_j, z_j, p_j, \alpha_j, \delta_j$.

Bibliography

[1] B.P. Anderson and M.A. Kasevich, Science **282**, 1686 (1998).

[2] K. Bongs, S. Burger, S. Dettmer, D. Hellweg, J. Arlt, W. Ertmer, and K. Sengstock, Phys. Rev. **A63**, 31602 (2001).

[3] M. Greiner, I. Bloch, O. Mandel, T.W. Haensch, and T. Esslinger, cond-mat/0105105.

[4] W.K. Hensinger *et al.*, Nature **412**, 52 (2001).

[5] O. Morsch, J.H. Müller, M. Cristiani, D. Ciampini and E. Arimondo cond-mat/0108457.

[6] C. Orzel, A.K. Tuchman, M.L. Fenselau, M. Yasuda, and M.A. Kasevich, Science **291**, 2386 (2001).

[7] S. Burger, F.S. Cataliotti, C. Fort, F. Minardi, M. Inguscio, M.L. Chiofalo and M.P. Tosi, Phys. Rev. Lett. **86**, 4447 (2001).

[8] F.S. Cataliotti, S. Burger, C. Fort, P. Maddaloni, F. Minardi, A. Trombettoni, A. Smerzi, and M. Inguscio, Science **293**, 843 (2001).

[9] K. Berg-Sorensen and K. Molmer, Phys. Rev. **A58**, 1480 (1999).

[10] J. Javanainen, Phys. Rev. **A60**, 4902 (1999).

[11] D. Choi and Q. Niu, Phys. Rev. Lett. **82**, 2022 (1999).

[12] M.L. Chiofalo and M.P. Tosi, Phys. Lett. **A268**, 406 (2000).

[13] A. Trombettoni and A. Smerzi, Phys. Rev. Lett. **86**, 2353 (2001).

[14] F.Kh. Abdullaev, B.B. Baizakov, S.A. Darmanyan, V.V. Konotop, and M. Salerno, Phys. Rev. **A64**, 43606 (2001).

[15] V.V. Konotop and M. Salerno, cond-mat/0108212.

[16] D. Hennig and G.P. Tsironis, Phys. Rep. **307**, 333 (1999).

[17] K.Ø. Rasmussen, T. Cretegny, P.G. Kevrekidis, and N. Grønbech-Jensen, Phys. Rev. Lett. **84**, 3740 (2000).

[18] P.G. Kevrekidis, K.Ø. Rasmussen, and A.R. Bishop, Phys. Rev. **E61**, 4652 (2000).

[19] J.H. Müller, D. Ciampini, O. Morsch, G. Smirne, M. Fazzi, P. Verkerk, F. Fuso, and E. Arimondo, J. Phys. **B33**, 4095 (2000).

[20] J.H. Müller, O. Morsch, D. Ciampini, M. Anderlini, R. Mannella, and E. Arimondo, Phys. Rev. Lett. **85**, 4454 (2000).

[21] A. Trombettoni, A. Smerzi, and A.R. Bishop, submitted.

[22] L.P. Pitaevskii and S. Stringari, cond-mat/0104458.

[23] A. Cuccoli, A. Fubini, V. Tognetti, and R. Vaia, cond-mat/0107387.

[24] A. Smerzi, A. Trombettoni, T. Lopez-Arias, C. Fort, P. Maddaloni, F. Minardi, and M. Inguscio, submitted.

[25] D. Jaksch, C. Bruder, J.I. Cirac, C.W. Gardiner, and P. Zoller, Phys. Rev. Lett. **81**, 3108 (1998).

[26] A. Brunello, F. Dalfovo, L.P. Pitaevskii, and S. Stringari *et al.*, Phys. Rev. Lett. **85**, 4422 (2000).

[27] O. Zobay and B.M. Garraway, Phys. Rev. **A61**, 33603 (2000).

[28] M.L. Chiofalo, M. Polini, and M.P. Tosi, Eur. Phys. J. **D11**, 371 (2000); M.L. Chiofalo, S. Succi, and M.P. Tosi, Phys. Rev. **A63**, 63613 (2001).

[29] B. Wu and Q. Niu, cond-mat/0009455.

[30] S. Pötting, M. Cramer, C.H. Schwalb, H. Pu, and P. Meystre, Phys. Rev. **A64**, 23604 (2001).

[31] B. Wu, R.B. Diener, and Q. Niu, cond-mat/0109183.

[32] F. Dalfovo, S. Giorgini, L.P. Pitaevskii, and S. Stringari, Rev. Mod. Phys. **71**, 463 (1999).

[33] P. Pedri, L.P. Pitaevskii, S. Stringari, C. Fort, S. Burger, F.S. Cataliotti, P. Maddaloni, F. Minardi, and M. Inguscio, cond-mat/0108004.

[34] A. Trombettoni and A. Smerzi, J. Phys. **B**, in press.

[35] A. Smerzi, S. Fantoni, S. Giovanazzi, and S.R. Shenoy, Phys. Rev. Lett. **79**, 4950 (1997).

[36] S. Raghavan, A. Smerzi, S. Fantoni, and S.R. Shenoy, Phys. Rev. **A59**, 620 (1999).

[37] E.A. Ostrovskaja, Yu.S. Kivshar, M. Lisak, B. Hall, F. Cattani, and D. Anderson, Phys. Rev. **A61**, R31601 (2000).

[38] *Proceedings of the Conference on Future Directions of Nonlinear Dynamics in Physical and Biological Systems, Denmark,* edited by P.L. Christiansen, J.C. Eilbeck, and R.D. Parmentier [Physica (Amsterdam) **68D**, 1-186 (1993)].

[39] A.C. Scott, *Nonlinear Science: Emergence and dynamics of coherent structures*, Oxford University Press (1999).

[40] S. Flach and C.R. Willis, Phys. Rep. **295**, 181 (1998).

[41] J.D. Andersen and V.M. Kenkre, Phys. Rev. **B47**, 11134 (1993).

[42] M. Peyrard, T. Dauxois, H. Hoyet, and C.R. Willis, Physica **68D**, 104 (1993).

[43] D. Cai, A.R. Bishop, and N. Grønbech-Jensen, Phys Rev. Lett. **72**, 591 (1994); Phys. Rev. **E53**, 4131 (1996).

[44] R. Scharf and A.R. Bishop, Phys. Rev. **A43**, 6535 (1991); Phys. Rev. **E47**, 1375 (1993).

[45] F. Cooper, H. Shepard, C. Lucheroni, and P. Sodano, Physica **68D**, 344 (1993).

[46] A.B. Aceves, C. De Angelis, T. Peschel, R. Muschall, F. Lederer, S. Trillo, and S. Wabnitz, Phys. Rev. **E53**, 1172 (1996).

[47] O. Zobay, S. Pötting, P. Meystre, and E. M. Wright, Phys. Rev. **A59**, 643 (1999).

[48] S. Burger, K. Bongs, S. Dettmer, W. Ertmer, K. Sengstock, A. Sanpera, G.V. Shlyapnikov, and M. Lewenstein, Phys. Rev. Lett. **83**, 5198 (1999).

[49] P. Binder, D. Abraimov, A.V. Ustinov, S. Flach, and Y. Zolotaryuk, Phys. Rev. Lett. **84**, 745 (2000); E. Trias, J.J. Mazo, and T.P. Orlando, Phys. Rev. Lett. **84**, 741 (2000).

[50] U.T. Schwarz, L.Q. English, and A.J. Sievers, Phys. Rev. Lett. **83**, 223 (1999).

[51] H.S. Eisenberg, Y. Silberberg, R. Morandotti, A.R. Boyd, and J.S. Aitchison, Phys. Rev. Lett. **81**, 3383 (1998).

[52] B.I. Swanson, J.A. Brozik, S.P. Love, G.F. Strouse, A.P. Shreve, A.R. Bishop, and W.-Z. Wang, Phys. Rev. Lett. **82**, 3288 (1999).

[53] T.V. Ramakrishnan, in *Chance and Matter*, Proceedings of the Les Houches Summer School, Session XLVI, edited by J. Souletie, J. Vannimenus, and R. Stora (North-Holland, Amsterdam, 1987), p. 213.

[54] A. J. Leggett, Rev. Mod. Phys. **73**, 307 (2001).

[55] A. Barone, *Weakly coupled macroscopic quantum systems: likeness with difference*, I. O. Kulik, R. Ellialtioglu, Eds. (Kluwer Academic Publishers 2000), pp.301-320.

[56] A.Barone and G.Champ Paternò, *Physics and Applications of Josephson Effect*, Wiley-Interscience, New York, 1982.

[57] B.D. Josephson, Phys. Lett. **1**, 251 (1962).

[58] O. Avenel and E. Varoquaux, Phys. Rev. Lett. **60**, 416 (1988).

[59] S.V. Pereverzev, A. Loshak, S. Backhaus, J.C. Davis, and R.E. Packard, Nature **388**, 449 (1997).

[60] R. Fazio and H. van der Zant, cond-mat/0011152.

[61] Y. Makhlin, G. Schön, and A. Shnirman, Rev. Mod. Phys. **73**, 357 (2001).

[62] M. Kozuma, L. Deng, E.W. Hagley, J. Wen, R. Lutwak, K. Helmerson, S.L. Rolston, and W.D. Phillips, Phys. Rev. Lett. **82**, 871 (1999).

[63] S.L. Sondhi, S.M. Girvin, J.P. Carini, and D. Shahar, Rev. Mod. Phys. **69**, 315 (1997).

[64] T.D. Kuehner, S.R. White, and H. Monien, Phys. Rev. **B61**, 12474 (2000).

[65] R.M. Bradley and S. Doniach, Phys. Rev. **B30**, 1138 (1984).

[66] A.I. Larkin and L.I. Glazman, Phys. Rev. Lett. **79**, 3736 (1997).

[67] M.-S. Choi, J. Yi, M.Y. Choi, J. Choi, and S.-I. Lee, Phys. Rev. **B57**, R716 (1998).

[68] I. Zapata, F. Sols, and A.J. Leggett, Phys. Rev. **A57**, R28 (1998).

[69] G.B. Witham, J. Fluid. Mech. **27**, 399 (1967); T.B. Benjamin and J.E. Feir, J. Fluid. Mech. **27**, 417 (1967).

[70] L.A. Ostrovskii, Sov. Phys. JETP **24**, 797 (1969).

[71] A. Hasegawa, Phys. Rev. Lett. **24**, 1165 (1970).

[72] M. Peyrard and A.R. Bishop, Phys. Rev. Lett. **62**, 2755 (1989); T. Dauxois, M. Peyrard, and A.R. Bishop, Phys. Rev. **E47**, 684 (1993).

[73] Yu.S. Kivshar and M. Peyrard, Phys. Rev. **A46**, 3198 (1992).

[74] I. Daumont, T. Dauxois, and M. Peyrard, Nonlinearity **10**, 617 (1997).

[75] M. Peyrard and M. Kruskal, Physica **14D**, 88 (1984); P.G. Kevrekidis and M.I. Weinstein, Physica **142D**, 113 (2000).

[76] T. Dauxois and M. Peyrard, Phys. Rev. Lett. **70**, 3935 (1993).

[77] M. Johansson and S. Aubry, Phys. Rev. **E61**, 5864 (2000).

[78] A. Sanchez and A.R. Bishop, SIAM Rev. **40**, 579 (1988).

[79] R. Morandotti, U. Peschel, J.S. Aitchison, H.S. Eisenberg, and Y. Silberberg, Phys. Rev. Lett. **83**, 2726 (1999).

[80] R. Morandotti, U. Peschel, J.S. Aitchison, H.S. Eisenberg, and Y. Silberberg, Phys. Rev. Lett. **83**, 4756 (1999).

[81] M.I. Molina, Phys. Rev. **B58**, 12547 (1998).

[82] V.M. Kenkre and D.K. Campbell, Phys. Rev. **B34**, 4959 (1986).

[83] A. Trombettoni *et al.*, in preparation.

[84] M.R. Andrews, C.G. Townsend, H.-J. Miesner, D.S. Durfee, D.M. Kurn, and W. Ketterle, Science **275**, 637 (1997).

[85] M.R. Matthews, B.P. Anderson, P.C. Haljan, D.S. Hall, C.E. Wieman, and E.A. Cornell, Phys. Rev. Lett. **83**, 2498 (1999).

[86] M. Benakli, S. Raghavan, A. Smerzi, S. Fantoni, and S.R. Shenoy, Europhys. Lett. **46**, 275 (1999).

[87] G.J. Milburn, J. Corney, E.M. Wright, and D.F. Walls, Phys. Rev. **A55**, 4318 (1997).

[88] L.-M. Kuang and Z.-W. Ouyang, Phys. Rev. **A61**, 23604 (2000)

[89] I. Marino, S. Raghavan, S. Fantoni, S.R. Shenoy, and A. Smerzi, Phys. Rev. **A60**, 487 (1999).

[90] J. Williams, R. Walser, J. Cooper, E. Cornell, and M. Holland, Phys. Rev. **A59**, R31 (1999); Phys. Rev. **A61**, 33612 (2000).

[91] P. Maddaloni, M. Modugno, C. Fort, F. Minardi, and M. Inguscio, Phys. Rev. Lett. **85**, 2413 (2000); M. Modugno, F. Dalfovo, C. Fort, P. Maddaloni, and F. Minardi, Phys. Rev. **A62**, 63607 (2000).

[92] C.-Y. Lin, E.J.V. de Passos, and D.-S. Lee, Phys. Rev. **A62**, 55603 (2000).

[93] J. Denschlag *et al.*, Science **287**, 97 (2000).

[94] D.R. Tilley and J. Tilley, *Superfluidity and Superconductivity*, Hilger, New York (1990).

[95] A.J. Leggett, in *Bose-Einstein Condensation*, edited by A. Griffin, D.W. Snoke, and S. Stringari, Cambridge University Press, Cambridge (1995).

[96] A. Smerzi, S. Raghavan, S. Fantoni, and S. R. Shenoy, Eur. Phys. J. **B**, in press.

[97] R.A. Webb, R.L. Kleinberg, and J.C. Wheatley, Phys. Lett. **48A**, 421 (1974).

[98] J. Ruostekoski and D.F. Walls, Phys. Rev. **A58**, R50 (1998).

[99] N.F. Ramsey, *Molecular Beams*, Oxford Press (1985).

[100] W. Zurek, Phys. Today **44**, 36 (1991).

[101] R.E. Graham, D.E. Knuth, and O. Patashnik, *Concrete mathematics: a foundation for computer science*, Addison-Wesley (1989).